Synthesis and Characterization of Nanoparticles and Nanostructured Materials for Thermoelectric Applications

NGUYEN THANH MAI

Japan Advanced Institute of Science and Technology

Synthesis and Characterization of Nanoparticles and Nanostructured Materials for Thermoelectric Applications

by

NGUYEN THANH MAI

Submitted to

Japan Advanced Institute of Science and Technology

In partial fulfillment of the requirements

For the degree of

Doctor of Philosophy

Supervisor: Professor Dr. Shinya Maenosono

School of Materials Science

Japan Advanced Institute of Science and Technology

September 2013

Acknowledgment

This thesis could not be completed without the support and contribution of many people. I would like to thank Prof. Dr. Shinya Maenosono for supervise me during my research. His encouragement, guidance and support always lead me ahead with my research. He creates a good research environment in the lab that I can study and enjoy my study time.

I highly acknowledge Prof. Dr. Kohki Ebitani for being my second supervisor. I learn from him many helpful things for my research and my life.

My thanks will go to Assoc. Prof. Dr. Mikio Koyano for his acceptance as my minor research project supervisor. His kindly guidance and discussions strongly contribute to the expansion of my knowledge to physic aspects of my work.

I would like to acknowledge the useful discussion and help from Prof. Hideo Iwasaki, Dr. Koichiro Suekuni, Dr. Tatsuya Murakami, Dr. Koichi Higashimine, Dr. Go Nakamoto from JAIST and Dr. Atsushi Yamamoto from AIST. They kindly cooperate with me in many of the technical issues and measurements presented in this thesis.

I would like to thank Dr. Derrick M. Mott for his support and discussion from the very beginning of my research in Japan as well as his correcting and proofreading my paper works.

I express my sincere gratitude to the former and current members of the Maenosono and Ebitani Lab for their support and sharing with me the studying time in the lab.

Finally, I would like to thank my family for their endless love and understanding for all hard and happy moment of my life.

Nguyen Thanh Mai

September 2013

Table of Contents

Abbreviation and Symbol

Abbreviation

DT	Decanethiol
EDS	Energy Dispersive X-ray Spectroscopy
HAADF	High Angle Annual Dark Field
HR-TEM	High Resolution Transmission Electron Microscopy
ICP-MS	Inductively Couple Plasma - Mass Spectroscopy
ICP-OES	Inductively Couple Plasma – Optical Emission Spectroscopy
ND, NDs	Nanodisc, Nanodiscs
NP, NPs	Nanoparticle, Nanoparticles
NW, NWs	Nanowire, Nanowires
OAC	Oleic Acid
OAM	Oleylamine
SEM	Scanning Electron Microscopy
STEM	Scanning Transmission Electron Microscopy
TE	Thermoelectric
TEM	Transmission Electron Microscopy
TGA	Thermal Gravimetric Analysis
XPS	X-ray Photoelectron Spectroscopy
XRD	X-ray Diffraction

Symbol

α	Seebeck coefficient
κ	Thermal conductivity
ρ	Electrical resistivity
σ	Electrical conductivity
λ	Wavelength

List of Figure

List of Table

Abstract

Thermoelectric (TE) materials are interesting research field for energy conversion applications such as cooling devices, power generation, energy harvesting materials. Because TE materials can enable the direct alternative conversion between poor-quality thermal energy and high-quality electric energy, the renewal of these materials can make them become potential candidate for a next generation technology of waste heat recovery. TE materials with phonon-glass electron-crystal (PGEC) property have been recognized as one of the most promising approaches to improve the TE efficiency for practical applications and introducing desired nanostructure into TE materials is one way to create PGEC materials. Because of the capability of well control morphology and nanostructure, chemical synthesis is interesting for producing nanoparticles (NP)s with tailorable characteristics for TE applications. Furthermore, the chemical synthesis could be scaled up to obtain large amount of NPs for creating nanostructured TE materials.

The purpose of this research is to develop the chemical synthesis approaches towards nanoparticles and nanostructured materials for TE applications. With this purpose, my research will address the issues regarding NPs synthesized *via* chemical methods in order to offer scalable and economic comparative syntheses with capability of creating compounds and alloys with tailorable characteristics in nanoscale regime. The NPs which I focus on include Bi-Sb-Te based ternary alloys and Zn-Sb alloys which can be applied for room temperature to 400 ^{o}C and are challenging for chemical synthesis.

(1) Synthesis and formation mechanism to control the composition and morphology of solid solution BiSbTe NPs

The modified polyol method was utilized to synthesized BiSbTe containing NPs *via* a one-pot chemical reaction. The resulting NPs show various morphologies (nanowires, nanodiscs, nanodiscs grew on NWs) associated with nature of the capping ligands used in the synthesis and the phase segregation occurs in each case. Because of the complicated interactions between metal precursors and capping ligands as well as the metal interaction in the one-pot reaction, a systematic investigation of the synthesis of monometallic, bimetallic and trimetallic NPs was conducted to elucidate the NP's formation mechanism. The results of the investigation indicate that using DT as capping ligand, Te can act as the catalyst for the formation of Bi_2Te_3 and Sb_2Te_3 and the strong interaction between Te and Bi and/or Sb precursor complex results in the phase segregation of the resulting BiSbTe containing NPs. On the other hand, using OAM as the capping species, BiSb NPs (alloy) can be formed and the interaction between BiSb and Te NPs in the solution can result in the formation of ternary BiSbTe NPs. Based on the NP's formation mechanism, the one-pot synthesis is performed with tri-molecular precursors in OAM to achieve ternary BiSbTe NWs. To further control the morphology and composition of ternary BiSbTe NPs, the chemical synthesis was modified in which BiSb alloy NPs with tailorable composition first prepared in the presence of OAM and used as the seed to grow ternary solid solution BiSbTe NPs. The resulting NPs are ternary alloy of Bi, Sb and Te and the ratios of Bi:Sb and the morphology of the seeds were maintained in the BiSbTe NPs. The results of these studies offer the fundamental understanding of the NPs' formation mechanism and the basic knowledge to synthesize NPs with controllable morphology and composition.

(2) Zn-Sb NPs: chemical synthesis and large scale reaction to create the nanostructured Zn-Sb materials.

A chemical synthesis with multiple steps in one-pot reaction was designed via the formation of Sb NPs as the seed followed by the reduction of Zn on surface of Sb NPs and alloying to form Zn-Sb NPs. The careful investigation using TEM, XRD, EDS, XPS, STEM-HAADF reveals the complex structure of Zn-Sb NPs with core-shell like morphology and the opposite composition distribution of Zn and Sb from the core to the shell of single NP. The enhancement of oxidation stability of Zn-Sb NPs is associated with the alloy formation.

The nanostructured Zn-Sb materials were prepared from Zn-Sb NPs obtained in the large scale synthesis (after surface treatment) *via* hot-pressing. The Zn-Sb pellets still possess the nanograinboundary and the TE properties of the pellets were investigated. The results indicated that the pellets have semiconducting properties with good electrical conductivity, low thermal conductity and Seebeck coefficient similar to Sb, which arises from the existence of Sb phase and Zn-Sb phase together with ZnO in the pellet. Even though the TE efficiency is not significant, the research exhibits the capability of utilizing NPs as the building block for creating nanostructured TE materials. Further study on the reaction and pressing conditions can help to improve the TE efficiency.

Key word: thermoelectric, nanoparticles, semiconductor, chemical synthesis, alloy

Chapter 1

General Introduction to Thermoelectric Materials and Research Objective

This chapter will give a general introduction to the thermoelectric (TE) effect, TE materials and the challenges to make TE materials practical available for energy conversion. The studies on improving TE efficiency, the center of the current research on TE materials, are briefly reviewed. We then focus on the nanoparticles as a potential candidate for improving TE performance with an overview on the chemical synthesis approach to get nanoparticles as promising building block for creating TE materials. The difficulties and strategy to synthesize nanoparticles with well-defined structure and tunable properties for TE applications will be reviewed. The chapter will conclude with the objective of the research.

1.1. Introduction to Thermoelectric Materials

Energy is considered to be the blood of the planet because of the fact that all activities of living thing require energy. The energy sources consist of two types, one is the long term energy (eternal energy) such as solar energy or earth heat and the other created from solar energy and stored in biomass and underwent a chemical and physical transition such as charcoal, petroleum, natural gas... The later is ready to use but it is expected to be quickly run out in the future at the current demand of energy. Furthermore, using these energy sources always result in the CO_2 emission and greenhouse effect which damages the environment and sustainable development. A new policy and research should be devoted to solve these problems. One direction mainly focuses on creating new energy sources such as making use of reusable energy from biomass, fuel cell, solar cell… Researchers all over the world are doing their best for those green energy sources widely and practically available to replace oil and charcoal. The other direction which also attracts much of consideration is to improve the efficiency of using energy in the world (in other words, saving energy). It would be significant if we take into account the current efficiency of using energy where about 30 % of energy will be ready to use while large amount of energy releases as heat waste. In term of power generation as well as improving the energy usage efficiency, thermoelectric (TE) materials known to be one potential candidate can converse heat (in general) and/ or heat lost to electricity. In other words, these materials enable direct alternative conversion between poor-quality thermal energy and high-quality electric energy. Especially, the reuse of waste heat will be significant with the renewal of these materials to become a next generation technology. Another advantage of TE materials is associated with the fact that TE materials can help to reduce the impact on the environment *via* diminishing CO_2 emission during the energy conversion processes. The advantage is also worth when TE materials are utilized as electronic cooling devices and equipments when apply the current to generate the thermal difference at their ends without moving part or Freon generation. Therefore, to solve the energy and environmental issues, TE materials are expected to be very important candidate.[1-7]

Back to the history of TE materials, the underlying physics of TE materials, called thermoelectric effects including Seebeck effect, Peltier effect, are well known for a long time. However, since Seebeck effect and Peltier effect were separately discovered in 1821 and 1834 respectively which served as basic principles for TE materials, until second half of the 20th century, TE materials for energy conversions became practical.[3,4] The great consideration and

extensive researches were put on this field which resulted in the finding of Bi and Bi-Sb alloys, Bi_2Te_3 based alloys and PbTe compound as well as Si-Ge alloys as the state of the art materials for specific temperature ranges.[1,5,7] Those studies also expanded a huge knowledge of TE properties and materials characteristics relation, synthesis techniques and characterization methods. However from those studies, a limitation of TE efficiency is found and set a big challenge for not only the wide application of TE materials in terms of energy conversions but also the further study in this field. By the 1970s, less research effort was made in TE material and seemed to be stopped because it was considered as a mature field. Two decades later, in the 1990s, when the energy crisis become serious and requirement for higher TE efficiency became crucial for the future development, TE research had been brought back with great of interest. Along with the renewing of TE research, many new findings in theoretical and calculation aspect, thin film, nanotechnology and new concept for materials have been discovered and evidenced, which expected to open new windows for higher TE performance.

The following part of this chapter will overview the underlying principle of TE effect, thermoelectric efficiency and its limitation, the materials for thermoelectric application, the proposed solutions for improving TE efficiency. A part of this chapter will focus on the chemical synthesis approach to get TE nanoparticles (NP)s as promising building block for TE application. This chapter will end with the research area and the objective of the study presented in the thesis. The characterization methods of low dimensional materials and the measurement of TE properties are important for study in field of NP for TE applications will be given in the Appendix I.

1.2. Thermoelectric Effect, Thermoelectric Efficiency and Its Limitation

Thermoelectric effects refer to the effects in which thermal energy converts to electricity and vice versa. The Seebeck effect, named after the physicist Thomas Johann Seebeck, occurs when a temperature gradient between the junctions of two conductors connected each other raises a voltage between two junctions. This effect is familiar with all technicians and scientists who work with a thermal couple to measure temperature. The Seebeck effect can be expressed *via* an integral form relates the voltage V appears at temperature difference ΔT: $V = \alpha_{ab}\Delta T$, where α_{ab} is the Seebeck coefficient of two junctions between conductors a and b (Fig. 1.1A).

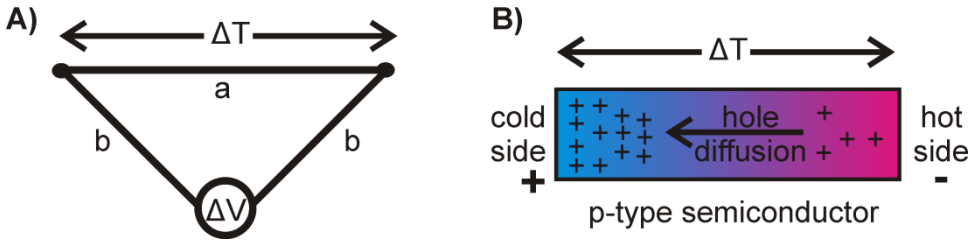

Figure 1.1. Schematic illustration of Seebeck effect (A) and a gas diffusion model to explain the voltage arises from the temperature gradient applied to a p-type semiconductor (B).

The Peltier effect which named after Jean Charles Athanase Peltier exhibits the phenomenon when a current passing though the junction between two conductors creates the temperature different at the two ends of the junction. The integral form of the Peltier effect is $\pi_{ab} = q/I$, where q is the heating rate (cooling rate) at one of the junctions when an electric current I passes round the circuit and π_{ab} is the Peltier coefficient for these two junctions. The Seebeck effect and Peltier effect are reversible phenomenon and closely related to each other *via* the Kelvin relationships: $\pi_{ab} = \alpha_{ab}T$. It is noted that these two thermoelectric effects are defined for two junctions between two conductors, but the two coefficients are properties of the bulk materials which have the absolute coefficient (α_a, π_a for examples) and α_{ab} and/or π_{ab} equal to the different of the absolute coefficients of two conductors ($\alpha_{ab} = \alpha_a - \alpha_b$, $\pi_{ab} = \pi_a - \pi_b$). The Seebeck coefficient is often regarded as thermopower of the materials and can be measured easier than the Peltier coefficient. The Seebeck and Peltier effects can be imagined with consideration that electrons/holes diffuse under temperature gradient or move in the electric field as gas model (Fig. 1.1B).

The efficiency of TE materials is defined by the useful work (w) divided by the heat (q) from the heat source: w/q. The temperature different between the heat source (T_H) and the sink (T_C) (T_H-T_C) results in the electromotive force $V = \alpha_{ab}(T_H-T_C)$. The current of the circuit I, equals to $V/(R+R_L)$ where R is the resistance of TE generator and R_L is the resistance of the load. The heat is the sum of the heat lost by thermal conduction of the TE generator and the heat compensates for Peltier cooling of the hot junction when the current passes through:

$$q = K(T_H-T_C) + \alpha_{ab}IT_H \quad (1)$$

The highest efficiency (η_{max}) was first given by Ioffe as follows:

$$\eta_{max} = \frac{(T_H - T_C)}{T_H} \frac{(1+ZT)^{1/2}}{T_C/T_H + (1+ZT)^{1/2}} \quad (2)$$

where $T = (T_H+T_C)/2$, and Z equals to (α_{ab}^2/KR) which is the figure of merit of the TE generator (Fig. 1.2). It is noted that $(T_H-T_C)/T_H$ is the maximum efficiency of an ideal thermodynamic machine (Carnot efficiency). Therefore, the highest TE efficiency could be reached when Z value becomes very large. The efficiency of TE materials strongly depends on the Z (ZT) value and the Z value depends on the properties of both materials which form the TE generator. The figure of merit Z of the TE generator when it reaches the optimum value is given by:

$$Z = \frac{(\alpha_a - \alpha_b)^2}{[(\sigma_a \kappa_a)^{1/2} + (\sigma_b \kappa_b)^{1/2}]^2} \quad (3)$$

where κ_a, κ_b is the thermal conductivity of two branches of TE generator.

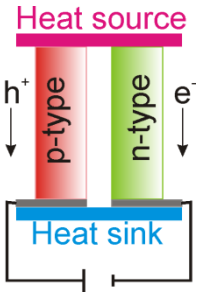

Figure 1.2. Thermoelectric generator composed of n-type and p-type semiconductors based on Seebeck effect.

For a single material, the figure of merit is defined as $z = \alpha^2\sigma/\kappa$ (where σ is the electrical conductivity, κ is the thermal conductivity and α is the Seebeck coefficient of the material) which is convenient in investigation of the TE materials. The figure of merit has the dimension of inverse temperature, and when times it with absolute temperature (normally operating temperature range) we have the dimensionless figure of merit, zT, which is commonly used. The other definition of figure of merit is as the ratio of power factor to thermal conductivity. The power factor ($\alpha^2\sigma$) depends on the electronic properties of the material while the thermal conductivity is sum of lattice and electrical thermal conductivity, κ_L and κ_e respectively. It is noted that the electrical thermal conductivity always exists and it is in

relationship with the electrical conductivity expressed in Wiedemann-Franz law: $\kappa_e = L\sigma T$, where L is the Lorentz number which is a constant for metal and depend on the Fermi level for a semiconductor (SC). For this reason, each increase or decrease of electrical conductivity always causes the corresponding increase or decrease of thermal conductivity, which make the ratio of σ/κ_e nearly constant. Moreover, the Seebeck coefficient, α, is also in a relation with the electrical conductivity, σ, because an increase in α of often gives a certain decrease of σ. The interrelation of parameters determined thermoelectric efficiency therefore sets a limitation (zT about 1) which is difficult to overcome.

1.3. Materials for Thermoelectric Applications

A good material for TE applications must satisfy the following requirements of high enough Seebeck coefficient, high electrical conductivity and low thermal conductivity. Because an increase in α often leads to the decrease of σ and the decrease of σ results in the decrease of the electronic contribution to κ as displayed in Wiedemann-Franz law. Hence, for bulk materials, these requirements themselves make a fundamental challenge for searching a good TE material. Metals and their alloys generally have very low α (less than some tens of microvolts per Kelvin) and the ratio of σ to κ nearly the value given by Wiedemann-Franz law, which is all together resulting in much less than unity of the dimensionless TE figure of merit (zT).

Since semiconductors were discovered, the higher Seebeck coefficient of milivolts per Kelvin was found in some SCs.[8] However, SCs with enhanced Seebeck coefficient still displayed a small value of the ratio between electrical conductivity and thermal conductivity due to the fact that they have low electrical conductivity and the dominant of the lattice thermal conductivity. The improvement in the ratio between electrical and thermal conductivity nearly the value given in Wiedemann-Franz law in some of SCs make them become the current used TE materials. In the classical approximation,[3] the zT value was estimated by:

$$zT = \frac{[\eta - (r+\frac{5}{2})]^2}{(\beta \exp\eta)^{-1} + (r+\frac{5}{2})} \quad (4)$$

where η is the Fermi energy divided by kT (different from the efficiency in eq.2), r is a scattering parameter that describes the way in which the relaxation time for the carriers varies with energy and r often lies between -1/2 and 3/2, the extremes corresponding to acoustic-mode lattice scattering and ionized-impurity scattering. β was given by:

$$\beta = 5.745 \times 10^{-6} \frac{\mu}{\lambda_L} (\frac{m^*}{m})^{3/2} T^{5/2} \quad (5)$$

where μ is the carrier mobility, m and m^* is the mass of a free electron and the effective mass of the carriers. For the optimum value of zT, the quantity β should be as high as possible. However, it is found that for known materials, β is less than 0.5.

The calculations based on classical statistics as well as Fermi-Dirac statistics are in good agreement in indicating the zT can reach the optimum in SCs with high carrier mobility, large effective mass, and low thermal conductivity. It also requires a large enough energy gap, E_g, for the negligible of the concentration of the minority carrier when the Seebeck coefficient is optimized. In the classical SCs, the maximum value of Seebeck coefficient at given temperature is equal to $E_g/2eT$, where e is the electronic charge. The Seebeck coefficient can be calculated using Fermi-Dirac statistics, and the optimum value is close to ± 200 μVK^{-1}.[3]

1.4. Solutions for Improving the Thermoelectric Efficiency

The solutions for improving TE efficiency include the methods to obtain materials displaying good Seebeck coefficient, electrical conductivity and low thermal conductivity, on the other words, to reduce the lattice thermal conductivity without much decrease of the power factors, or improvement of power factor of the existing materials without increasing much of thermal conductivity. The current researches in the field of TE indicate that the phonon glass electron transmission materials which offer low thermal conductivity as glasslike materials and high electrical conductivity as metal should be ideal for high performance thermoelectricity.[9] Introducing the mechanism to lower the thermal conductivity *via* effective and selective phonon scattering therefore becomes very important to obtain the ideal TE materials. Because the heat carried by phonon often has a band spectrum of mean free path (MFP)[10] which can be scattered in different mechanisms (Fig. 1.3), the study and combination of scattering phonons with short, medium, and long MFP can result in extremely low thermal conductivity at the same extent of electrical structure. The following reviews the methods to effectively scatter heat carried by phonon at different length scale (of the MFP) while not much affect on the electrical conductivity of the materials.

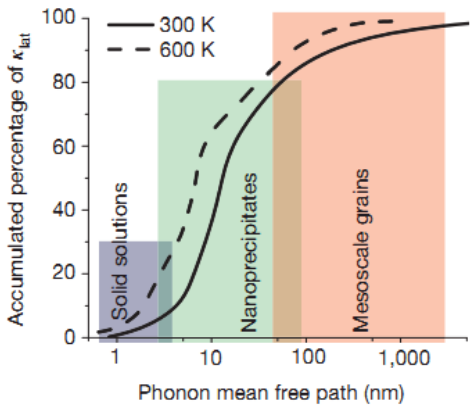

Figure 1.3. Contribution of phonons with different mean free paths to the cumulative lattice thermal conductivity value for PbTe adapted from ref. 10.

1.4.1. Alloying

This method was first proposed by Ioffe and his colleagues based on the prediction that alloying allows introducing the short range disturbance to significantly scatter phonon but the maintaining the long range order to prevent the scattering of electrons and holes.[8] As a result, the alloys exhibit much lower thermal conductivity than their constituents without decreasing of electrical conductivity. This approach serves as one efficient method providing the most improvement of zT in 1950s -1960s and find its significant in Bi_2Te_3 based materials (now mostly in solid solution with Sb_2Te_3 or Bi_2Se_3 to form one of the best p- and n-type SCs for TE application at room temperature up to 200 ^oC), Pb-Te (often in solid solution with SnTe, PbSe to form one of the best p- and n-type SCs for TE application at intermediate temperature above 200 ^oC to 500 ^oC), and Si-Ge alloys (above 500 ^oC to 1000 ^oC) which are now used as materials for TE generation. For example, the alloy $Bi_{0.5}Sb_{1.5}Te_3$ and $Bi_2Te_{2.7}Se_{0.3}$ show the figure of merit, z, increase to $3.3x10^{-3}$ K^{-1} compared to z of $2x10^{-3}$ K^{-1} for Bi_2Te_3. Another example is about Si-Ge alloy at 300 K the κ values for Si and Ge are of 113 and 63 $Wm^{-1}K^{-1}$ respectively while a solid solution of Si and Ge with composition of $Si_{0.7}Ge_{0.3}$ has κ of only 10 $Wm^{-1}K^{-1}$.

The underlying mechanism of the thermal conductivity reduction is the phonon scattering due to mass fluctuation entire the solid solution. The alloying allows the effectively scattering of phonon with short mean free paths in the order of subnano to several nanometers.

(Phonon scattering mechanisms in crystal structure materials: the decrease of thermal conductivity of crystal materials is often due to the phonon-phonon scattering, phonon-

impurity scattering, phonon-boundary scattering. The first one was further divided into normal phonon scattering and Umklapp scattering where the phonon momentum was transferred to the lattice causing the resistance to the heat flow. The phonon-phonon scattering is important contribution to heat resistance at room temperature due to the Umklapp scattering, but phonon impurity scattering more dominant as lowering the temperature. At low temperature, phonon-boundary scattering contribute to the decrease of thermal conductivity (the MFP of phonon is comparable to the grain size of materials) and this kind of scattering is temperature independence. Therefore, at low temperature, the thermal conductivity is proportional to T^3 as the same as specific heat.)

1.4.2. Phonon rattling in complex symmetric and crystal materials

In 1990s, Slack suggested the concept of "phonon glass electron crystal" (PGEC) as the criteria for good TE materials.[9,11,12] His idea of such TE materials becomes somewhat practical presence in materials exhibiting the complex symmetry and crystal structure with "cages" or "tunnels" large enough for atoms located inside to rattle but do not destroy the favorable electronic structure. The rattling centers (atoms) effectively scatter phonon for which the thermal conductivity is glasslike while allows the electron pass through the crystal lattice, displaying the PGEC structure. The "phonon rattling" concept proposed to reduce the lattice thermal conductivity in the crystal materials with high power factor is important as it had contributed to the great improvement of *zT* observed in the history of TE materials where many solid systems were found to possess *zT* values over 1 such as skutterudites and clathrates based on this standpoint.[9,11-13] However, it is worth to emphasize that even the ideal PGEC material is still not practical presence, the enhancement of *zT* due to the rattling process in complex symmetric materials is a good theoretical guidance for researchers in searching effective TE materials based on lowering the thermal conductivity while maintaining a good electrical conductivity.

1.4.3. Low dimensional materials

Low dimensional thermoelectricity refers to two important strategies to improve *zT* value including: (i) offer large area of boundary for phonon-boundary scattering even at room temperature if the size of materials smaller or comparable with the mean free path of phonon, which results in extremely low κ, while still allows carrier transmission and (ii) improve α and somewhat decoupling α and σ *via* the quantum confinement effect theorized by Hick and

Dresselhaus in which the increase of the density of states near the Fermi energy leads to the enhancement of α and the low dimensionality offer the possibility to tailor the electronic structure to decouple the α and σ.[14,15] The first advantage of the low dimensionality is based on choosing a suitable size of materials that allow the boundary effectively scattering phonon than electron giving rise in the σ/κ ratio.[16-22] The experimental results in Bi_2Te_3-Sb_2Te_3 superlattices[17] and nanostructured TE materials can clearly demonstrate this theoretical standpoint. The second aspect of low dimensionality regarding the enhancement of α arises from the increase of the density of states near the Fermi level due to the confinement effect.[14,15] It was proved in the PbTe-$Pb_{1-x}Eu_xTe$ quantum well superlattices where the increase of α directly relates to the increase of density of state at each subband edge.[3] Furthermore, the experimental results for n-type PbTe agree well with the theoretical calculation results that $\alpha^2 n$, where n is the carrier concentration, also increase with the size decreases of PbTe. Another example is the size dependent semimetal-semiconducting transition due to the quantum confinement effect when the decrease of the size of Bi from the bulk to nano regime leads to the increase in Seebeck coefficient and the capability of tuning its electronic structure from semimetal into SC. These results indicate the possibility of decoupling the interrelated parameters, which determine TE efficiency, in low dimensional materials to obtain enhanced zT values.[3]

Other phenomena displaying in low dimensional materials can also contribute a part to the decoupling and somewhat independently modifying α, σ, κ are energy filtering, carrier pocket engineering.

The theory of low dimensionality (nano regime) for enhanced TE efficiency and the experimental achievements of improved zT values arising from decreasing the size of the state of the art TE materials make this research field become more and more promising for advanced TE materials. As mentioned before in this section, the much higher zT can reach by the combination of the low dimensionality (current approach) with alloying and/or complex structure and symmetry which is the main origin of the high zT in most of the bulk state of the art TE materials. Therefore, introducing low dimensionality (nanostructure) into state of the art TE materials has been active research topic in the field of advanced TE materials. Synthesis of these advanced materials, however, associates with a lot of difficulties regarding precise control the dimensions, nanostructure, composition, surface properties and so on due to its essential importance for TE efficiency improvement. Therefore, the following part of the thesis is devoted to overview the synthesis of nanoparticles (NP)s for TE applications, especially the

chemical synthesis which displays high capability of tailoring NPs characteristics compared to physical methods, its advantages, achievements and challenges.

1.5. Chemical Synthesis of Nanoparticles for Thermoelectric Applications

Regarding the synthesis method for TE materials, physical methods are dominant in producing bulk TE materials. In preparation of NPs for TE applications, there are two main methods categorized based on the starting materials and pathways used to create NPs: first, start with bulk materials, using physical method to reduce size of the bulk (top down methods) and second, start with the molecules and using molecules to build up the nanostructure (bottom up methods).[23] The physical approaches include: alloying, melting, zone-melting, cold/hot-pressing, grinding, spark plasma sintering, crystal growth techniques, molecular beam epitaxy, molecular vapor deposition. Other approaches combine the physical and chemical methods such as electro-chemical synthesis, sono-chemical synthesis also work in producing TE NPs. However, in terms of large scale synthesis, environmentally benign technique and manipulation NPs' characteristics such as size, shape, composition, nanostructure, surface properties, and so on, there are some degrees of difficulty regarding the physical approaches which often require intensiveenergy, normally high temperature, some time high degree of vacuum level and expensive apparatus. Chemical synthesis, on the other hand, serve as a bottom up method, can offer host of advantages in tailoring NPs' characteristics and potential to obtain large amount of products at comparative cost.[24,25] As the characteristics of NPs are crucial important parameters affecting on the TE properties of their nanostructured materials, the good manipulations on those parameters have received great of interest. Hence, focusing on the chemical methods to control the NPs' characteristics for advanced TE materials, a review is provided for the chemical methods, the key factors to obtain well-defined nanostructure, the capability and current difficulties when using chemical techniques towards NPs for TE applications.

Several chemical synthetic methods have been developed towards NPs for TE applications. The most often used methods are the hydrothermal/solvothermal method with various reducing agents, solvent based reduction method, microwave assisted chemical synthesis (sonochemical method), or the decomposition method.

1.5.1. Thermal decomposition method

In this approach, precursors are typically prepared in the form of single or multiple zero-oxidation-state metal complexes.[26] They are dispersed in an organic solvent with stabilizing (capping) molecules. Around the decomposition temperature of the metal complexes, the elemental precursor atoms undergo nucleation, followed by protection by the capping molecules and subsequent growth of the NPs. In this method, study of the precursor source, decomposition conditions and capping molecules is very important to elucidate the parameters that are required to obtain well-defined NPs.

1.5.2. Hydrothermal method

Hydrothermal synthesis is typically conducted in water at temperatures higher than the boiling point of water in a closed system under pressure (Fig. 1.4).[27-29] For the metal precursor, one can use salts, oxides, hydroxides, or metal/semimetal powders. Various kinds of reducing agents can be introduced into the reaction system ranging from sodium borohydride ($NaBH_4$) or hydrazine (N_2H_4) to organic compounds including oleylamine, ethylene glycol, glucose, formaldehyde or biomolecules. Capping ligands such as oleic acid, oleylamine, dodecanethiol, sodium bis(2-ethylhexyl)sulfosuccinate, L-glutathionic acid, complexing agents [ethylenediaminetetraacetic acid (EDTA), cetyl trimethylammonium bromide (CTAB), etc.], or polymers (polyvinyl pyrrolidone, PVP, polyethylene glycol, etc.) are often employed to stabilize NPs and control the resulting morphology during nucleation and growth. Other synthetic conditions including pH, temperature and reaction time can be modified to obtain monodispersed and uniform NPs.

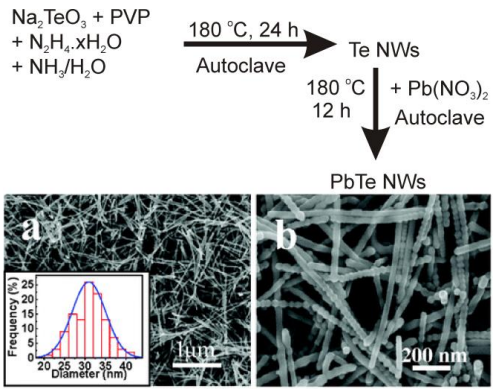

Figure 1.4. Hydrothermal reaction to synthesize PbTe NWs and TEM images of PbTe NWs adapted from ref. 27.

1.5.3. Solvent based reduction method

The solvent based reduction method is similar to the hydrothermal/solvothermal synthesis in terms of reducing agents, capping molecules, solvents and precursors used except for the point that it can be conducted under atmospheric pressure.[30-32] The synthesis is typically performed in an organic solvent such as diphenyl ether, phenyl ether, dioctyl ether or ethylene glycol, at a temperature ranging from room temperature to near the boiling point of the solvent (25-300 ºC). The polyol method is a class of the solvent based synthesis technique that uses a polyol as solvent and reducing agent. The polyol method is a good candidate for synthesizing highly uniform NPs in terms of size, shape and structure.

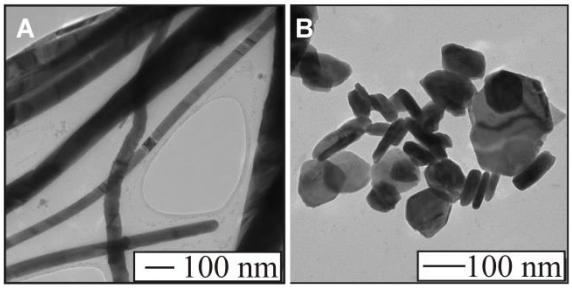

Figure 1.5. TEM images of Bi_2Te_3/Te nanowires and Bi_2Te_3/Sb_2Te_3 nanodiscs synthesized using oleic acid/oleylamine and decanethiol as capping ligands respectively. The images are adapted from ref. 34.

Recently, the solvent based reduction method has proven to be advantageous in control over the size and shape of NPs for TE applications with narrow size distribution.[30] PbSe nanowires (NWs) with various controllable morphologies (zigzags, branches, wires, helical wires) with a diameter that can be tuned from 4 to 20 nm,[30] and very thin $Sb_{2-x}Bi_xTe_3$ nanosheets have been obtained based on this method[33] as well as Bi, Sb, Te containing NPs with different morphology can be produced by changing the capping species (Fig. 1.5).[34] This technique has provided a convenient tool to manipulate the NP morphologies *via* modifying the synthetic conditions, capping systems, reaction steps, and molecular precursor sources. The main disadvantages of this method relates to the existence of organic capping species on the surface of the NPs which strongly affects the surface and TE properties. The complete removal of adsorbed capping species is a challenge and often results in the oxidation of NPs which will reduce σ and the resulting zT value.

1.5.4. Important factors in the synthesis towards well-defined NPs for TE applications

In order to synthesize well-defined NPs for TE applications, the careful control of synthetic conditions is crucially important. For well-defined size and shape NPs, a nano- or micro-scaled template with specific geometry is often required. The "hard template" is based on micro-porous materials which provide confined spaces for the reaction and growth of NPs, defining the final morphology. By using the template-based synthesis method, various kinds of NWs have been synthesized including Bi_2Te_3,[35] PbTe[36] and PbTe/Bi_xTe_{1-x}/PbTe heterostructured dumbbell-like NWs.[37] In another case, templating NPs can be sacrificed themselves for the formation of another kind of NP with different composition but inherited morphology *via* galvanic replacement or Kirkendall effect. For example, Bi_2Te_3 NWs were synthesized using Ni NWs as a template,[37] and Bi_2Te_3 nanotubes (NTs) were fabricated using Te NWs as templates (Fig. 1.6).[38]

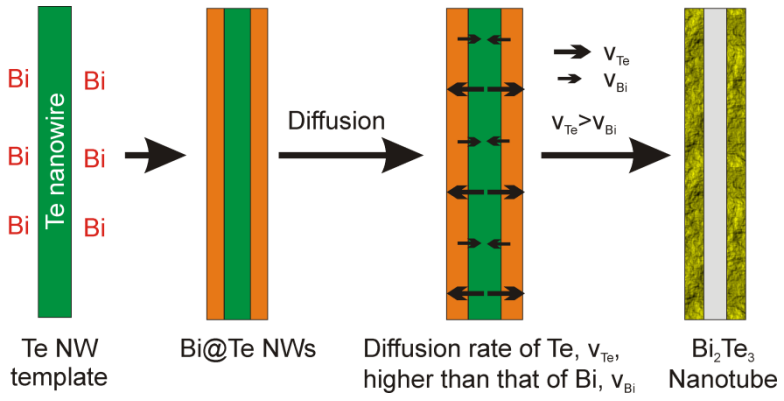

Figure 1.6. Schematic illustration of the chemical method to synthesize Bi_2Te_3 nanotube using Te nanowire (NW) template *via* Kirkindall effect

When capping molecules are used in the synthesis, they can act as a "soft template" to direct the shape formation and play a key role in stabilizing the NPs. At the early stage of the homogeneous nucleation, the capping species selectively adsorb on the thermodynamically-favored surfaces of nuclei, and then, strongly restrict the growth direction of the nuclei to form NPs with specific shape (Fig. 1.7).[39] It was observed that very thin PbTe NWs were grown by the polyol synthesis in the presence of sucrose capping ligands as a soft template, while isotropic PbTe NPs or even bulk PbTe crystals were obtained in the absence of sucrose.[40] There

have been a number of in-depth studies addressing the effect of capping molecules on the size and shape formation of NPs.[39,41,42] Another way that the capping species can be used to direct the particle size and shape formation is through micelles formed from a surfactant[43] or ionic liquid molecules[44] which act as nanoreactors. The organic capping species on the surface of the NPs is crucial not only for manipulating the NP morphology but also for protecting the NPs from uncontrollable aggregation and oxidation which readily occurs once the capping molecules are removed. On the other hand, however, the organic nature of the remaining capping molecules often causes a significant decrease of electrical conductivity which is detrimental to overall TE efficiency, negating the advantages of low dimensional of NPs. Hence, some solutions and modifications have been proposed in order to use capping species to direct the growth of anisotropic NPs while avoiding a decrease in the electrical conductivity. For example, conducting polymers or short alkyl chain molecules have been utilized as capping species to stabilize NPs,[45] and surface organic ligands were extracted and replaced with ammonia[33] or $N_2H_4 \cdot H_2O$[46] offering new approaches to increase the *zT* value of TE materials made from NPs.

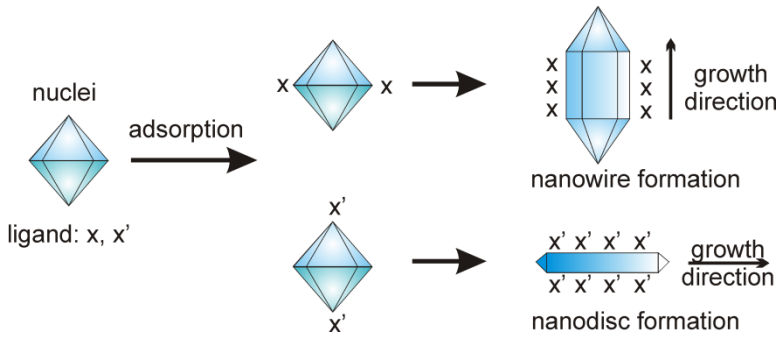

Figure 1.7. Schematic illustration of utilizing capping species to direct the shape formation of NPs *via* control the kinetic growth of NPs in the chemical method

1.5.5. Review on the chemical method to synthesize some representative NPs for TE applications

(Bi,Sb)-(Te,Se) based NPs

(Bi,Sb)-(Te,Se) based NPs can serve as one of the most efficient TE materials near room temperature. The layered crystal structure makes it feasible to grow Bi-Te alloy NPs with anisotropic morphologies.[47] 1D NPs of this system were prepared by surfactant assisted

hydrothermal/solvothermal synthesis,[48] solvent based technique[34,49-55] or the thermal decomposition method.[26] It is notable that, the one dimensional NPs can be obtained for only binary Bi_2Te_3, Sb_2Te_3 but still challenging for ternary BiSbTe alloy NPs due to the difficulty associated with homogenous nucleation, growth and alloying of ternary element, the uniformity of NPs' morphology and composition as well as the stabilization NPs in the synthesis. The knowledge from binary NP synthesis is still useful in understanding the chemical synthesis of BiSbTe containing NPs.

Bi_2Te_3 nanorods (NRs) with a diameter smaller than 80 nm are required to display improved TE efficiency due to the size reduction induced decrease in thermal conductivity.[52] Based on an aqueous solution synthesis at 100 ºC, Ramanath and coworkers demonstrated that the size of Bi_2Te_3 NRs can be tuned by changing the organic capping ligands,[52] for example, using L-cysteine, NRs with an average diameter of 71 nm and length of 470-800 nm were obtained, while their mean diameter and length were reduced to 54 nm and 210-520 nm respectively when using thioglycolic acid as a capping ligand. More complex Bi_2Te_3/BiS core-shell NRs whose lengths and lateral dimension respectively range from 100-4000 nm and 35-290 nm were synthesized by the polyol method using L-glutathionic acid (LGTA) biomolecular surfactant as a capping ligand.[53] Additionally, the kinetic growth of NRs which important to direct the morphology and sizes can be controlled with choosing the appropriate reaction temperature, time and ligand to precursor ratios such as at 140 ºC in the synthesis, wide and long unbranched NRs were obtained at high LGTA/Bi^{3+} ratio, and branched NRs appear at low LGTA/Bi^{3+} ratio while increase the reaction temperature to ca. 195 ºC, longer NRs with branches and macroscopic agglomerates became dominant for short reaction time (5 hours) and for longer reaction time (24 hours), respectively.

One dimensional (Bi,Sb)-(Te,Se) based NWs have received even more interest for high TE efficiency, but it is still a synthetic challenge in terms of producing thin NWs with well-defined crystal structure, high uniformity as well as chemical and mechanical stability. In a typical synthesis of Bi-Te NWs, Te NWs were first formed followed by reduction of Bi precursor in the presence of capping ligands. Based on this approach, Bi_2Te_3 based NWs have been synthesized by hydrothermal or solvent based reduction syntheses[45] with strong reducing agent ($NaBH_4$ or N_2H_4). Bi_2Te_3 based NWs were also synthesized by the thermal decomposition method using tris[bis(trimethylsilyl)amino] bismuth ($Bi[N(SiMe_3)_2]_3$) and Te NW precursors.[26] It is noted that the diameter of the Bi_2Te_3 NWs strongly depends on the synthetic method, i.e., 200-500 nm for the hydrothermal method,[35] 50-85 nm for the thermal

decomposition method[26], and 20-25 nm for the solvent based method using PVP as a capping ligand.[55] Mott *et al.* recently reported a one-pot polyol synthesis of Bi_2Te_3/Te heterogeneous NWs with diameters of 30-50 nm and high aspect ratio using organic capping ligands such as oleic acid and oleylamine.[34]

(Bi,Sb)-(Te,Se) NTs are also promising 1D TE NPs because of their hollow-quasi-1D structure. The synthesis of well-defined NTs by hydrothermal or solvent based methods have been reported as exemplified by Bi_2Se_3 NTs[51] and Bi_2Te_3 NTs.[37,38,48-50,54] The galvanic displacement reaction between Bi^{3+} and $HTeO^{2+}$ ions and Ni NWs as templates was first utilized to form Bi_2Te_3 NTs.[37] The formation of Bi_2Te_3 NTs was promoted by the difference in the reduction potential between Bi and Te precursors and Ni NWs. As another way to synthesize Bi_2Te_3 NTs, the Kirkendall effect, which originates in the difference in diffusion rates of the elements in a solid, has been extensively utilized in hydrothermal or solvent based chemical syntheses.[38,48-50,54] In the syntheses, Te NWs were used as templates and Bi precursor was subsequently added. As the Bi is reduced at the Te NW surface, the Te and Bi begin to diffuse into each other, the higher diffusion rate of Te into Bi causes a void space to form in the center of the wires, creating the hollow NTs (known as the Kirkendall effect). As a result, Bi_2Te_3 NTs were readily synthesized.[38] This method appears to be advantageous in large scale synthesis, uniformity and control of the wall thickness.

The last decade has witnessed the success of various chemical synthetic routes in producing 2D (Bi,Sb)-(Te,Se) based NPs including hexagonal nanoplatelets of Bi_2Te_3, Sb_2Te_3, *n*-type $Bi_2Te_{2-x}Se_x$ and *p*-type $Sb_{2-x}Bi_xTe_3$, nanobelts of Bi_2Se_3 or Sb_2Te_3, $Sb_{2-x}Bi_xTe_3$ nanosheets and heterostructured Bi_2Te_3/Sb_2Te_3 nanodiscs. The chemical synthesis show relatively well control on the binary NPs of Bi_2Te_3, Sb_2Te_3 or Bi_2Se_3 but only few synthesis routes can produce ternary alloy NPs.

Single crystal and highly monodispersed hexagonal shaped Bi_2Te_3 nanoplatelets that are very thin (thickness lower than 15 nm) are formed as a result of surfactant assisted organic solvent based synthesis under well controlled synthetic parameters such as elemental precursor, temperature and synthetic conditions.[56] The resulting Bi_2Te_3 nanoplatelets exhibit the advantages in control of NP characteristics over other chemical methods, such as surfactant assisted hydrothermal/solvothermal synthesis[57-59] and surfactant-free galvanic replacement reaction,[60] where thicker nanoplates (30-50 nm) with larger size distribution are often formed. For example, heterogeneous crystal structures and Bi_2Te_3/Te segregated phases are detected in

the microwave stimulated solvothermal method[61] and microwave assisted galvanic replacement method.[60] In the case of 2D Sb_2Te_3 NPs, the hydrothermal synthesis is the most successful approach,[57,62-64,72] different from the cases of 2D Bi_2Te_3 NPs which could be synthesized by various other synthetic techniques.

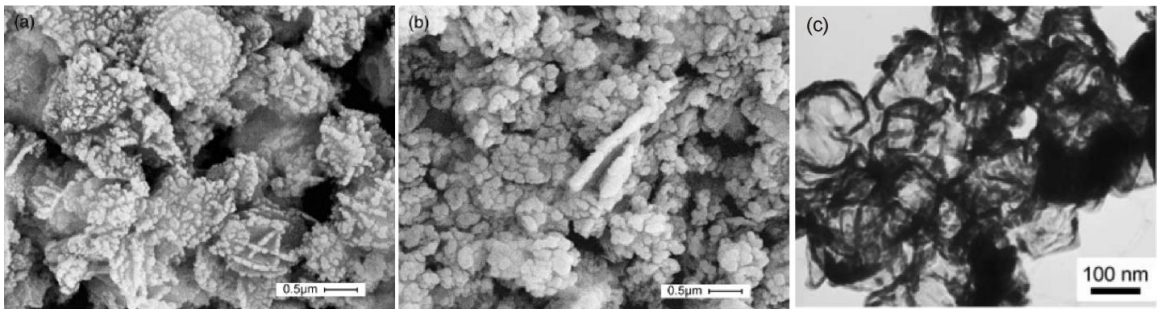

Figure 1.8. SEM images of (a) $Bi_2(Te,Se)_3$, (b) $(Bi,Sb)_2Te_3$ aggregated nanocrystals synthesized by aqueous chemical route adapted from ref. 65 and (c) TEM image of $(Bi,Sb)_2Te_3$ powder by hydrothermal synthesis adapted from ref. 66. All images show submicron non-isolated particles without much control morphology.

It is well known that incorporation of Se or Sb into the Bi_2Te_3 crystal structure can produce *n*- or *p*-type semiconductors respectively with the enhancement of phonon-scattering due to low crystal symmetry, and site occupancy disorder which contributes to the decrease of lattice thermal conductivity, hence, improvement of TE efficiency. With high grain boundary area gained from a nanoscale size, ternary BiSbTe or BiTeSe alloy NPs are expected to scatter heat carried by the phonon much more effectively.[33] However, the chemical synthesis of these ternary alloy NPs has to overcome many challenges evolving from control of the homogeneity of both morphology and composition at the same time. There have been some reports on the formation of BiSbTe NPs *via* hydrothermal approach,[65-67] in which NPs appear highly aggregated in nature, their compositions and crystal structure were not clearly determined and their sizes and shapes were not well controlled. The lack of stabilizing agents[65] and the hydrothermal conditions[66,67] in an one-pot synthetic technique make it difficult to obtain isolated NPs with well-defined morphology as shown in Fig. 1.8.

Recently, Zhang *et al.*[57] modified a solvothermal synthesis using PVP as capping molecules, ethylene glycol as solvent and reducing agent, and NaOH as reaction environment control agent, to synthesize *n*-type Bi_2Te_2Se semiconductor NPs from oxide precursors. The

obtained NPs are hexagonal shaped nanoplatelets with a thickness of 25 nm and edge length of 200-300 nm. The XRD, SAED pattern and HRTEM images reveal nanoplatelets with a single phase and well-defined crystal structure. P-type BiSbTe NPs with true nanosize composed of single phase $Bi_{0.5}Sb_{1.5}Te_3$ (Fig. 1.9 a) has been synthesized *via* a ligand assisted organic solution synthesis developed by Burda *et al.* with the injection of Te-TOP complex into the hot solution of Bi and Sb organometallic precursors, capping ligands, and reducing agent.[68] Although an anisotropic morphology was not achieved, it shows the feasibility of the ligand assisted solution approach in creating low dimensional ternary BiSbTe alloy NPs. However, this method consists of multiple reaction steps and using toxic chemicals, which may limit the practical application.

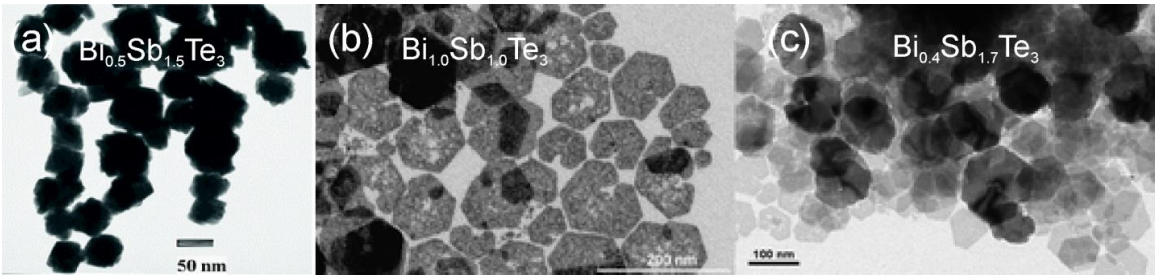

Figure 1.9. TEM images of (a) $Bi_{0.5}Sb_{1.5}Te_{3.0}$ NPs adapted from ref. 68, (b) $Bi_{1.0}Sb_{1.0}Te_{3.0}$ nanosheets and (c) $Bi_{1.7}Sb_{0.4}Te_{3.0}$ nanoplatelets synthesized by ligand assisted solvothermal route adapted from ref. 15.

Taking the advantage point of this approach with some modifications, Weller and coworkers recently succeeded in synthesizing *p*-type $Sb_{2-x}Bi_xTe_3$ nanosheets and nanoplatelets which have elemental composition of $Bi_{1.0}Sb_{1.0}Te_{3.0}$ (Bi:Sb = 1:1) and $Bi_{1.7}Sb_{0.4}Te_{3.0}$ (Bi:Sb = 4:1) respectively (Fig. 1.9 b and c).[15] The morphology and structure of these 2D NPs are sensitive to the reaction temperature. At moderate reaction temperature (ca. 60 ºC), the formation of thin nanostructures occurs followed by their combination to form larger structures, so-called "nanosheets". Nanosheets are very thin (thickness of about 5 nm) and ranges from 50-200 nm in edge length. Futhermore, nanosheets have a single crystalline structure revealing the perfect alignment of the thin nanostructures in a specific crystalline direction during the reaction. At higher reaction temperature (90 ºC), the thickness of the nanosheets increased to 15-20 nm which are referred to "nanoplatelets". The transformation of nanosheets to nanoplatelets with an increase in thickness is due to growth in the *c*-axis direction initiated by

an increase in reaction temperature. This method opened the way to chemically grow well-defined NPs for highly efficient TEs. Even though this is the only successful wet-synthesis of 2D BiSbTe ternary alloy, it is still limited in the type of NPs (with certain morphology and composition) the method can produce and exhibits how challenging it is to create ternary alloy NPs.

In summary, various chemical synthesis techniques are demonstrated the capability of creating well-defined binary NPs of (Bi,Sb)-(Te,Se) based system. The formation and effect of synthetic parameters on the resulting NPs dimensions and nanostructure have been somewhat elucidated. On the other hand, the synthesis of ternary BiSbTe and BiTeSe alloy NPs is very challenging work in term of creating true NPs, controllable morphology, composition and structure with high uniformity and homogeneity simultaneously. Moreover, synthesis techniques succeeded in formation of BiSbTe alloy NPs can lead to only one specific type of NP in terms of shape or structure, making these techniques very limited in the range of NPs they can produce. Part of these difficulties arises from the lack understanding of the formation of NPs in the tri-elemental NPs due to the complexity occurs in the reaction of tri-elemental precursors in which not only the effect of surfactant but also other factors such as relative reaction rate or interaction of the two or three elemental precursors, the alloying… on the growth of NPs. Therefore, further study on the formation of ternary alloy NPs is required to well control NPs' characteristics and to be able to expand the chemical synthesis to obtain, such as ternary BiSbTe NWs or BiSbTe NPs with tunable morphology and composition.

Pb-(Te,Se) system

Pb-(Te,Se) materials possess very high *zT* value at an intermediate temperature (the maximum *zT* value occurs at about 430 ^{o}C). PbTe quantum dot superlattices show improved TE efficiency compared to the bulk.[69] One-dimensional PbTe NPs with an enhanced Seebeck coefficient were experimentally and theoretically proven to give a comparable *zT* value with PbTe/PbSe$_x$Te$_{1-x}$ superlattices.[70] The chemical synthesis of 1D Pb-(Te,Se) NPs required strict control of the reaction conditions. Recently, 1D PbTe and PbSe NPs were successfully synthesized using the hydrothermal method and solvent based synthesis method with the aid of shape directing surfactants.[27,29-32]

Hydrothermal synthesis in an one-pot reaction at high temperature (ca. 200 ^{o}C) using N_2H_4 or $NaBH_4$ as reducing agents with or without different surfactants has been widely applied for the synthesis of 1D PbTe NPs.[27,29,71-73] However, the resulting NPs often have

relatively large diameters of 30-100 nm. The formation of 1D PbTe with various morphologies such as NRs, NTs and NWs and sizes was reported depending on the amount of surfactant (eg. CTAB)[72] or the reaction environment (mixed hydroxides of NaOH and KOH).[72,73] For better control of 1D NP size and shape, a two-step synthetic route was developed in which Te NWs were first synthesized, and then PbTe NWs were formed by alloying of the Te NWs. The resulting PbTe NWs displayed pearl-necklace shape with the average external diameter of the PbTe NWs was about 30 nm, which is smaller than the exciton Bohr radius of PbTe crystal (ca. 46 nm).[27] Several phenomena may govern the formation of pearl-necklace-shaped NWs including the higher diffusion coefficient of Pb than Te resulting in the fracture of Te NWs in the transformation process from trigonal Te NWs to face-centered-cubic (*fcc*) PbTe NWs, the oriented attachment of existing dot-shaped NPs along a given crystal orientation, the dipole-dipole interaction between PbTe nanocrystals, and/or the selective protecting effect of pyrrolidone (PVP) capping molecules. Varying the reaction temperature, reaction time and concentration of Pb precursor, uniform and smooth PbTe NWs with a diameter ranging from 20 to 40 nm and length from several to 100 μm were obtained.[29] Towards the NT morphology, till now, there are few reports on the chemical synthesis of PbTe NTs *via* hydrothermal synthesis.[74,75] Modified polyol synthesis with the injection of precursor solutions into sucrose containing-hot pentandiol solvent (180-210 ºC) has also succeeded to produce PbTe NWs.[39] The advantages of this method include creating very thin PbTe NWs and tunability of the NW size *via* the shape directing effect of sucrose based on the π-π interaction of hydroxyl groups in these molecules with Pb in the PbTe to form a stacking template in the solution. Sometimes chemical synthesis techniques offer flexible ways to tailor the morphology of 1D PbTe NPs. For example, PbTe NRs can be synthesized using Te NTs as templates.[76]

1D PbSe NPs have also been deeply investigated in terms of chemical synthesis technique, formation mechanism, assembly and electronic properties.[30-32] Solvent based methods are typically used for PbSe NW synthesis. Cho and coworkers synthesized PbSe NWs by injecting precursors [lead acetate trihydrate/oleic acid and Se-trioctylphosphine (TOP)/TOP] into diphenyl ether at 250 ºC.[30] Talapin and coworkers tailored the morphology of the resulting NWs including straight, zigzag, helical and branched forms using surfactants as shape-directing agents.[31] Their observation suggested that the resulting NWs were formed as a result of spontaneous alignment and fusion of cubic PbSe NPs along the (100) axis. This process refers to the oriented attachment mechanism which creates highly anisotropic NWs from nanodot building blocks. Higher feeding ratios of Pb to Se resulted in a branched

morphology. Use of *n*-tetradecylphosphonic acid as a capping ligand resulted in straight and uniform NWs, while addition of long-chain aliphatic amines gave zigzag-shaped NWs. Talapin *et al.* has further developed this technique to prepare more complex-shaped PbSe/PbS core-shell NWs, or to decorate PbSe NWs with Au NPs.[32] Core-shell NWs with a tunable shell thickness are interesting in terms of controlling the TE properties. Complex heterostructured NWs can become a new candidate for TE materials with novel and tunable characteristics.

There have been few reports on the chemical synthesis of 2D PbTe or PbSe NPs due to the challenges in anisotropic growth of the highly symmetric cubic crystal structure of this system. Even though, some groups have successfully synthesized 2D PbTe or PbSe nanosheets with thickness of 20-80 nm using an alkaline hydrothermal route in the presence of PVP.[78,79] A time-dependent study suggested that nanosheet formation in this system is also related to the spontaneous arrangement and alignment of Pb-(Te,Se) nanocrystals *via* an oriented attachment mechanism and form a single crystal upon fusion of the nanocrystals,[78] which is consistent with the previous observation in 1D Pb-(Te,Se) NPs.[27,29-32]

Zn-Sb system

ZnSb compounds are representative for a class of the rare-earth-element-free compounds with high *zT* value at an intermediate temperature range from 200 ^{o}C to near 400 ^{o}C.[80] Zn_4Sb_3 shows the maximum *zT* value of 1.3 at about 600 K, which can be a promising substitute for PbTe with the advantage of Pb and Te free. Zn_4Sb_3 has very low thermal conductivity arising from the complex structure and the disorder interstitial Zn in the crystal structure.[80-84] Zn_4Sb_3 or ZnSb were mostly prepared *via* physical methods such as ball-milling,[85] mechanical alloying,[86] zone melting,[87] spark plasma sintering,[88] and hot-pressing.[89] The TE properties of Zn-Sb can be tuned with doping of a third element into ZnSb bulk crystal to enhance the TE efficiency.[90-92]

Nanostructuring of TE materials enables the reduction of thermal conductivity while retaining the electrical conductivity, and thus, leads to an enhancement in TE efficiency. However, a few chemical approaches toward Zn-Sb nanostructures have been proposed.[93-96] For example, Zn@Sb core-shell particles were synthesized first, and then, nanostructured Zn-Sb compound was formed by annealing Zn@Sb core-shell particles at 300 ^{o}C for 6 hours.[93] In this method, the crystal growth occurs during longer heating periods, and thus, undesirable grain growth cannot be avoided during the reaction. In another approach, based on the solid

state reaction of activated powders of Zn and Sb pioneered by Schlecht et al.,[94] Tremel and coworkers developed a new synthetic method to obtain Zn-Sb NPs *via* a peritectoid reaction between differentially-synthesized Zn and Sb NPs in an organic solvent at about 300 ^{o}C (Fig.1.10).[95,96] In this case, it is also somewhat difficult to control the grain size, which is crucially important for TE properties, because coalescence of the NPs takes place during the peritectoid reaction. In either case, it isn't possible to synthesize well-defined Zn-Sb NPs in terms of morphology and uniformity. Even though, these results indicate that the chemical synthesis are able to use for obtaining Zn-Sb compounds and they encourage the further study on the preparation of Zn-Sb compounds with better control on the nano-structure.

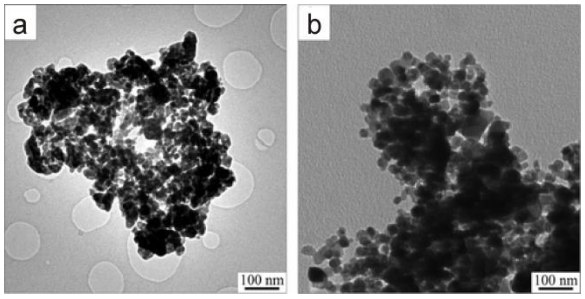

Figure 1.10. TEM images of Zn_4Sb_3 NPs obtained from the synthesis in solution adapted from ref. 95.

Quasi three dimensional TE materials

Beside the NPs, the chemical synthesis was found to be able to create quasi three-dimensional (3D) TE materials which have micro-scale dimensions but are composed of nanostructured building blocks such as aligned Bi_2Te_3 nanoplatelet-Te NR heterogeneous structures or string-cluster hierarchical structured Bi_2Te_3 nanoplatelets.

The first example in this section is the complex structure of aligned Bi_2Te_3 nanoplatelets on Te NRs first reported by Lu *et al.*.[56] In the attempt to synthesize *n*-type semiconductor NPs by simply adding a small amount of Se-TOP into the surfactant-solution synthesis reaction of Bi_2Te_3 nanoplatelets, they happened to obtain complex nanostructures in which strings of nanoplatelets growing out of the NRs attached at the NR edges. The alignment of nanoplatelets exhibits a very well controlled reaction which reveals the specific crystal orientation

relationship. The detailed composition correlated with morphology analysis suggested that the NRs are composed of Te, while the nanoplatelets are made of Bi_2Te_3. Furthermore, the crystal characterization at the interface of the nanoplatelets and the NR shows the *c*-axis of the nanoplatelets parallel to the *c*-axis of the NRs indicating an expitaxial orientation relationship between nanoplatelets and NRs. Therefore, the string of aligned Bi_2Te_3 nanoplatelets on Te NRs occurred as a result of epitaxial growth of Bi_2Te_3 on Te NRs. The formation of Te NRs may relate to the lower stability of Te-TOP compared to Se-TOP at high temperature. These complex structures are very interesting for several reasons: first, the assembly of 2D NPs has not met with much success until now, and thus, the understanding of the formation mechanism may open new approaches to control and tailor anisotropic building blocks into higher-order structures; second, the higher-order nanostructures may result in enhancement of TE efficiency as well.

The above mentioned primary results of well aligned Bi_2Te_3 nanoplatelets grown out of Te nanorods feature the perfect alignment of 2D structures into strings. However, these complex nanostructures still possess heterogeneity in their structure and composition. A finer study on a hydrothermal synthesis of BiTe nanoplatelets conducted by Mi and coworkers resulted in the same string-alignment pattern of resulting nanoplatelets with homogeneous structure, composition and even longer range ordering.[97] The platelets align into strings and these strings connect to form clusters with hierarchical structures. It is very important to point out that these hierarchical structures were built up from only nanoplatelets and the structure-composition analysis confirmed that they are single crystal Bi_2Te_3. Based on the time-dependent study, the formation of Te NWs were observed in the course of the reaction which was followed by the epitaxial growth of Bi_2Te_3 nanoplatelets which is consistent with the mechanism proposed by Lu *et al.*.[56] If the hydrothermal synthesis is prolonged for 24 hours, Te NRs were also found to be consumed during the development of Bi_2Te_3 nanoplatelets. The Te NRs act as intermediate templates that transfer their patterns into the strings of Bi_2Te_3 nanoplatelets which were aligned with a specific orientation. The strings of nanoplatelets then connect to each other *via* the combination of nanoplatelets to form the cluster of strings with hierarchical structure (arrays). The formation mechanism of these string-clusters of nanoplatelets can happen with smaller nanoplatelets and the different intermediate templates can result in different ordered arrays of NPs. These results can be used to study the self assembly of 2D TE NPs and contribute to further study on the design of higher-order nanostructured quasi 3D TE materials.

1.5.6. Thermoelectric properties of nanostructured TE materials synthesized using chemical methods

The low-dimensional TE materials are expected to have an enhanced power factor, $\alpha^2\sigma$, due to the shaft feature in the electronic density of states originating from a quantum confinement effect. Therefore, the enhancement of α in 1D materials is considered to be one of the important factors for the improvement in overall zT value arising from low dimensionality. Even though from NP building blocks to nanostructured materials, a lot of challenges need to overcome such as the large amount of NPs required, surface treatment and pressing/sintering conditions for maintain the nanostructure in the 3D materials, some research group succeeded in demonstrate the enhanced TE properties of nanostructured materials with NP building blocks synthesized *via* chemical route.

Purkayastha *et al.* reported that the room-temperature α of PbTe NRs with a diameter of 66 ± 12 nm was 263 μV/K, which is almost the same value as that for bulk PbTe crystal.[76] This would be due to the larger mean diameter of the PbTe NRs than the exciton Bohr radius of PbTe crystal (ca. 46 nm), which cannot exhibit a strong quantum confinement effect. On the other hand, the pearl-necklace-shaped PbTe NWs with smaller mean diameter (ca. 30 nm) showed a significant improvement of the Seebeck coefficient (α = 307 μV/K), which is 16% higher than that of the bulk counterpart at room temperature.[27] PbTe NWs with even smaller diameter (< 30 nm) yielded about 80% enhancement in α (~ 470 μV/K) compared to the bulk PbTe in the temperature range of 375-425 K.[40]

More importantly, the main purpose in using low-dimensional TE NPs as building blocks for TE devices to improve zT value is significant reduction in κ. By fabricating TE devices using TE type NPs as building blocks, one can easily create a phonon scattering/carrier transmission structure utilizing grain boundaries among NPs. The thermal conductivity of the pellets fabricated from $Sb_{1.7}Bi_{0.4}Te_{3.0}$ nanoplatelets by spark plasma sintering is found to be dramatically reduced, especially in the lattice thermal conductivity (60% lower than that of its bulk counterpart).[33] The electrical conductivity, σ, of pelletized $Sb_{1.7}Bi_{0.4}Te_{3.0}$ nanoplatelets was also found to be reduced compared to those of the bulk counterpart. However, the reduction in κ is much larger than that in σ, and thus, the zT value is increased to over 15% higher than that of the bulk counterpart. The enhancement of the zT value has also been reported for the Bi_2Te_3-Te micro-nano heterostructure.[61]

In summary, the results of enhanced TE properties of nanostructured TE materials with NP building block synthesized *via* chemical techniques are important step on the way to use NPs for TE application. Again, a suitable surface treatment, maintaining nanostructure, attempting high density materials with good electrical contact and so on are still raising a lot of difficulties for creating a good nanostructured TE materials from NP building blocks.

1.6. Research Objective

Nanostructured materials have been proved as one of the most promising approaches to improve efficiency of the state of the art TE materials. The studies on the chemical synthesis and TE properties of Bi-Te, Pb-Te and Zn-Sb based NPs demonstrated a great potential of creating NPs as advanced materials for TE applications. At the same time, there were pointed out many challenges remaining as reviewed for BiSbTe ternary alloy NPs and ZnSb NPs which are mainly associated with (i) the lack of understanding the formation mechanism of the BiSbTe ternary alloy NPs or solution growth of ZnSb NPs, (ii) synthesis route and conditions to get NPs with high uniformity, controllable composition, structure, morphology and other properties simultaneously, (iii) scale-up the chemical synthesis, surface treatment of NPs and creation of nanostructured materials using NPs as the building blocks, study the thermoelectric properties, and the relationship between the TE properties and the NPs' characteristics such as size, shape and so on.

My research has been devoted to address the mentioned challenges of chemical synthesis of BiSbTe ternary solid solution and Zn_4Sb_3 NPs because of several reasons: firstly, their bulk counterparts are well known for the high TE performance at near room temperature (< 250 ^oC) and moderate temperature (200-400 ^oC) respectively in which BiSbTe is representative of a p-type SC containing Te while Zn_4Sb_3 contains abundant elements; and secondly, nanostructuring of the materials is promising for TE applications. However, the chemical synthesis of these NPs is challenging in terms of control NP characteristics including composition and nanostructure, which are important for improving the TE efficiency. This research aims to offer scalable, economically comparative and environmentally friendly syntheses with capability of creating compounds and alloys with tailorable characteristics in the nanoscale regime for TE applications.

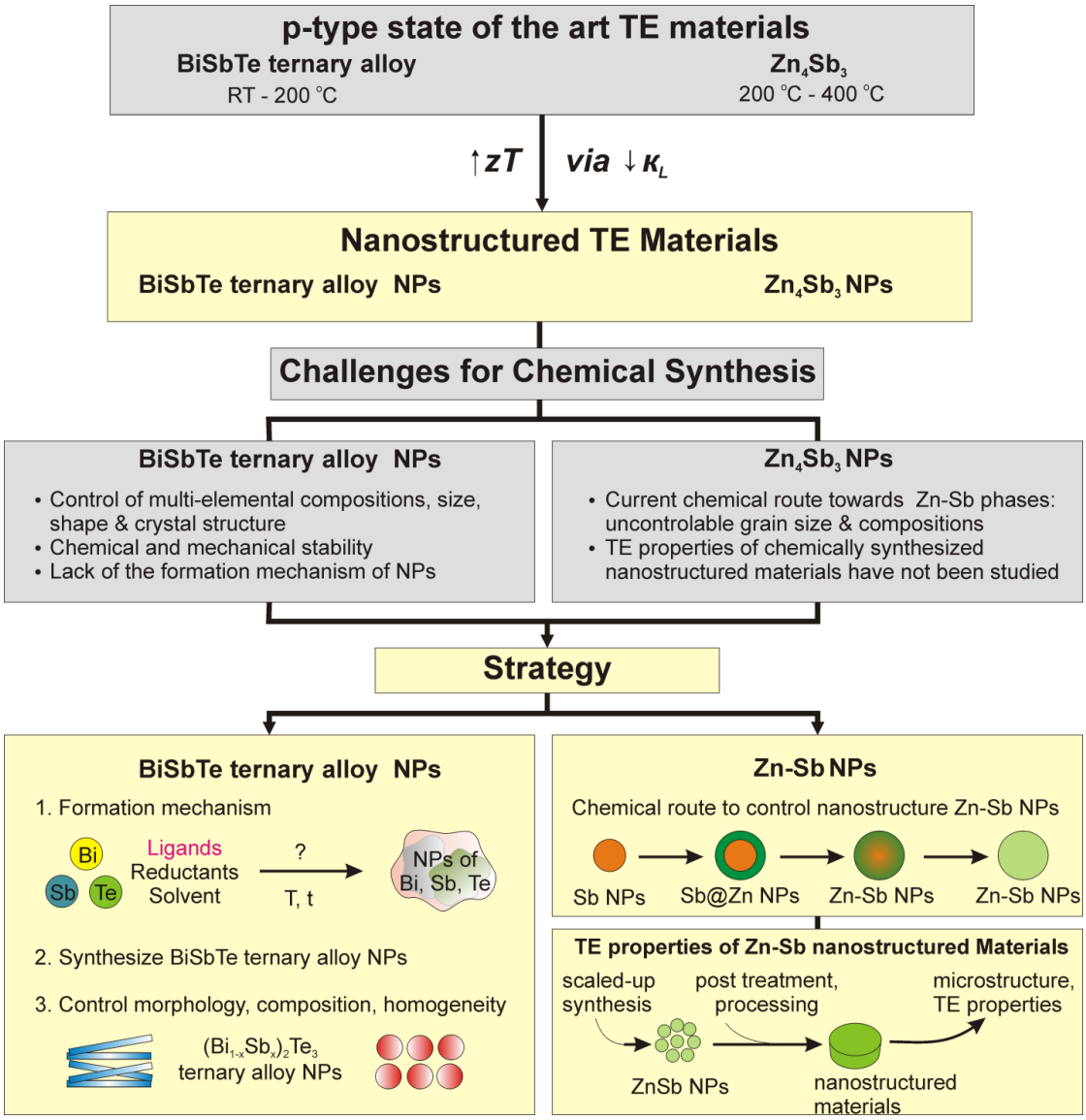

Figure 1.11. Summary of the issues and research objectives

In detail, my research will address the following aspects (Fig. 1.11):

(1) Investigation of the formation of BiSbTe containing NPs to manipulate the NP's characteristics: nanostructure and composition.

(2) Synthesis of BiSbTe ternary NPs with controllable composition and nanostructure

(3) Design a chemical route towards Zn-Sb NPs with defined nanostructure served as building blocks for TE nanomaterials

(4) Study on the scaling up reaction, creation of nanostructured TE materials, and the TE properties of nanostructured TE materials with a case study of Zn-Sb NPs.

Following the introduction, the thesis continues with another 4 chapters for the results obtained from my research in which chapter 2 and 3 are for the study of BiSbTe ternary solid solution NPs and chapter 4 and 5 are devoted for the research on chemical synthesis of Zn-Sb NPs and the TE properties of the Zn-Sb nanostructured materials. The conclusion and highlight of the contribution and prospects of the research are given in chapter 6. In more detail:

Chapter 2. The chemical synthesis, characterization and formation mechanism of BiSbTe NPs with various morphologies and compositions. This study is important due to the fact that the formation of ternary BiSbTe NPs are complicated and not been elucidated in the literature. Additionally, few chemical syntheses succeeded in the formation of single phase BiSbTe NPs are limited in the type of NP morphology they can produce. The understanding of ternary solid solution NPs formation and synthesis could help to create NPs with better control of NPs characteristics. Because of the complex interaction of capping species with elemental precursors, nuclei and NPs during the nucleation and growth of NPs during the formation of ternary solid solution NPs, the research performed a systematic investigation of NP formation in mono-, bi-, and tri-elemental synthesis with different type of capping system to elucidate the formation details of BiSbTe ternary NPs.

Chapter 3. Based on the mechanism elucidated in chapter 2, the seed mediated growth of BiSbTe based NPs were developed which mainly focuses on the manipulation of the seed NPs' composition in order to manipulate the BiSbTe ternary alloy NPs' composition. In this chapter, BiSb NPs with various compositions and platelet like morphology were synthesized. The BiSb NPs are used as the seeds, Te was reduced and growth on the seeds, followed by the alloying to form BiSbTe NPs. By this method, the study exhibits a control on NPs' morphology and composition.

Chapter 4. One pot chemical synthesis of Zn-Sb NPs was investigated. Because the successful solution syntheses of Zn_4Sb_3 NPs are based on peritectod reaction which in general relies on the formation of new phase (Zn_4Sb_3) from Zn and Sb NPs in the solution at high temperature to form Zn_4Sb_3 NPs, the method is not fully capable of producing isolated NPs with well-defined nanostructure and surface properties. Therefore, in this chapter, a multiple step reaction was designed with the formation of Sb seed NPs, the reduction and growth of Zn on the seed and followed by the alloying to obtain Zn-Sb NPs with better control over the morphology. The resulting Zn-Sb NPs which display high uniformity and complex nanostructure were carefully characterized in addition to assessment of the Seebeck coefficient conducted on the powder sample of these NPs.

Chapter 5. The TE properties of Zn-Sb nanostructured materials are necessary to study. For that purpose, a large amount of Zn-Sb NPs are required to make a large scale pellet. Therefore, scaling up the chemical reaction of Zn-Sb NPs and using these NPs to make the nanostructured pellet to study their TE properties will be presented in this chapter.

References

[1] D. M. Rowe, *CRC Handbook of Thermoelectrics*, CRC Press, **1994**.

[2] D. M. Rowe, *Thermoelectrics Handbook: Macro to Nano*, CRC Press, Boca Raton, Florida, **2006**.

[3] T. M. Tritt, *Recent Trends in Thermoelectric Materials Research*, in *Semiconductors and Semimetals*, Academic Press, CA, **2001**.

[4] T. M. Tritt, *Annu. Rev. Mater. Res.* **2011**, *41*, 433.

[5] G. J. Snyder, E. S. Toberer, *Nat. Mater.* **2008**, *7*, 105.

[6] S. B. Riffat, X. Ma, *Appl. Therm. Eng.* **2003**, *23*, 913.

[7] M. G. Kanatzidis, *Chem. Mater.* **2010**, *22*, 648.

[8] A. F. Ioffe, S. V. Airapetyants, A. V. Ioffe, N. V. Kolomoets, L. S. Stil'bans, *Dokl. Akad. Nauk. SSSR* **1956**, *106*, 981.

[9] G. A. Slack, *In CRC Handbook of Thermoelectrics*, ed. by D. M. Rowe, p. 147, CRC Press, Boca Raton, FL **1995**.

[10] B. Qiu, H. Bao, G. Zhang, Y. Wu, X. Ruan, *Comput. Mater. Sci.* **2012**, *53*, 278.

[11] G. S. Nolas, J. L. Cohn, G. A. Slack, *Phys. Rev. B* **1998**, *58*, 164.

[12] G. A. Slack, V. G. Tsoukala, *J. Appl. Phys.* **1994**, *76*, 1665.

[13] G. S. Nolas, D. T. Morelli, T. M. Tritt, *Ann. Rev. Mater. Sci.* **1999**, *29*, 89.

[14] L. D. Hick, T. C. Harman, M. S. Dresselhaus, *Appl. Phys. Lett.* **1993**, *63*, 3230.

[15] L. D. Hicks, M. S. Dresselhaus, *Phys. Rev. B* **1993**, *47*, 12727.

[16] C. J. Vineis, A. Shakouri, A. Majumdar, M. G. Kanatzidis, *Adv. Mater.* **2010**, *22*, 3970.

[17] R. Venkatasubramanian, E. Siivola, T. Colpitts, B. O'Quinn, *Nature* **2001**, *413*, 597.

[18] T. C. Harman, W. P. Walsh, B. E. Laforge, G. W. Turner, *J. Electron. Mater.* **2005**, *34*, 19.

[19] A. I. Hochbaum, P. Yang, *Chem. Rev.* **2010**, *110*, 527.

[20] Y. Lan, A. J. Minnich, G. Chen, Z. Ren, *Adv. Funct. Mater.* **2010**, *20*, 357.

[21] J. Liu, G. Cao, Z. Yang, D. Wang, D. Dubois, X. Zhou, G. L. Graff, L. R. Pederson, J.-

G. Zhang, *ChemSusChem* **2008**, *1*, 676.

[22] P. Pichanusakorn, P. Bandaru, *Mater. Sci. Eng. R* **2010**, *67*, 19.

[23] A S. K. Bux, J.-P. Freurial, R. B. Kaner, *Chem. Commun.* **2010**, *46*, 8311.

[24] J. S. Son, M. K. Choi, M.-K. Han, K. Park, J.-Y. Kim, S. J. Lim, M. Oh, Y. Kuk, C. Park, S.-J. Kim, T. Hyeon, *Nano Lett.* **2012**, *12*, 640.

[25] Y. Zhang, L. P. Hu, T. J. Zhu, J. Xie, X. B. Zhao, *Cryst. Growth. Des.* **2013**, *13*, 645.

[26] H. Yu, P. C. Gibbons, W. E. Buhro, *J. Mater. Chem.* **2004**, *14*, 595.

[27] G. Tai, W. Guo, Z. Zhang, *Cryst. Growth Des.* **2008**, *8*, 2906.

[28] W. Z. Wang, B. Poudel, D. Z. Wang, Z. F. Ren, *Adv. Mater.* **2005**, *17*, 2110.

[29] G. Tai, B. Zhou, W. Guo, *J. Phys. Chem. C* **2008**, *112*, 11314.

[30] K.-S. Cho, D. V. Talapin, W. Gaschler, C. B. Murray, *J. Am. Chem. Soc.* **2005**, *127*, 7140.

[31] D. V. Talapin, C. T. Black, C. R. Kagan, E. V. Shevchenko, A. Afzali, C. B. Murray, *J. Phys. Chem. C* **2007**, *111*, 13244.

[32] D. V. Talapin, H. Yu, E. V. Shevchenko, A. Lobo, C. B. Murray, *J. Phys. Chem. C* **2007**, *111*, 14049.

[33] M. Scheele, N. Oeschler, I. Veremchuk, K.-G. Reinberg, A.-M. Kreuziger, A. Kornowski, J. Broekaert, C. Klinke, H. Weller, *ACS Nano* **2010**, *4*, 4283.

[34] D. Mott, N. T. Mai, N. T. B. Thuy, Y. Maeda, T. P. T. Linh, M. Koyano, S. Maenosono, *Phys. Status Solidi A*, **2011**, *208*, 52.

[35] J.-J. Kim, S.-H. Kim, S.-W. Suh, D.-U. Choe, B.-K. Park, J.-R. Lee, Y.-S. Lee, *J. Cryst. Growth* **2010**, *312*, 3410.

[36] G. Zhang, Q. Yu, W. Wang, X. Li, *Adv. Mater.* **2010**, *22*, 1959.

[37] F. Xiao, B. Yoo, K. H. Lee, N. V. Myung, *J. Am. Chem. Soc.* **2007**, *129*, 10068.

[38] G. Zhang, Q. Yu, Z. Yao, X. Li, *Chem. Commun.* **2009**, 2317.

[39] C. Burda, X. Chen, R. Narayanan, M. A. El-Sayed, *Chem. Rev.* **2005**, *105*, 1025.

[40] Q. Yan, H. Chen, W. Zhou, H. H. Hng, F. Y. C. Boey, J. Ma, *Chem. Mater.* **2008**, *20*, 6298.

[41] M. P. Pileni, *J. Phys. Chem. C.* **2007**, *111*, 9019.

[42] D. V. Talapin, J.-S. Lee, M. V. Kovalenko, E. V. Shevchenko, *Chem. Rev.* **2010**, *110*, 389.

[43] A. Purkayastha, S. Kim, D. D. Gandhi, P. G. Ganesan, T. Borca-Tasciuc, G. Ramanath, *Adv. Mater.* **2006**, *18*, 2958.

[44] J. Jiang, S.-H. Yu, W.-T. Yao, H. Ge, G.-Z. Zhang, *Chem. Mater.* **2005**, *17*, 6094.

[45] K. C. See, J. P. Feser, C. E. Chen, A. Majumdar, J. J. Urban, R. A. Segalman, *Nano Lett.* **2010**, *10*, 4664.

[46] M. Scheele, N. Oeschler, K. Meier, A. Kornowski, C. Klinke, H. Weller, *Adv. Funct. Mater.* **2009**, *19*, 3476.

[47] D. Teweldebrhan, V. Goyal, A. A. Balandin, *Nano Lett.* **2010**, *10*, 1209.

[48] X. B. Zhao, X. H. Ji, Y. H. Zhang, T. J. Zhu, J. P. Tu, X. B. Zhang, *Appl. Phys. Lett.* **2005**, *86*, 062111-1-3.

[49] S. H. Kim, B. K. Park, *J. Appl. Phys.* **2010**, *108*, 102808-1-5.

[50] S. H. Kim, B. K. Park, *Mater. Lett.* **2010**, *64*, 938.

[51] H. Cui, H. Liu, X. Li, J. Wang, F. Han, X. Zhang, R. I. Boughton, *J. Solid State Chem.* **2004**, *117*, 4001.

[52] A. Purkayastha, F. Lupo, S. Kim, T. Borca-Tasciuc, G. Ramanath, *Adv. Mater.* **2006**, *18*, 496.

[53] A. Purkayastha, Q. Yan, M. S. Raghuveer, D. D. Gandhi, H. Li, Z. W. Liu, R. V. Ramanujan, T. Borca-Tasciuc, G. Ramanath, *Adv. Mater.* **2008**, *20*, 2679.

[54] Y. Q. Cao, T. J. Zhu, X. B. Zhao, *J. Alloys Compd.* **2008**, *449*, 109.

[55] G. Zhang, W. Wang, X. Li, *Adv. Mater.* **2008**, *20*, 3654.

[56] W. Lu, Y. Ding, Y. Chen, Z. L. Wang, J. Fang, *J. Am. Chem. Soc.* **2005**, *127*, 10112.

[57] G. Zhang, W. Wang, X. Lu, X. Li, *Cryst. Growth Des.* **2009**, *9*, 145.

[58] Y. Xu, Z. Ren, G. Cao, W. Ren, K. Deng, Y. Zhong, *Mater. Lett.* **2008**, *62*, 4525.

[59] Y. Deng, C.-W. Nan, G.-D. Wei, L. Guo, Y.-H. Lin, *Chem. Phys. Lett.* **2003**, *374*, 410.

[60] Y. Zhang, H. Wang, S. Kräemer, Y. Shi, F. Zhang, M. Snedaker, K. Ding, M. Moskovits, G. J. Snyder, G. D. Stucky, *ACS Nano* **2011**, *5*, 3158.

[61] R. J. Mehta, C. Karthik, B. Singh, R. Teki, T. Borca-Tasciuc, G. Ramanath, *ACS Nano* **2010**, *4*, 5055.

[62] W. Wang, B. Poudel, J. Yang, D. Z. Wang, Z. F. Ren, *J. Am. Chem. Soc.* **2005**, *127*, 13792.

[63] W. Wang, D. Long, Y. Liang, G. Zhang, B. Zeng, Q. He, *Langmuir* **2011**, *27*, 815.

[64] W. Shi, J. Yu, H. Wang, H. Zhang, *J. Am. Chem. Soc.* **2006**, *128*, 16490.

[65] Y. Xu, Z. Ren, W. Ren, K. Deng, Y. Zhong, *Mater. Lett.* **2008**, *62*, 763.

[66] Y. Q. Cao, T. J. Zhu, X. B. Zhao, X. B. Zhang, J. P. Tu, *Appl. Phys. A: Mater. Sci. Process.* **2008**, *92*, 321.

[67] X. H. Ji, X. B. Zhao, Y. H. Zhang, B. H. Lu, H. L. Ni, *Mater. Lett.* **2005**, *59*, 682.

[68] Y. Zhao, C. Burda, *ACS Appl. Mater. Interfaces* **2009**, *1*, 1259.

[69] T. C. Harman, P. J. Taylor, M. P. Walsh, B. E. Laforge, *Science* **2002**, *297*, 2229.

[70] J. P. Heremans, C. M. Thrush, D. T. Morelli, *Phys. Rev. B* **2004**, *70*, 115334-1-5.

[71] L. Z. Zhang, J. C. Yu, M. S. Mo, L. Wu, K. W. Kwong, Q. Li, *Small* **2005**, *1*, 349.

[72] B. Wan, C. Hu, H. Liu, Y. Xiong, F. Li, Y. Xi, X. He, *Mater. Res. Bull.* **2009**, *44*, 1846.

[73] B. Wan, C. Hu, B. Feng, Y. Xi, X. He, *Mater. Sci. Eng. B* **2009**, *163*, 57.

[74] G. Zou, Z. Liu, D. Wang, C. Jiang, Y. Qian, *Eur. J. Inorg. Chem.* **2004**, *22*, 4521.

[75] H. Tong, Y.-J. Zhu, L.-X. Yang, L. Li, L. Zhang, *Angew. Chem. Int. Ed.* **2006**, *45*, 7739.

[76] A. Purkayastha, Q. Yan, D. D. Gandhi, H. Li, G. Pattanaik, T. Borca-Tasciuc, N. Ravishankar, G. Ramanath, *Chem. Mater.* **2008**, *20*, 4791.

[77] G. D. Moon, S. Ko, Y. Xia, U. Jeong, *ACS Nano* **2010**, *4*, 2307.

[78] T. P. Zhu, X. Chen, X. Y. Meng, X. B. Zhao, J. He, *Cryst. Growth Des.* **2010**, *10*, 3727.

[79] X. Wang, G. Xi, Y. Liu, Y. Qian, *Cryst. Growth Des.* **2008**, *8*, 1406.

[80] G. J. Snyder, M. Christensen, E. Nishibori, T. Caillat, B. B. Iversen, *Nat. Mater.* **2004**, *3*, 458.

[81] L. Bjerg, G. K. H. Madsen, B. B. Iversen, *Chem. Mater.* **2011**, *23*, 3907.

[82] F. Cargnoni, E. Nishibori, P. Rabiller, L. Bertini, G. J. Snyder, M. Christensen, C. Gatti, B. B. Iversen, *Chem. Eur. J.* **2004**, *10*, 3861.

[83] S. Bhattacharya, R. P. Hermann, V. Keppens, T. M. Tritt, G. J. Snyder, *Phys. Rev. B* **2006**, *74*, 134108(5).

[84] H. J. Kim, E. S. Božin, S. M. Haile, G. J. Snyder, S. J. L. Billinge, *Phys. Rev. B* **2007**, *75*, 134103(4).

[85] P. H. M. Böttger, K. Valset, S. Deledda, T. G. Finstad, *J. Electron. Mater.* **2010**, *29*, 1583.

[86] V. Izard, M. C. Record, J. C. Tedenac, *J. Alloys Compd.* **2002**, *345*, 257.

[87] B. L. Pedersen, B. B. Iversen, *Appl. Phys. Lett.* **2008**, *92*, 161907.

[88] T. Souma, G. Nakamoto, M. Kurisu, *J. Alloys Compd.* **2002**, *340*, 275.

[89] J. H. Ahn, M. W. Oh, B. S. Kim, S. D. Park, B. K. Min, H. W. Lee, Y. J. Shim, *Mater. Res. Bull.* **2011**, *46*, 1490.

[90] H.-J. Gau, J.-L. Yu, C.-C. Wu, Y.-K. Kuo, C.-H. Ho, *J. Alloys Compd.* **2009**, *480*, 73.

[91] X. Y. Qin, M. Liu, L. Pan, H. X. Xin, J. H. Sun, *J. Appl. Phys.* **2011**, *109*, 033714.

[92] J. L. Cui, L. D. Mao, D. Y. Chen, X. Qian, X. L. Liu, W. Yang, *Curr. Appl. Phys.* **2009**, *9*, 713.

[93] A. Denoix, A. Solaiappan, R. M. Ayral, F. Rouessac, J. C. Tedenac, *J. Solid State Chem.* **2010**, *183*, 1090.

[94] S. Schlecht, C. Erk, M. Yosef, *Inorg. Chem.* **2006**, *45*, 1693.

[95] C. S. Birkel, E. Mugnaioli, T. Gorelik, U. Kolb, M. Panthöfer, W. Tremel, *J. Am. Chem. Soc.* **2010**, *132*, 9881.

[96] G. Kieslich, C. S. Birkel, A. Stewart, U. Kolb, W. Tremel, *Inorg. Chem.* **2011**, *50*, 6938.

[97] J. L. Mi, N. Lock, T. Sun, M. Christensen, M. Søndergaard, P. Hald, H. H. Hng, J. Ma, B. B. Iversen, *ACS Nano* **2010**, *4*, 2523.

Chapter 2

Study on Formation Mechanism and Ligand-directed Architectural Control of Nanoparticles Composed of Bi, Sb and Te: towards One-pot Synthesis of Ternary $(Bi,Sb)_2Te_3$ Nanobuilding Blocks

This chapter reports a study on the formation mechanism of nanoparticles (NPs) composed of bismuth, antimony and tellurium for thermoelectric materials using a modified polyol synthetic route. This one-pot synthesis technique has proven highly versatile in creating a wide range of different anisotropic NPs such as nanowires (NWs), nanodiscs (NDs), nanoribbons and nanospines (NDs studded on NWs) simply by modifying the capping species or elemental precursor feeding ratio used in the synthesis. However, an independent control of morphology and composition is still hugely challenging and the facile synthesis of $(Bi,Sb)_2Te_3$ solid solution NPs is not a trivial task, reflecting the complex nature of this multicomponent system. To achieve this goal, it is imperative to understand the formation mechanism based on a systematic investigation of mono- and binary elemental NP systems. The study clearly shows the different actions of oleylamine (OAM) and decanethiol (DT) capping ligands in the synthesis reaction. In the case of DT capping system, Te NDs are first formed, and then, Bi and Sb are separately incorporated into the Te ND structure *via* catalytic decomposition of Bi-DT and Sb-DT complexes on the Te ND surfaces. Therefore, the resulting NPs are phase segregated into Te, Bi_2Te_3 and Sb_2Te_3. On the other hand, in the case of the OAM capping system, Te NWs and Bi-Sb solid solution NPs are formed separately, and then, parts of Te NWs are transformed into $(Bi,Sb)_2Te_3$ phase *via* oriented attachment of Bi-Sb NPs and Te NWs. These findings are crucially important towards the one-pot synthesis of uniform $(Bi,Sb)_2Te_3$ nanobuilding blocks with controllable characteristics for highly efficient thermoelectric materials.

2.1. Introduction

With the advent of nanotechnology the field of thermoelectric (TE) materials has been rejuvenated, and what was once thought of as an area of research with insurmountable challenges has now become one of the most promising technologies to extend our current energy sources.[1] TE materials are highly exciting because they exhibit the Seebeck effect which can be used to create devices that harvest excess heat to create electricity, or can be used to make freonless refrigerators, cool microelectronics, *etc.*[1,2] Nanoparticles (NPs) have proven useful in these materials because the small particle (grain) size causes scattering of the heat carrying phonon along the crystal boundaries, effectively allowing the thermal conductivity to be reduced while maintaining the electrical conductivity.[2,3] In addition, it has been demonstrated that the NP shape plays a key role in this effect because the orientation and area of the grain boundaries can be tuned by long range ordering of the NPs, for example superlattices of one-dimensional nanowires (NWs) or two-dimensional nanodiscs (NDs).[4-6] This causes the overall efficiency of the material to be increased, which is expressed by the dimensionless figure of merit, $ZT = \alpha^2\sigma T/\kappa$, where α is the Seebeck coefficient, σ is the electrical conductivity, κ is the thermal conductivity and T is the absolute temperature.[1] With this in mind, several researchers have attempted to create efficient TE materials with nanostructuring. Bi-Te alloy systems are known to have some of the highest *ZT* values at low temperature range (< 600 K).[2] By creating Bi-Te alloy based NPs, the thermoelectric efficiency is predicted to be even higher.[3,7,8]

Currently there is a large amount of attention being devoted to the creation of nanostructured TE materials. Most often, the synthetic approaches to the TE nanomaterials include techniques such as hydrothermal,[9] electrochemical deposition,[10-13] pulsed laser deposition,[14] sputtering,[15] shear extrusion,[16] mechanical alloying,[17] spark plasma sintering,[18] rapid solidification processes,[19] microwave assisted organic surfactant synthesis,[20,21] or sonoelectrochemistry.[22] Despite much attention being given to the creation of the nanostructured TE materials, few techniques have proven successful at the creation of true nanoscale particles with controllable size, shape and composition composed of Bi-Te alloys. In response to the challenges encountered in these preparation techniques, a few researchers have begun to explore wet chemical based synthesis techniques towards binary Bi-Te alloy NPs with controllable properties in terms of size, shape, composition, *etc.* For example, the synthesis of well-defined Bi_2Te_3-Te heterogeneous nanostructures by controlling the kinetic reaction of Bi^{3+} and TeO_3^{2-} in the presence of hydrazine,[23] the inorganic surfactant assisted

solvothermal synthesis of Bi_2Te_3 nanoplates,[24] the ligand-directed synthesis of Bi_2Te_3 nanorods or nanosheets,[25] or the hot injection synthesis of Bi_2Te_3 nanoplatelets in the presence of oleic acid[26] have been previously reported. Moreover, the synthesis of Bi_2Te_3 NPs through a microemulsion synthetic route,[27] two-step synthesis of Bi_2Te_3 NPs from Bi seeds in the presence of oleylamine,[28] hydrothermal synthesis of Bi_2Te_3 NWs through the solid state interdiffusion of Bi and Te,[29] surfactant directed synthesis of Bi_2Te_3/Bi_2S_3 core–shell nanorod,[30] and two-step synthesis of well-defined Bi_2Te_3 nanotubes based on solution phase nanoscale Kirkendall effect[31] have illustrated the feasibility of using chemically synthesized NPs to create materials with enhanced TE properties because of the highly controllable characteristics of the NPs.

The $(Bi,Sb)_2Te_3$ ternary solid solution system is known as a p-type TE material and has a higher *ZT* value when compared with the Bi_2Te_3 binary alloy.[32,33] This is mainly because $(Bi,Sb)_2Te_3$ exhibits significantly reduced lattice thermal conductivity due to increased unit cell size, low crystal symmetry, and site occupancy disorder. As stated above, chemical synthesis strategies for binary Bi_2Te_3 NPs have been somewhat successful, even though the formation mechanisms of those NPs have not been completely clarified yet. Meanwhile, however, there have been very few successful reports on the direct chemical synthesis of $(Bi,Sb)_2Te_3$ ternary solid solution NPs. For example, Talapin and co-workers have reported the formation of a $Bi_{2-x}Sb_xTe_3$ nanostructured thin film by annealing Bi_2S_3 nanorods functionalized with Sb_2Te_3 metal chalcogenide complex.[3] Zhao and co-workers synthesized nanocrystalline Bi-Sb-Te bulk solids by a combination of hydrothermal synthesis and hot pressing.[9] Ren and co-workers created irregular-shaped $(Bi,Sb)_2Te_3$ bulk solids in an aqueous-phase reduction process.[34] All of these synthetic approaches did not lead to isolated $(Bi,Sb)_2Te_3$ ternary solid solution NPs. Exceptionally, Burda and co-workers successfully synthesized isolated $Bi_{0.5}Sb_{1.5}Te_3$ angular shaped NPs by direct chemical solution synthesis. They first heated bismuth acetate [$Bi(OAc)_3$] and antimony acetate [$Sb(OAc)_3$] dissolved in phenylether in the presence of dodecanethiol (DDT) for 1 h followed by injection of Te dissolved in trioctylphosphine (TOP), followed by reaction for 30 min to form $Bi_{0.5}Sb_{1.5}Te_3$ NPs.[35] Weller and co-workers also reported the successful synthesis of isolated $Bi_xSb_{2-x}Te_3$ nanoplatelets[36] which was similar to the synthetic route of Burda and co-workers.[35] They first heated $Bi(OAc)_3$ and $Sb(OAc)_3$ dissolved in DDT for 45 min followed by injection of oleylamine and Te dissolved in TOP to form $Bi_xSb_{2-x}Te_3$ nanoplatelets.

The above mentioned synthetic techniques typically required multiple steps with the preparation of elemental precursors and lead to only one specific type of NP in terms of shape or structure, making these approaches very limited in the range of NPs they can produce. The polyol synthetic technique is one that has proven very versatile for synthesizing NPs with controllable size, shape, composition, and structure, and in our own research we have demonstrated that in a one-pot synthesis, this general approach can lead to a wide variety of Bi, Sb and Te based NPs with tunable shape and composition simply by changing the nature of the capping species used in the synthesis.[37] Because of the importance in synthesizing $(Bi,Sb)_2Te_3$ ternary solid solution NPs with controllable characteristics we present here a study on the formation mechanism of these promising nanoscale materials. The complexity associated with the formation mechanism of NPs is remarkably increased with the presence of more than one elemental precursor and capping ligand. Even in the single elemental system, the growth mechanism was reported to be not simply based on the function of surfactant as a soft template for NP growth.[38] Expanding to the double elemental NPs, not only the effect of surfactant but many other factors such as the relative reaction rate or the interaction of the two elemental precursors should be taken into account for the increased difficulties in elucidating the NP formation pathway.[39-42] Therefore, in a ternary system, there are many more challenges in addressing the formation mechanism without understanding the fundamental formation of mono- and bi-elemental NPs. Our synthesized NPs consist of Bi, Sb and Te, which are in general considered to be a poor metal (Bi) or a semi-metal (Sb and Te) but hereafter are referred to as "metals". Hence, a systematic study of mono-, bi- and trimetallic NP synthesis is strongly required to investigate the formation mechanism in this complex system. Our results detail the effect of capping ligands, precursors and the metal–ligand cross interaction on NP morphology and composition and elucidate the different formation mechanisms that occur with different capping species. The formation and synthesis of a ternary BiSbTe NW alloy in oleylamine and binary BiTe/SbTe NDs in decanethiol will be discussed.

2.2. Experimental section

2.2.1. Chemicals

Bismuth trichloride ($BiCl_3$, purity 99%), antimony trichloride ($SbCl_3$, purity 99%), tellurium tetrachloride ($TeCl_4$, purity 99%), oleic acid (OAC, purity 90%), oleylamine (OAM, purity 70%), 1,2-hexadecanediol (HDD, purity 90%), 1-decanethiol (DT, purity 96%), 1-dodecanethiol (DDT, purity 98%) and dioctylether (purity 99%) were purchased from Sigma

Aldrich Corp. as well as other common solvents. All reagents were used without further purification .

2.2.2. Synthesis of NPs

1.67×10^{-4} moles each of $BiCl_3$, $SbCl_3$ and $TeCl_4$ precursors were used in the monometallic synthesis. For each bimetallic and trimetallic synthesis, a total 5×10^{-4} moles of elemental precursor was used with equimolar feeding ratio. Elemental precursors were mixed with 25 mL of dioctylether, and 1.5×10^{-3} moles of HDD was added along with the capping species, the identity of which was used to manipulate the morphology and composition of the resulting NPs. In this work, OAM, OAC/OAM and DT were used as capping agents with varying ratios and amounts. The exact amount of capping species used in each synthesis is described more fully in the text. Next, the mixture was purged with argon under vigorous stirring. At this point the reaction temperature was raised to 105 °C for 10 min to remove water, which also caused the reactants to completely dissolve in the solvent (a light grey color in the solution). After this, the temperature was increased to 200 °C and was held for 1 h. The formation of particles within this time was evidenced by the solution color change from light grey to dark grey or black depending on the capping species used. After reaction, the NP solution was cooled to room temperature and the particles were purified by precipitation in ethanol. The materials could be briefly resuspended in hexane with additional OAC, OAM and/or DT. The resulting NPs were then analyzed.

2.2.3. Instrumentation and analysis conditions

An array of instrumental techniques including X-ray diffraction (XRD), transmission electron microscopy (TEM), energy dispersive spectroscopy (EDS), inductively couple plasma mass spectroscopy (ICP-MS), electrospray ionization Fourier transform ionization cyclotron resonance mass spectroscopy (ESI-FTICR-MS), and thermogravimetry (TG) were used to characterize the size, shape, composition, structure and other properties of the materials. XRD patterns were collected in reflection geometry using a Rigaku RINT2500 X-ray Diffractometor at room temperature with Cu Kα radiation (wavelength 1.542 Å). TEM analysis was performed on Hitachi H-7100 and H-7650 transmission electron microscopes operated at 100 kV. TEM samples were prepared by dropping the suspended particles onto a carbon coated copper grid and drying in air overnight. Samples for ICP-MS were prepared by dissolving in aqua regia then were diluted using nitric acid solution (2–5%). The data were collected using a Hitachi

Plasma Mass Spectrometer P-5000 with guide voltages of 30, 35, and 50 V for Sb, Te, and Bi isotopes, respectively. A Fourier transform ion cyclotron resonance mass spectrometer equipped with a 9.4 T superconducting magnet (SolariX, Bruker Daltonics) was used to analyze the metal–ligand complex solution. TG analysis was performed using a Seiko TG /DTA6200. Samples underwent heat treatment from 25 to 600 °C in flowing nitrogen gas with a heating rate of 10 °C per minute.

2.3. Results and discussion

In the previous work,[37] we successfully synthesized NPs composed of Bi, Sb and Te using different capping systems and the complexity that arose in the ternary alloy system inspired us to conduct a more systematic study to investigate the formation mechanism for controlling the morphology and composition of the final NPs. In this study, three capping systems consisting of OAM, OAC/OAM and DT were used to synthesize mono-, bi- and trimetallic NPs. We studied the effect of individual interactions between capping ligands and metal precursors on NP morphology and composition from the results of the primary synthesis using only one metal precursor with each capping system. Then the combination of two metal precursors was studied to clarify the role that each metal plays in the synthesis, along with effect of capping ligands in the reaction/incorporation of the two metals into the final NPs. These results together with the characterization of trimetallic NPs synthesized using each capping system help to clarify the formation mechanism of trimetallic NPs in these complex systems. As a result of the wide range of syntheses conducted with varying reaction conditions, not all of the synthesized materials have an ideal size, structure or composition. Many of the results related in this work show the formation of micro-sized particles, non-homogeneous structure/composition, or oxidized materials, *etc.*, however these results still shed light on the underlying formation mechanism of NPs in this system. Additionally, it is also important to note that the three different capping ligands used in this study were not further purified before use, so a significant portion of these ligands (especially OAM) may include short alkane chain impurities. It is well known that trioctylphosphine oxide (TOPO) ligands contain impurities such as phosphonates and phosphonic acid , and these impurities may very well bind far more strongly to cation sites than TOPO. The ligands used in this study may also contain impurities which have different functional groups. While these impurities may influence the particle size or shape formation, this study primarily focuses on the chemical nature of the reactive terminus of the primary component of the ligands (*i.e.* amine, carboxylate and thiol), which is the

primary factor leading to the various particle size, morphology, structure and compositions observed.

2.3.1. Study of monometallic synthesis approach

Bi, Sb and Te monometallic NPs were synthesized using a single metal precursor with the various capping systems. The morphology and crystal structure of the resulting NPs were characterized by TEM and XRD analyses. The results are briefly summarized in Table 2.1.

Table 2.1 Main products synthesized using a single metal precursor[a]

	Organic Capping Ligands		
Metal Precursors	**OAM**	**OAC/OAM**	**DT**
$BiCl_3$	BiOCl aggregates	BiOCl aggregates	Bi plates D ~ 500 nm L > 2 μm
$SbCl_3$	Sb NWs D ~ 100 nm L ~ 2−10 μm	Sb NWs D ~ 100 nm L ~ 2−10 μm	No solid product
$TeCl_4$	Te NWs D ~ 200 nm L ~ 5−10 μm	Te NWs D ~ 100 nm L ~ 2−6 μm	Te nanoplates D ~ 100 nm

[a] D and L represent mean diameter and length estimated from TEM images, respectively

Synthesis of Bi NPs

Fig. 2.1 shows the XRD patterns (A–C) and TEM images (D and E) of materials synthesized using a $BiCl_3$ precursor. When OAM or OAC/OAM is used as a capping system, bismuth oxychloride (BiOCl) was mainly formed with elemental Bi in a rhombohedral phase as a minor product as seen in Fig. 2.1A and B (for detail see Appendix II, Table A2.1 and A2.2). The BiOCl NPs are insoluble in any kind of solvent used in this study. The peak broadening in the XRD pattern indicates that the mean crystalline sizes of BiOCl and Bi are relatively small. Fig. 2.1D shows a TEM image of the sample synthesized using OAM. Large aggregates composed of matrix having an indeterminate form and small NPs with spherical shape with a diameter of about 20 nm are observed. Similar TEM images were also observed for the case of using OAC/OAM (not shown). As a consequence, we attribute the small

spherical NPs and the matrix in Fig. 2.1D to Bi NPs and BiOCl crystals, respectively. It is well known that $BiCl_3$ reacts with water to give a white precipitate of BiOCl. The source of oxygen in the present syntheses may be from residual water and/or oxygen molecules dissolved in the solvent (dioctylether) which could not be completely removed, even under argon purging and elevated temperature. In addition, it has also been reported that BiOCl was formed in the synthesis of Bi_2S_3 with $BiCl_3$ and sulfur precursors using OAM as solvent and capping ligands even under a water-free environment[43] which is similar to our observation.

Changing to the DT capping system, only an elemental Bi phase (see Appendix II, Table A2.3 for detail XRD peak assignment) was observed with some minor unidentifiable peaks (unlabeled) in the XRD pattern as shown in Fig. 2.1C. These minor peaks could arise as a result of some leftover bismuth precursor-ligand complex which could not be removed during the particle purification process. A mixture of elongated plate-like particles (~500 nm in diameter and several microns in length) and smaller polyhedral shaped particles (~500 nm) are shown in Fig. 2.1E. These results suggest that DT makes stable complexes with the Bi cation and protect it from creating BiOCl while OAC and OAM ligands do not.

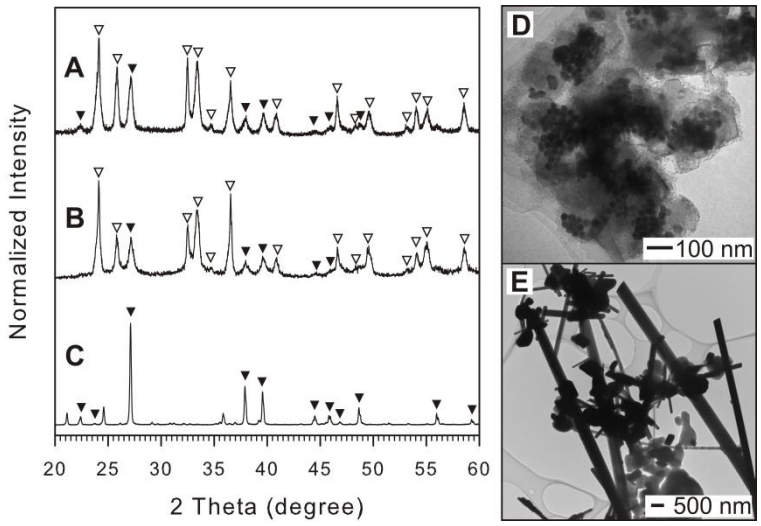

Figure 2.1. XRD patterns and TEM images of materials synthesized using $BiCl_3$ and OAM (A and D), OAC/OAM (B), and DT (C and E). The indexed peaks are marked by the symbols open triangle (▽) for BiOCl (JCPDS card no. 006-0242) and filled triangle (▼) for Bi (JCPDS card no. 044-1246).

Synthesis of Sb NPs

Similarly, syntheses with $SbCl_3$ and capping ligands OAM, OAC/OAM and DT were performed. Fig. 2.2 shows the XRD patterns (A and B) and TEM images (C and D) of the synthesized NPs. When OAM or OAC/OAM is used as a capping system, the XRD patterns collected for the samples are well defined for elemental Sb with a rhombohedral structure without by-product such as antimony oxychloride (SbOCl) as shown in Fig. 2.2A and B (for detailed peak positions and assignment see Appendix II, Table A2.4 and A2.5). Using OAM or OAC/OAM leads to the formation of NWs which have a diameter of about 100 nm and length of several microns (Fig. 2.2C, D, and Appendix II, Fig. A2.1 and A2.2). However, using DT as a capping system, Sb was not successfully reduced under the reaction conditions as evidenced by the fact that the reaction solution did not change color during one hour of heating at 200 °C and no solid materials could be obtained. This phenomenon can be explained due to the stable complex that Sb forms with DT which is not easily decomposed, preventing the subsequent reduction and formation of Sb NPs. To further probe the observation, the Sb-DT synthesis was also conducted at 240 °C, which resulted in a brown suspension that quickly returned to a clear color upon cooling of the reaction. When the synthesis was repeated using dodecanethiol (DDT) at 250 °C, an identical phenomenon was observed. The results indicate that Sb NPs could not be synthesized in the presence of DT or DDT, even at elevated temperature, perhaps because of an etching effect of Sb metal by thiol containing ligands.

In a separate experiment, $SbCl_3$ could be dissolved in DT and hexane solvent at room temperature (Appendix II, Fig. A2.3) and ESI-FTICR-MS was used to detect high molecular weight fragments containing Sb isotopes coupled with an organic component which arises from the Sb-DT complex (Appendix II, Fig. A2.4). Moreover, thermal analysis for the Sb-DT complex shows a slow mass loss taking place before 220 °C (Appendix II, Fig. A2.5), which explains the stability of the Sb-DT complex under the reaction conditions. The study of monometallic Sb synthesis suggests that different capping ligands created a complex with Sb with different stability in which DT makes a more stable complex that did not undergo the reduction to Sb NPs while OAM or OAC/OAM creates a weaker complex that can be reduced to form elemental Sb NWs.

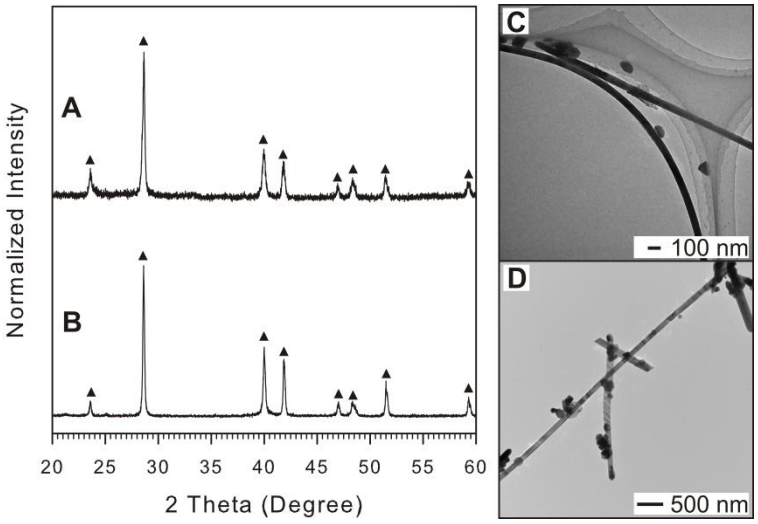

Figure 2.2. XRD patterns and TEM images of Sb NWs synthesized using OAM (A and C) and OAC/OAM (B and D). In the case of using DT, no solid particles can be obtained. The upright filled triangles (▲) indicate peaks assigned to Sb with rhombohedral structure (JCPDS card no. 01-085-1322) in the XRD pattern (A and B).

Synthesis of Te NPs

Fig. 2.3 shows the XRD patterns (A–C) and TEM images (D–F) of NPs synthesized using a $TeCl_4$ precursor. The composition and structure of all the resulting NPs determined based on the indexed peaks show that all samples are composed of elemental Te with a hexagonal phase (Fig. 2.3A–C). For detailed XRD peak assignment, see Appendix II, Table A2.6-A2.8.

The formation of elemental Te in all cases may occur because of the relatively high reduction potential of Te^{4+}, $E^{\circ}_{red}(Te^{4+}/Te)$ = 0.529V, which enhances the ability of Te to be reduced under the synthetic conditions. In addition, $E^{\circ}_{red}(Te^{4+}/Te)$ is significantly higher than those of Bi^{3+} [$E^{\circ}_{red}(Bi^{3+}/Bi)$ = 0.16V] and Sb^{3+} [$E^{\circ}_{red}(Sb^{3+}/Sb)$ = 0.212V].[34] This supports the favorable tendency of elemental Te particles to be formed under the various reaction conditions while Bi and Sb exhibit many cases where particles were not formed. The elemental Te NPs with various morphologies illustrate the effect of capping ligand identity. The use of the OAM or OAC/OAM capping system led to the formation of very long wires which appear to grow from a central nucleation point in different directions (Fig. 2.3D, E, and Appendix II, Fig. A2.1 and A2.2). This phenomenon is especially apparent when using OAC/OAM as a capping species, in Fig. 2.3E a NW cluster can be observed with a central nucleation point and tapered wires protruding out from the center of the cluster .

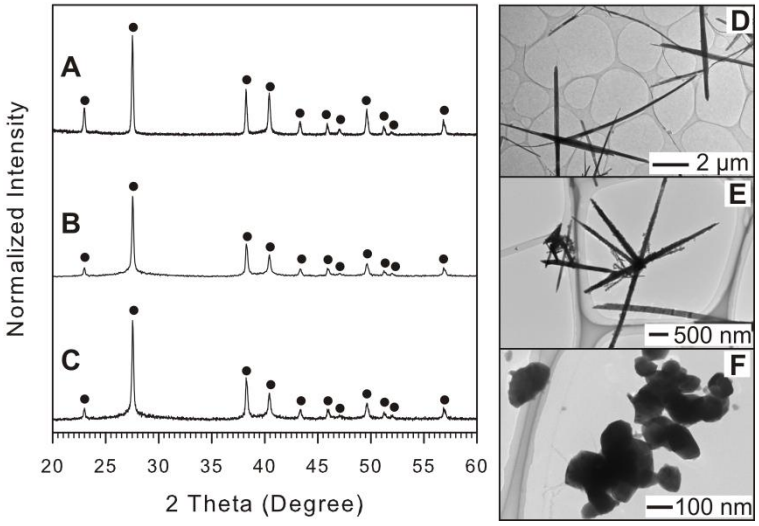

Figure 2.3. XRD pattern and TEM images of resulting Te NPs synthesized using OAM (A and D), OAC/OAM (B and E), and DT (C and F). The XRD peaks are labeled by filled circle (●) for hexagonal structured Te (JCPDS card no. 036-1452).

Changing the capping ligand to DT resulted in roughly spherical particles with a diameter of about 100 nm (Fig. 2.3F). However, the mean crystalline size of Te NPs was estimated to be around 41 nm from the full width at half-maximum of the (101) primary peak by the Scherrer formula, which is smaller than the size estimated from TEM images (*ca.* > 100 nm) suggesting that the NPs have a platelet morphology. For detailed XRD peak assignment, see Appendix II, Table A2.8.

2.3.2. Study of bimetallic synthesis approach

To further study the general synthetic system, the analysis was expanded to include binary metallic precursors in the synthesis under otherwise identical conditions to the monometallic cases. The resulting variation in particle formation in terms of composition, morphology and structure reveals the complex nature of this system. The understanding of the interdependence of each metal precursor along with the organic capping ligands is important for controlling the properties of the resulting NPs. Each combination of two elemental precursors was used with different capping ligand systems including OAM, OAC/OAM or DT to study the effect on the final particle characteristics. The general results for these syntheses are summarized in Table 2.2.

Table 2.2 Main products synthesized using two different kinds of metal precursors[a]

Metal precursors	Organic Capping Ligands		
	OAM	**OAC/OAM**	**DT**
$BiCl_3$, $SbCl_3$	BiSb nanoplates *D* ~ 20−60 nm	BiSb NPs *D* ~ 20−40 nm	Bi plates *D* ~ 100−300 nm *L* ~ 10 μm
$BiCl_3$, $TeCl_4$	Te NWs *D* ~ 30−200 nm *L* ~ 3−10 μm	Te NWs *D* ~ 100−200 nm *L* ~ 3−10 μm	Bi-Te NDs *D* ~ 30−50 nm *H* ~ 5−10 nm
$SbCl_3$, $TeCl_4$	Te NWs *D* ~ 30−100 nm *L* ~ 3−10 μm	Te NWs *D* ~ 50−200 nm *L* ~ 3−10 μm	Sb-Te plates

[a]The composition assessment is based on EDS except for the case of NPs synthesized using Sb and Te precursors. D, L and H represent mean diameter, length and/or thickness estimated from TEM images, respectively.

Synthesis of Bi-Sb NPs

Bi-Sb materials were first synthesized using OAM, OAC/OAM and DT as capping systems. Fig. 2.4 shows the XRD patterns and the corresponding TEM images collected for the three resulting materials with OAM (A, D, and G), OAC/OAM (B and E) and DT (C and F) capping system. When OAM is used, the particles appear roughly spherical (some particles are observed with hexagonal (Fig. 2.4G) or pentagonal shape) with an approximate size of ~20–60 nm. However, in some places where particles overlap each other (the inset of Fig. 2.4D), it is found that the overlapping areas were darker than the other areas which suggests NPs with a disc or platelet morphology. Additionally, the peaks in the XRD pattern for this sample (Fig. 2.4A) seem uncharacteristically broad (*i.e.* reflective of a smaller grain size), in light of these observations it may be that very thin platelets have formed in this synthesis approach. Weller and co-workers made a similar claim when they analyzed their $Bi_xSb_{2-x}Te_3$ nanoplatelets.[36] When OAC/OAM was used as a capping species, spherical and egg shaped NPs with a diameter around ~20–40 nm were obtained (Fig. 2.4E) with a morphology similar to Bi NPs formed in the monometallic synthesis using $BiCl_3$ and OAM or OAC/OAM (Fig. 2.1D). The broadened peaks appearing in the XRD pattern (Fig. 2.4B) arise as a result of the nanoscale size of the particles. The mean crystalline size of the NPs was calculated to be 19 nm from the full width at half-maximum of the (012) primary peak by the Scherrer formula, which is comparable with the size estimated from Fig. 2.4E as shown in Table 2.3 suggesting that the crystallinity of the

NPs is quite good. For detailed XRD peak assignment, see the Appendix II Table A2.9 and A2.10.

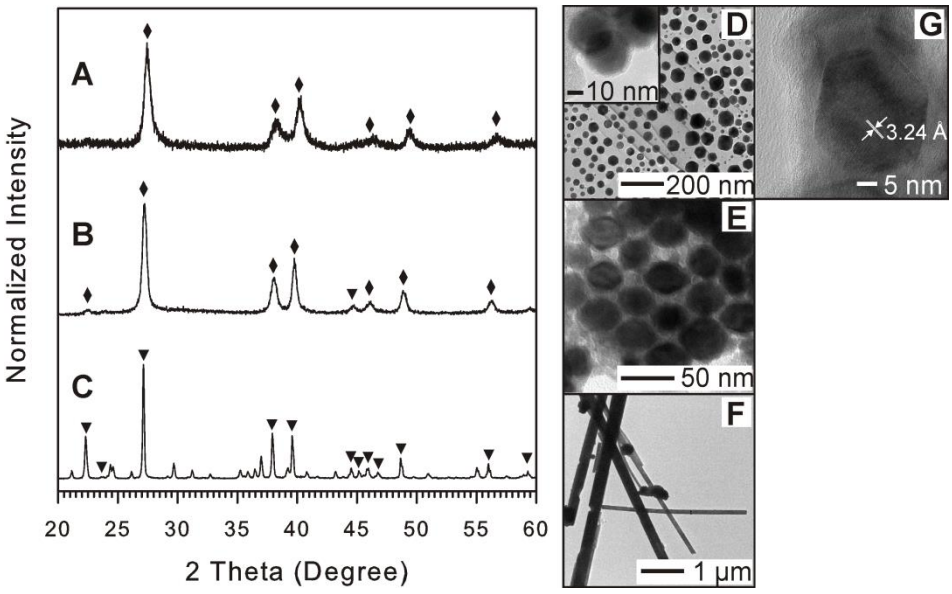

Figure 2.4. XRD patterns and TEM images for Bi-Sb NPs synthesized using OAM (A and D), OAC/OAM (B and E), and DT (C and F). G is the HR-TEM image of Bi-Sb NPs synthesized using OAM. The identities of XRD peaks were labelled by filled diamond (♦) for Bi-Sb alloy (JCPDS card no. 00-035-0517) and filled triangle (▼) for Bi (JCPDS card no. 044-1246). For detail see Appendix II, Table A2.9–11.

By analyzing the XRD peak positions in detail, all peaks are found to be in between the reference positions of pure Bi and Sb peaks for both samples. The lattice spacing measured from HR-TEM (Fig. 2.4 G) for single Bi-Sb NP also shows a value of 3.24 Å (corresponding to (012) crystal plane) which is consistent with the average d-spacing calculated from main peak in XRD pattern (Bragg's law) and in between those values of pure Bi and Sb. In addition, EDS analyses for the particles shown in Fig. 2.4D and E confirmed that the compositions of NPs are $Bi_{70}Sb_{30}$ and $Bi_{95}Sb_5$, respectively. Both Bi and Sb have a face-centered rhombohedral crystal structure, and they have complete solid solubility with each other.[44] Early X-ray studies showed that the lattice parameter changes linearly with Sb concentration.[45] Hence, Vegard's law can be applied directly to the Bi-Sb alloy system. The mathematical expression of Vegard's law is given by:

$$d_{BiSb} = xd_{Bi} + (100\text{-}x)d_{Sb} \qquad (2.1)$$

where d_{Bi}, d_{Sb} and d_{BiSb} denote the lattice spacings of Bi, Sb and Bi_xSb_{100-x}, respectively, and x is the molar percent of Bi in the alloy. When the (012) lattice spacing (primary peaks in Fig. 2.4D and E) is plotted as a function of x, a clear linear relationship was obtained (Fig. 2.5). As a result, it is concluded that both NPs synthesized using OAM and OAC/OAM as capping systems are Bi-Sb alloys with compositions of $Bi_{70}Sb_{30}$ and $Bi_{95}Sb_5$ respectively.

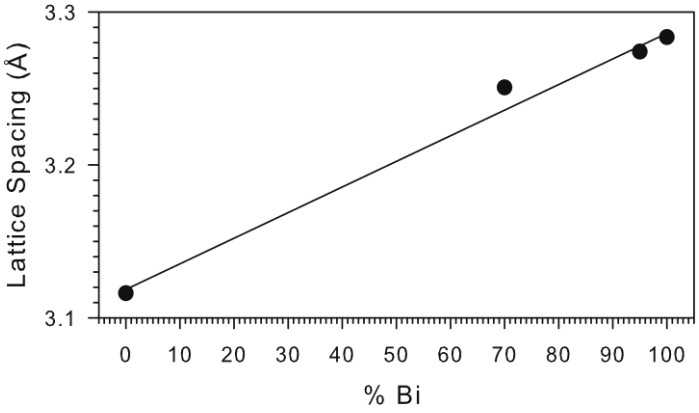

Figure 2.5. Relationship between the lattice spacing of (012) crystal plane and molar composition of BiSb alloy synthesized using OAM ($Bi_{70}Sb_{30}$) and OAC/OAM ($Bi_{95}Sb_5$). The lattice distance of crystal plane (012) of pure Bi, Sb and BiSb alloy were calculated based on XRD peak positions of (012) crystal plane collected for the corresponding synthesized NPs.

Changing the capping ligand to DT, particles with elongated plate-like shape occur with a length of ~10 μm and diameter of *ca.* ~100–300 nm, along with some smaller spherical shaped NPs as shown in Fig. 2.4.F. The XRD pattern reveals the formation of elemental Bi with some minor unidentifiable peaks as shown in Fig. 2.4C, which are characteristically the same pattern as those observed in Fig. 2.1C for monometallic Bi synthesized using DT (for detailed comparison see Fig. A2.6, Appendix II). Therefore, these unidentifiable peaks could arise as a result of some by-product of bismuth and organic ligand that could not be removed in the particle purification process. One important observation is that there is no bismuth oxide or BiOCl peaks observed in the XRD pattern, which is consistent with the case of Bi monometallic synthesis using DT. The composition assessment using EDS shows only Bi without Sb in the final products. These results show the consistence with the monometallic study for Bi and Sb with DT where Bi elongated plates grew and Sb-DT could not be reduced to form Sb NPs. This also suggests that once Bi is formed, it does not seem to catalyze the decomposition or reduction of the stable Sb-DT complex under the reaction conditions used here.

Table 2.3 Mean crystalline size calculated for NPs based on XRD pattern and Scherrer's formula[a]

Metal Precursors	Capping systems	Main product	2 Theta (deg)	D_{XRD} (nm)	D_{TEM} (nm)
$TeCl_4$	DT	Te nanoplates	27.54	40.9	~100
$BiCl_3$, $SbCl_3$	OAM	BiSb nanoplates	27.45	14.6	39±14
$BiCl_3$, $SbCl_3$	OAC/OAM	BiSb NPs	27.28	19.0	32±4
$BiCl_3$, $TeCl_4$	DT	BiTe NDs	27.62	43.1	~30–50
$SbCl_3$, $TeCl_4$	DT	SbTe plates	28.20	45.5	N/A

[a] D_{XRD} and D_{TEM} represent mean crystalline size and NP size estimated from XRD patterns and TEM images, respectively.

Synthesis of Bi-Te NPs

Fig. 2.6 shows the XRD patterns (A–C) and TEM images (D–F) of NPs synthesized using $BiCl_3$ and $TeCl_4$ binary precursors. Fig. 2.6D shows the TEM image of NPs synthesized using OAM capping system. As can be seen in Fig. 2.6D, NWs with a smooth surface and a relatively narrow diameter (~30–200 nm) with a length of several microns are obtained. Fig. 2.6E shows that using the OAC/OAM capping system leads to the formation of wire or bar shaped materials with a length of several microns and diameter of about ~100–200 nm. These wire shaped materials are mainly composed of elemental Te based on XRD analysis (Fig. 2.6A and B) and TEM-EDS measurement. The disappearance of Bi in the final materials indicates that the alloying of Bi and Te did not occur and Te NWs did not promote the reduction of Bi complex to Bi under these synthetic conditions using OAM or OAC/OAM capping ligands. Moreover, BiOCl was not observed in the resulting synthesized material even though it was observed in the monometallic synthesis using OAM (Fig. 2.1A) or OAC/OAM (Fig. 2.1B). This may be due to the formation of a Te complex and preferential adsorption of the capping species on the Te NP surface (resulting in enhanced protection for Te NWs during growth, effectively occupying a majority of the capping species). Therefore, BiOCl was not observed as a byproduct of the synthesis, or it may have been removed as a result of the washing process of the Te NPs after the synthesis.

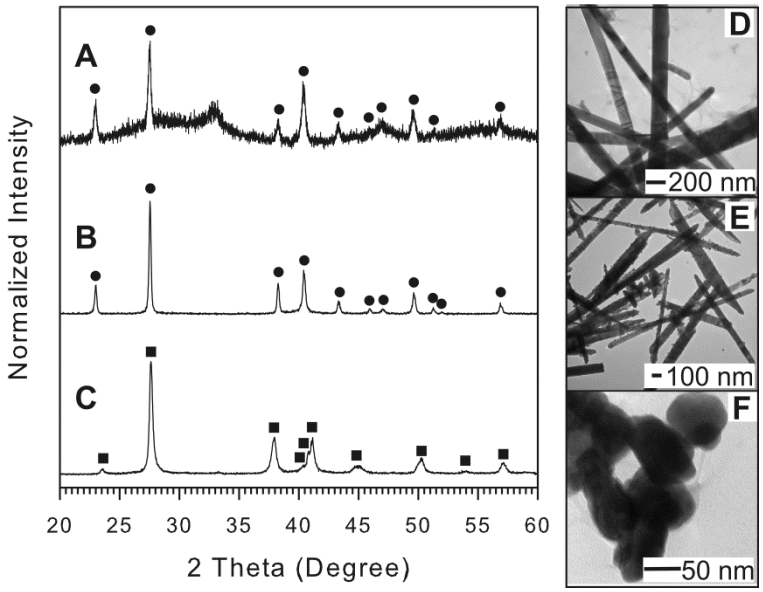

Figure 2.6. XRD patterns and TEM images for Bi-Te materials synthesized using OAM (A and D), OAC/OAM (B and E), and DT (C and F). Filled circles (●) and filled squares (■) indicate peaks assigned for hexagonal-phase Te (JCPDS card no. 036-1452) and for rhombohedral Bi_2Te_3 (JCPDS card no. 015-0863), respectively. For detail see Appendix II, Table A2.12–14.

TEM and XRD results for bimetallic NPs synthesized using DT capping species are given in Fig. 2.6C and F. From the TEM images (Fig. 6F) captured for this sample, the NPs appear to be highly aggregated and have a disc-like morphology. The NPs are not uniform in size, but seem to be very thin as several particles can be observed that overlap each other. Some additional TEM images (Appendix II, Fig. A2.7) collected for the resulting NPs show the varying image contrast caused by the different alignment of NDs to the electron beam where very light, roughly spherical NPs correspond to the top-down alignment and very dark rod like NPs offer a side view of the discs. The NDs have a diameter of about ~30–50 nm and thickness of about ~5–10 nm. The broad peaks in the XRD pattern (Fig. 2.6C) collected for these NPs may arise as a result of the nanoscale size and thin platelet morphology. Analysis of the composition based on assigning XRD peaks shows the presence of the Bi_2Te_3 phase which is consistent with the fact that both Bi and Te particles were formed in the monometallic approach using DT.

The higher standard reduction potential of Te(IV) likely leads to an initial reduction and nucleation of Te followed by the reduction of Bi complex to form Bi_2Te_3. The Te particle surface in this case catalyzed the decomposition of the Bi complex followed by the alternate adsorption/reduction reaction of Bi and Te, resulting in the Bi_2Te_3 phase and ND morphology instead of Bi elongated plates as found for Bi synthesized with DT (Fig. 2.1E). The formation of Bi_2Te_3 NDs capped with DT arises primarily as a result of the catalytic effect of Te at the particle surface in the decomposition of the Bi-DT complex which introduces an intriguing pathway to modify the final NP morphology and composition.

Synthesis of Sb-Te NPs

Fig. 2.7 shows the XRD patterns (A–C) and TEM images (D–F) of NPs synthesized using $SbCl_3$ and $TeCl_4$ binary precursors. It was found that the synthesis using $SbCl_3$ and $TeCl_4$ with OAM or OAC/OAM capping systems resulted in the formation of NWs (Fig. 2.7D and E) with a length of several microns and diameter of about ~30–200 nm. The XRD peak assignment (Fig. 2.7A and B) for these materials indicates the formation of only elemental Te without any sign of Sb or other compounds which is in agreement with the EDS analysis . It seems that Sb was not reduced or incorporated into the Te NWs even though both Sb and Te NWs can be created using these two capping systems in monometallic syntheses. From the study of Sb-DT complex, the complex fragments are noted to have very high molecular weight (Appendix II, Fig. A2.4) which may reflect the fact that several capping ligand species are required to form the complex. Therefore, in bimetallic synthesis when the amount of capping ligands used in the synthesis is double the normal amount, there still may not be a sufficient amount to make a stable complex with all metal precursors. The lack of Sb in the resulting NWs can be explained due to the fact that most capping species were used to make the complex with Te and were adsorbed on the Te NW surface rather than making a complex with $SbCl_3$. As a result, $SbCl_3$ or even Sb oxide and other compounds, such as SbOCl, would likely be removed in the particle washing process.

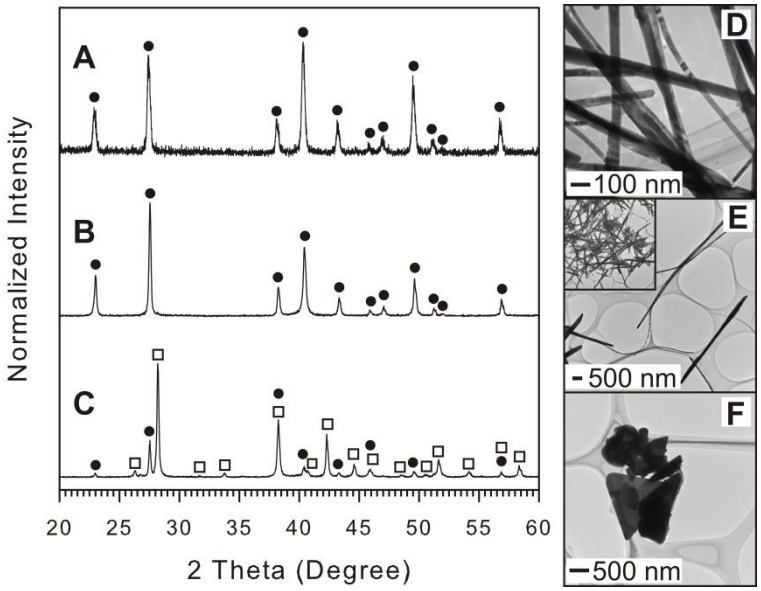

Figure 2.7. XRD patterns and TEM images for Sb-Te materials synthesized using OAM (A and D), OAC/OAM (B and E), and DT (C and F). The peak identities were labelled by the symbol filled circle (●) for Te (JCPDS card no. 036-1452) and open square (□) for Sb_2Te_3 (JCPDS card no. 015-0874). The inset of Fig. 2.7E represents a zoomed out view of synthesized NWs. For details see Appendix II Table A2.15–17.

Using DT as a capping system, on the other hand, leads to the formation of large platelet -like particles (Fig. 2.7F) composed of Sb_2Te_3 with a minor amount of elemental Te as indexed in the XRD pattern (Fig. 2.7C). The formation of two segregated phases including Sb_2Te_3 and Te indicates that the existence of Te NPs catalyzed the decomposition and reduction of the Sb-DT complex, which failed to be reduced in the Sb monometallic synthesis with DT (see Table 2.1).

2.3.3. Summary of the mono- and bi-metallic synthesis studies

From the study of mono- and bi-metallic syntheses, we can elucidate the role that each individual capping ligand plays, as well as the influence of the metallic interaction in the formation of the NPs. The formation of NPs is summarized for two general types of capping systems: one is DT and the other is OAM and OAC/OAM. For the first case, DT creates a relatively strong complex with the three elemental precursors, especially with Sb which could not be reduced in the monometallic synthesis. The resulting small Te nanoplates and long Bi particles without oxides and other compounds in single precursor approach show the good

capping ability of DT. Furthermore, the results of the bimetallic system capped with DT highlighted the important catalytic effect of Te for Bi_2Te_3 and Sb_2Te_3 formation. We also found that NPs composed of Bi and Sb failed to be formed in DT due to the stability of Sb-DT complex along with no catalytic effect of Bi particles. Therefore, the strong bimetallic interaction of Te with Bi and/or Sb-DT complexes and the lack of Bi-Sb alloy formation explain the existence of two segregated phases obtained when using DT with all three elemental precursor synthesis.[37] On the other hand, OAM or OAC/OAM, in the interaction with single precursor, directs the growth of monoelemental Sb and Te NWs as well as the BiOCl formation with a minor phase of Bi. In these capping systems, if Te does not act as catalyst for Bi or Sb complex reduction, then only monometallic Te NWs grow in the bimetallic systems. However, Bi and Sb can be incorporated into a Bi-Sb alloy NP as a result of the formation and catalytic effect of Sb on the Bi complex. Therefore, in OAM or OAC/OAM capping systems, there is a possibility of forming a $(Bi,Sb)_2Te_3$ ternary solid solution when all three elemental precursors are combined together. The general understanding of the NP formation mechanism encourages a study of the synthesis of trimetallic NPs using these capping species, towards $(Bi,Sb)_2Te_3$ ternary solid solution NPs.

2.3.4. Study of trimetallic synthesis approach

In light of the key results obtained from the formation mechanism investigation for monometallic and bimetallic syntheses, we synthesized trimetallic NPs with the OAM capping ligand system. In this section, the OAM capping system was focused on because of the failure to synthesize a Bi-Sb alloy using the DT capping system in the bimetallic synthesis, while only Bi-Te and Sb-Te alloys could be obtained using DT. Based on these results, it is likely that $Te/Bi_2Te_3/Sb_2Te_3$ segregated NPs would be dominantly synthesized if DT was used in a Bi-Sb-Te trimetallic synthesis. In fact, a similar result was previously reported in which phase-segregated NDs were obtained.[37] Therefore, the formation mechanism in this case is relatively simple, *i.e.*, Te NP formation followed by Bi and Sb individual incorporation into the Te NPs due to the catalytic effect of Te without Bi-Sb interaction. Accordingly, it seems quite difficult to synthesize nanostructured $(Bi,Sb)_2Te_3$ solid solution using DT as a capping system. On the contrary, in the case of Bi-Sb bimetallic synthesis using the OAM capping system, we successfully synthesized $Bi_{70}Sb_{30}$ alloy nanoplates, while Bi-Te and Sb-Te alloys could not be obtained using OAM. It is worthwhile to investigate whether a Bi-Sb-Te cross interaction takes place. The main results and discussion of this section, therefore, will detail only trimetallic

NWs synthesized with OAM capping species which give more insight into the growth mechanism of Bi-Sb-Te NPs and how to control the resulting shape, composition and structure.

Using OAM as a capping ligand led to the formation of very long and high aspect ratio NWs. Fig. 2.8 shows the TEM and HR-TEM images of NWs synthesized using 0.17 mL OAM (corresponding to 1 : 1 molar ratio of elemental precursors to OAM). The length of the NWs is several microns with a diameter ranging from 50 to 100 nm, which gives a very high aspect ratio (~50–100). On the surface of the NWs, there are some small NPs and the non-homogeneous local areas (reflected by different contrast) observed in the TEM images for each NW may indicate a heterogeneous composition. In addition, if one takes a close look at Fig. 2.8C, the center of a NW is lighter than the periphery suggesting the composition distribution in a radial direction (*i.e.* Bi-rich at the periphery) or the tube-like structure caused by nanoscale Kirkendall effect[31] which refers to a nonreciprocal mutual diffusion through an interface of two metals. HRTEM images of a single NW (Fig. 2.8D and E) illustrate the high crystallinity of particles, however, the lattice spacings measured by HR-TEM cannot used to distinguish between Te, Bi_2Te_3 and ternary solid solution BiSbTe phase due to the similarity in their crystal structure.

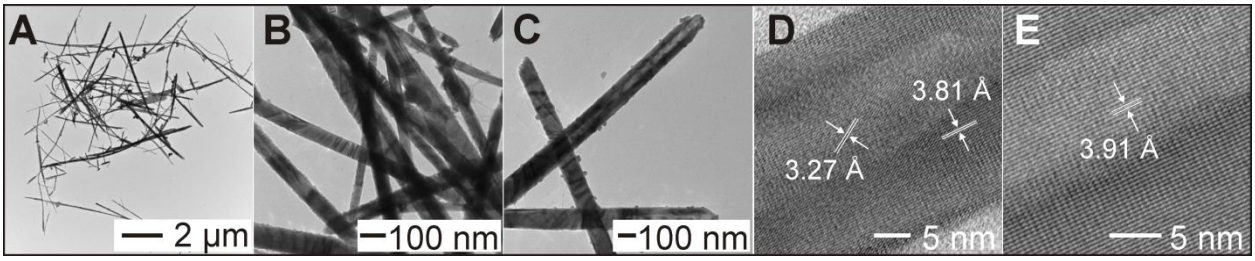

Figure 2.8. TEM (A-C) and HR-TEM (D-E) images of trimetallic NWs synthesized using OAM as capping species with 1:1 molar ratio of precursors and OAM. Image (A) shows the zoomed out view of the synthesized NWs, (B) shows a magnified view of the NWs which have a narrow diameter and are smooth, and (C) shows NWs with some smaller NPs at the surface and the tip of NWs. D and E are the HR-TEM of a single NW.

Fig. 2.9 shows the XRD patterns for NWs capped with OAM. XRD peaks can be indexed for several segregated phases including Te (hexagonal structure), Bi_2Te_3, and $(Bi,Sb)_2Te_3$ (rhombohedral structure) due to their similar crystal structures and overlapping peaks. The reference reflection of bulk $(Bi_{0.5}Sb_{0.5})_2Te_3$ was used to assign the peak position of

$(Bi,Sb)_2Te_3$ phase. Note that Sb_2Te_3, Sb or Sb oxide phases could not be found in the XRD pattern. To assign the phases definitively, the elemental assessment for NWs using ICP-MS analysis was conducted with the result of $Bi_{15}Sb_{26}Te_{59}$, which is in general consistent with each other in the co-existence of all three metal components. Note that the accurate elemental assessment of Bi-Sb-Te ternary material is difficult using EDS because Sb and Te peaks overlap each other significantly. It can be concluded that dominant phases of the NWs synthesized using OAM capping system are $(Bi,Sb)_2Te_3$ (rhombohedral) and elemental Te (hexagonal) by considering the following facts: (1) the NWs have no Sb_2Te_3, Sb or Sb oxide phases, (2) the NWs contain a significant amount of Sb, and (3) the presence of the characteristic peaks of Te at 2θ = 22.98, 38.21, 40.38, 43.28, 49.55, 51.16, and 51.92 degrees and of $(Bi,Sb)_2Te_3$ at 2θ = 70.06°. Note that the existence of the Bi_2Te_3 phase is not ruled out because other peaks of the $(Bi,Sb)_2Te_3$ phase significantly overlap with the Bi_2Te_3 phase. For details XRD peak assignment see Appendix II, Table A2.18.

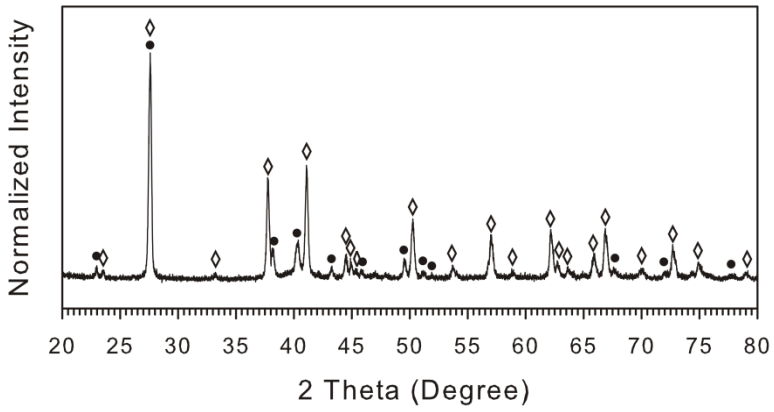

Figure 2.9. XRD patterns of trimetallic NWs synthesized using OAM as capping species with 1:1 molar ratio of precursors and OAM. The peak identities are labeled by the symbol filled circle (●) for Te (JCPDS card no. 036-1452), and open diamond (◊) for $(Bi_{0.5}Sb_{0.5})_2Te_3$ (JCPDS card no. 01-072-1835).

For the reference, the synthesis of BiSbTe NPs using only OAC also conducted, and in this case the phase segregation was clearly observed (see Appendix II, Fig. A2.8-9, Table A2.19).

2.3.5. Summary of the nanoparticle formation mechanism

To consistently explain all the results in the systematic studies about the effect of capping ligands and metal complex interaction on NP morphology and composition, we propose two separate formation mechanisms for BiSbTe containing NPs with two kinds of capping systems: OAM and DT based on the metal–ligand complex formation, decomposition and interaction. In general, due to the high reduction potential, the Te complex was first reduced, undergoing nucleation. However, the growth of Te NPs and the incorporation of other metals strongly depend on the capping ligands (formation of complex with the metal precursors) and the metal–ligand cross-interaction.

In the case for DT, a stable complex with Sb can be formed, with a less stable complex for Bi or Te. As a result, the Sb-DT complex itself could not be reduced under the synthetic conditions, but Bi and Te can be reduced and form elongated plates or nanoplates respectively. Bi was not found to catalyze the reduction of the Sb-DT complex, as indicated in the bimetallic approach which led to the formation of only monometallic Bi plates. On the other hand, Te NDs could act as a catalyst for Bi or Sb complex reduction, resulting in the formation of Bi_2Te_3 and Sb_2Te_3 materials. The existence of these two phases in trimetallic NPs synthesized using DT therefore can be explained based on the catalytic effect of Te and reaction of Te with the other metal complexes.

When OAM is used as a capping system, Te does not exhibit catalytic properties in the reduction of the other metal complexes. Moreover, the formation of Te containing NWs for all synthesis approaches with the presence of Te precursor and OAM indicated that the growth of Te NWs capped with OAM is preferential and the incorporation of other metals into the NWs is not feasible when using OAM. In this capping system, Sb was found to play a dual role in catalyzing the decomposition of the Bi complex, which prevented the formation of BiOCl. It is very important that a Bi-Sb alloy can be formed under similar synthetic conditions with OAM. The formation of these materials illustrates the possibility to form an alloy of BiSbTe when all three metal precursors are used in the synthesis. Therefore, the reduction and growth of Te NWs and Bi-Sb NPs can occur separately in the trimetallic synthesis, and the formation of the final NWs containing $(Bi,Sb)_2Te_3$ ternary solid solution may be caused by the oriented attachment[42] of Te NWs and Bi-Sb NPs which was not observed in the case of using DT as capping ligand. The formation mechanism in these two cases is illustrated in Fig. 2.10.

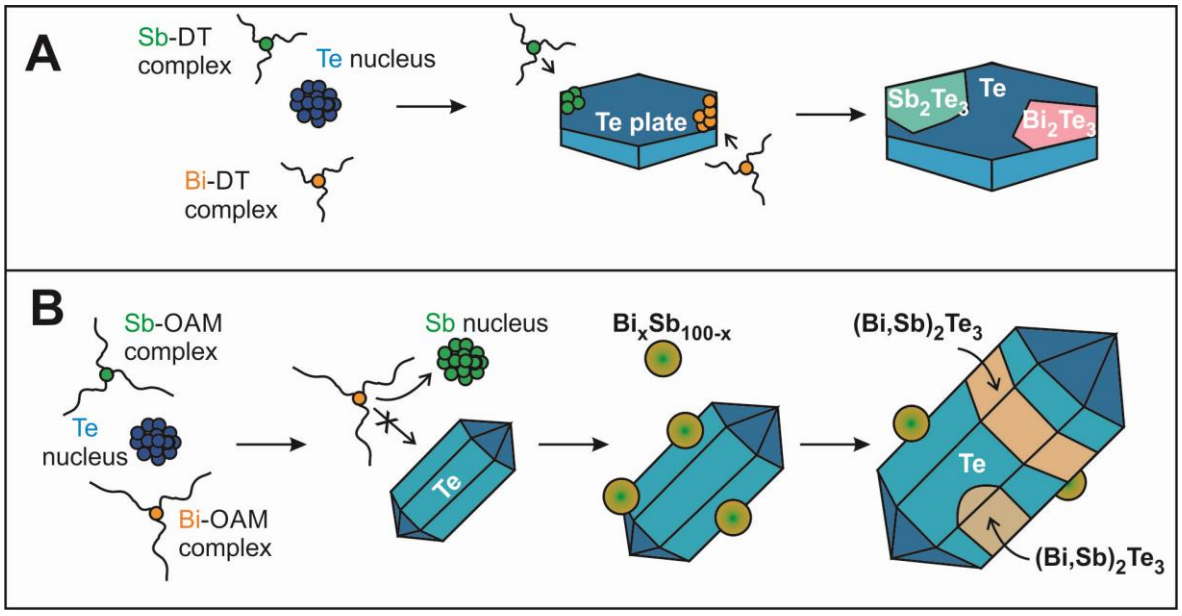

Figure 2.10. The illustration of the formation mechanisms for (A) Te/Bi_2Te_3/Sb_2Te_3 phase-segregated NDs synthesized using DT as a capping system and for (B) Te/$(Bi,Sb)_2Te_3$ NWs synthesized using OAM as a capping system.

2.4. Conclusion

In conclusion, we have partially addressed the complexity in the growth mechanism of trimetallic nanoparticles based on the synthesis and investigation of monometallic and bimetallic systems using various capping ligands. The use of different capping ligands in the complex formation and metallic interaction result in two different pathways in the formation of trimetallic NPs. Our study illustrates the formation of Bi_2Te_3 and Sb_2Te_3 based NPs due to the Te catalytic effect on the decomposition of the Sb and Bi precursor complexes. A bimetallic interaction was also observed in the case of using DT capping species. The formation of BiSb alloy in the OAM based capping system is important for the formation of a trimetallic alloy, which is observed in the triple elemental synthetic approach. The understanding of the NP formation mechanism arising from this expansive study gives a fundamental understanding of how to further control the composition, structure and characteristics of trimetallic NPs towards TE materials with enhanced and promising properties. Part of the ongoing work includes further delineation of the synthetic parameters, including precursor concentrations as well as characterization of the TE properties of these materials.

Acknowledgements

This work was supported by the Grant-in-Aid for Scientific Research (C). N. T. Mai thanks Drs. M. Koyano and K. Suekuni from JAIST for valuable advice and discussion.

References

[1] G. J. Snyder, E. S. Toberer, *Nat. Mater.* **2008**, *7*, 105.
[2] *Thermoelectrics Handbook: Macro to Nano*, D. M. Rowe, Ed. CRC Press: Boca Raton, FL, **2006**.
[3] M. V. Kovalenko, B. Spokoyny, J.-S. Lee, M. Scheele, A. Weber, S. Perera, D. Landry, D. V. Talapin, *J. Am. Chem. Soc.* **2010**, *132*, 6686.
[4] Y.-M. Lin, M. S. Dresselhaus, *Phys. Rev. B: Condens. Matter* **2003**, *68*, 075304.
[5] B. Yoo, F. Xia, K. N. Bozhilov, J. Herman, M. A. Ryan, N. V. Myung, *Adv. Mater.* **2007**, *19*, 296.
[6] A. E. Saunders, A. Ghezelbash, D.-M. Smilgies, M. B. Sigman, B. A. Korgel, *Nano Lett.* **2006**, *6*, 2959.
[7] R. Venkatasubramanian, E. Siivola, T. Colpitts, B. O'Quinn, *Nature* **2001**, *413*, 597.
[8] Y. Zhao, J. S. Dyck, B. M. Hernandez, C. Burda, *J. Phys. Chem. C* **2010**, *114*, 11607.
[9] Y. Q. Cao, T. J. Zhu, X. B. Zhao, X. B. Zhang, J. P. Thu, *Appl. Phys. A: Mater. Sci. Process.* **2008**, *92*, 321.
[10] S. H. Li, M. S. Toprak, H. M. A. Soliman, J. Zhou, M. Muhammed, D. Platzek, E. Muller, *Chem. Mater.* **2006**, *18*, 3627.
[11] S. H. Li, H. M. A. Soliman, J. Zhou, M. S. Toprak, M. Muhammed, D. Platzek, P. Ziolkowski, E. Muller, *Chem. Mater.* **2008**, *20*, 4403.
[12] F. Xiao, C. Hangarter, B. Yoo, Y. Rheem, K.-H. Lee, N. V. Myung, *Electrochim. Acta* **2008**, *53*, 8103.
[13] H. Ebe, M. Ueda, T. Ohtsuka, *Electrochim. Acta* **2007**, *53*, 100.
[14] A. Bailini, F. Donati, M. Zamboni, V. Russo, M. Passoni, C. S. Casari, A. L. Bassi, C. E. Bottani, *Appl. Surf. Sci.* **2007**, *254*, 1249.
[15] C. N. Liao, K. M. Liou, H. S. Chu, *Appl. Phys. Lett.* **2008**, *93*, 042103.
[16] S. S. Kim, S. Yamamoto, T. Aizawa, *J. Alloys Compd.* **2004**, *375*, 107.
[17] X. A. Fan, J. Y. Yang, R. G. Chen, W. Zhu, S. Q. Bao, *Mater. Sci. Eng. A* **2006**, *438*, 190.
[18] J. L. Cui, H. F. Xue, W. J. Xiu, L. Jiang, P. Z. Ying, *J. Solid State Chem.* **2006**, *179*, 3751.
[19] T.-S. Kim, B.-S. Chun, *J. Alloys Compd.* **2007**, *437*, 225.
[20] R. J. Mehta, C. Karthik, W. Jiang, B. Singh, Y. Shi, R. W. Siegel, T. Borca-Tasciuc, G. Ramanath, *Nano Lett.* **2010**, *10*, 4417.
[21] R. J. Mehta, C. Karthik, B. Singh, R. Teki, T. Borca-Tasciuc, G. Ramanath, *ACS Nano* **2010**, ***4***, 5055.

[22] X. F. Qiu, C. Burda, R. L. Fu, L. Pu, H. Y. Chen, J. J. Zhu, *J. Am. Chem. Soc.* **2004**, *126*, 16276.
[23] W. Wang, J. Goebl, L. He, S. Aloni, Y. Hu, L. Zhen, Y. Yin, *J. Am. Chem. Soc.* **2010**, *132*, 17316.
[24] Y. Xu, Z. Ren, G. Cao, W. Ren, K. Deng, Y. Zhong, *Mater. Lett.* **2008**, *62*, 4525.
[25] Y. Deng, C.-W. Nan, G.-D. Wei, L. Guo, Y. Lin, *Chem. Phys. Lett.* **2003**, *374*, 410.
[26] W. Lu, Y. Ding, Y. Chen, Z. L. Wang, J. Fang, *J. Am. Chem. Soc.* **2005**, *127*, 10112.
[27] A. Purkayastha, S. Kim, D. D. Gandhi, P. G. Ganesan, T. Borca-Tasciuc, G. Ramanath, *Adv. Mater.* **2006**, *18*, 2958.
[28] A. Scheele, N. Oeschler, K. Meier, A. Kornowski, C. Klinke, H. Weller, *Adv. Funct. Mater.* **2009**, *19*, 3476.
[29] J.-J. Kim, S.-H. Kim, S.-W. Suh, D.-U. Choe, B.-K. Park, J. R. Lee, Y.-S. Lee, *J. Cryst. Growth* **2010**, *312*, 3410.
[30] A. Purkayastha, Q. Y. Yan, M. S. Raghuveer, D. D. Gandhi, H. F. Li, Z. W. Liu, R. V. Ramanujan, T. Borca-Tasciuc, G. Ramanath, *Adv. Mater.* **2008**, *20*, 2679.
[31] G. Zhang, Q. Yu, Z. Yao, X. Li, *Chem. Commun.* **2009**, 2317.
[32] J. Yang, T. Aizawa, A. Yamamoto, T. Ohta, *J. Alloys Compd.* **2000**, *309*, 225.
[33] J. Jiang, L. Chen, S. Bai, Q. Yao, Q. Wang, *J. Cryst. Growth* **2005**, *277*, 258.
[34] Y. Xu, Z. Ren, W. Ren, K. Deng, Y. Zhong, *Mater. Lett.* **2008**, *62*, 763 .
[35] Y. Zhao, C. Burda, *ACS Appl. Mater. Interfaces* **2009**, *1*, 1259.
[36] M. Scheele, N. Oeschler, I. Veremchuk, K.-G. Reinberg, A.-M. Kreuziger, A. Komowski, J. Broekaert, C. Klinke, H. Weller, *ACS Nano* **2010**, *4*, 4283.
[37] D. Mott, N. T. Mai, N. T. B. Thuy, Y. Maeda, T. P. T. Linh, M. Koyano, S. Maenosono, *Phys. Status Solidi A* **2011**, *208*, 52.
[38] Z. Liu, Z. Hu, J. Liang, S. Li, Y. Yang, S. Peng, Y. Quian, *Langmuir* **2004**, *20*, 214.
[39] S. Saita, S. Maenosono, *Chem. Mater.* **2005**, *17*, 6624.
[40] D. D. Fanfair, B. A. Korgel, *Cryst. Growth Des.* **2008**, *89*, 3246.
[41] J.-L. Mi, N. Lock, T. Sun, M. Christensen, M. Søndergaard, P. Hald, H. H. Hng, J. Ma, B. B. Iversen, *ACS Nano* **2010**, *4*, 2523.
[42] Y. Deng, C. W. Nan, L. Guo, *Chem. Phys. Lett.* **2004**, *383*, 572.
[43] R. Malakooti, L. Cademartiri, Y. Akcakir, S. Petrov, A. Migliori, G. A. Ozin, *Adv. Mater.* **2006**, *18*, 2189.
[44] A. M. Ibrahim, D. A. Thompson, *Mater. Chem. Phys.* **1985**, *12*, 29.
[45] W. F. Ehret, M. B. Abramson, *J. Am. Chem. Soc.* **1934**, *56*, 385.
[46] Y. Li, J. Liu, *Chem. Mater.* **2001**, *13*, 1008.
[47] K. A. Abboud, R. C. Palenik, R. M. Wood, *Inorg. Chim. Acta* **2007**, *360*, 3642.

Chapter 3

Chemical Synthesis of BiSbTe Nanoparticles with Composition and Shape Manipulation

The ligand-directing chemical approach developed in chapter 2 have succeeded in synthesizing BiSbTe based nanoparticles (NP)s with capability of manipulating the morphology towards nanowires (NWs), nanodiscs (NDs) or nanoplates. However, at the same time, the strong correlation of composition and morphology in resulting NPs as well as their composition in-homogeneity are found and necessary to address. This chapter therefore mainly focuses on the control of NP compositions in correlation with morphology in terms of uniformity, homogeneity and ability to vary the composition. Based on the formation mechanism of BiSbTe ternary alloy NWs elucidated in the previous chapter, to obtain homogenous BiSbTe NPs with tunable composition and without preferential growth of Te NWs, a seed mediated growth chemical synthesis has been proposed. In the first step, an array of uniform $Bi_{1-x}Sb_x$ NPs with x ranging from 0 to 1 was synthesized *via* careful control of the feeding ratio and synthetic conditions. Then in the next step $Bi_{1-x}Sb_x$ NPs were used as the seeds for growth of BiSbTe NPs with controllable composition. The study further elucidates the key parameters for manipulation of the NP compositions.

3.1. Introduction

It is well know that the renewed interest of study on thermoelectric (TE) materials make this research field have become a hot topic with the main purpose is to overcome the limitation of the zT about 1 and make TE materials practical available with zT above 3.[1-2] The dimensionless figure of merit, zT, is given by $zT = T\alpha\sigma/\kappa$, where T, α, σ, and κ are absolute temperature, Seebeck coefficient, electrical and thermal conductivity, respectively, and κ is the sum of the thermal conductivity contributed from electron (κ_e) and phonon (κ_l). The challenges that limit the zT about 1 arise from the interrelated relations of the parameters defining zT, in which σ and electronic contributed to κ is proportional as given by Wiedemann-Franz's law, and the increase in α often goes with the decreasing of σ. To obtain the materials with enhanced zT, the current approaches are mainly laid on creating of materials satisfied the "phonon glass electron crystal" (PGEC) structure which possesses the glass-like thermal conductivity and electrical conductivity similar to crystal structure.[3] For that purpose, one can (i) introduce the nanostructure into the state of the art TE materials to make use of the large surface areas and size dependent properties of NPs to somewhat independently control the parameters (α, σ and κ) determining the TE efficiency,[4-7] or (ii) create the complex symmetric materials with crystal structure to make used of phonon rattling effect[8-10] or (iii) taking advantages of alloying in preserve the electrical conductivity and reduce thermal conductivity.[11,12] It is well known that the low dimensional materials with large area of grain boundary and suitable size can allow phonon scattering at the surface more effectively than electron scattering.[13,14] As a result, utilizing this advantage of the low dimensional materials can offer the larger reduction of thermal conductivity than that of electrical conductivity, or on the other words, decoupling the thermal and electrical conductivity to give rise in the TE efficiency and somehow create the PGEC materials.[13,14] Therefore, it is efficient to create the nanostructure of the state of the art TE alloys to further improve their TE performance.

Ternary solid solution BiSbTe are well known as promising p-type semiconductors for thermoelectric applications with one of the highest zT value of about 1.[15,16] Much of consideration and effort has been devoted to make BiSbTe ternary alloy in low dimensional structure because further reducing of κ_l in compensation for the decreasing σ is expected to further enhance the zT.[7,17,18] This idea attracted a great of interest from the experimentalists in synthesizing BiSbTe nanoparticles (NP)s and furthermore control the ternary solid solution NPs' characteristics such as size, shape and composition which are important factors contributing to the enhanced TE efficiency. However, it is challenging to well manipulate these

factors and producing uniform, homogenous NPs, especially, in case of the ternary element system in nano regime.[7,17,18] Regarding of chemical synthesis, it is the fact that only few facile syntheses is able to form ternary solid solution NPs.

From the previous study (chapter 2), it was found that the one-pot reaction is versatile in producing various morphologies of Bi, Sb and Te containing NPs, but the resulting single NPs are often heterogeneous in terms of phases and composition.[19] Under precise synthetic condition using OAM, ternary solid solution BiSbTe nanowires (NWs) can be grown. It was emphasized that the formation of Te and BiSb alloy NPs in the presence of OAM as the capping ligands is important for the formation of BiSbTe ternary solid solution NWs, however, the preferential growth of Te results in its existence as minor phase in a single NW.[19] Finally, it ends up with the fact that the composition and the morphology of the resulting NWs are hardly de-coupled and resulting BiSbTe ternary solid solution exist in narrow range of composition with minor undesirable Te phase. Therefore, based on the formation mechanism elucidated for BiSbTe ternary NWs, one of the particular interests is further development of the chemical approach towards synthesizing BiSbTe ternary alloy NPs with tailorable composition and morphology. In this chapter, a seed mediated growth synthesis of BiSbTe NPs is proposed with BiSb solid solution NPs as the seeds. The complete solubility of Bi and Sb in binary solid phase throughout entire range of compositions makes it possible to synthesize solid solution BiSb NPs with controllable composition. After that, BiSb NPs as the seeds are used to grow BiSbTe NPs and suppress the homogenous nucleation and growth of Te phase, aiming to better manipulation of their ternary composition, homogeneity and morphology. Additionally, the results in chapter 2 show that oleylamine supports the formation of BiSb solid solution NPs as well as the formation of ternary solid solution BiSbTe in NWs. Therefore, oleylamine is chosen as the capping agent for the seed mediated growth towards ternary solid solution BiSbTe NPs. The feeding ratio and temperature are the main parameters to tune the composition of the BiSb and BiSbTe NPs.

3.2. Experimental Section

3.2.1. Chemicals

Bismuth trichloride ($BiCl_3$, purity 99%), antimony trichloride ($SbCl_3$, purity 99%), tellurium tetrachloride ($TeCl_4$, purity 99%), oleylamine (OAM, purity 70%), 1,2-hexadecanediol (HDD, purity 90%), dioctylether (DOE, purity 99%) and diphenylether (purity

99%) were purchased from Sigma Aldrich Corp. as well as other common solvents. All reagents were used without further purification.

3.2.2. Synthesis of BiSb NPs

Binary solid solution BiSb NPs can be synthesized using either the bimetallic synthesis approach developed in chapter 2 (approach I) or the injection method (approach II). In both synthesis approaches, the molar feeding ratios of $BiCl_3$ to $SbCl_3$ equal to 1:2, 1:1 and 2:1 were used to tune the composition of the resulting NPs. In the first synthesis approach total 5.62×10^{-4} moles of $BiCl_3$ and $SbCl_3$ was added to 6.08×10^{-3} moles of OAM and 25 ml of DOE in a three neck flask under Ar gas bubbling and vigorous stirring for an hour. The flask was heated to 110 ^{o}C for 10 minutes to remove moisture and then heated to 195 ^{o}C and kept for 2 hours of reaction. In this synthesis approach, oleylamines have dual function as capping species and reducing agent at elevated temperature. The synthesis approach II is based on the injection of metal precursor complex stock solution into reducing solution at 250 ^{o}C. Stock solutions were prepared under Ar gas by mixing and heating total 5.00×10^{-4} moles of metal halide precursors in 1.5×10^{-3} moles of OAM and 10 mL of DOE to 60 ^{o}C for 10 min. The reducing solution was prepared under Ar gas by adding 1.5×10^{-3} moles of HDD along with the 1.5×10^{-3} moles of OAM into 15 ml of DOE, then heating to 250 ^{o}C. After the injection, the reaction solution turns to black quickly indicating the formation of NPs. The reaction was kept for an hour at 250 ^{o}C. After the reaction, the NP solution was quickly cooled to room temperature. Resulting NPs were purified using ethanol and hexane several times then collected for characterizations.

3.2.3. Synthesis of BiSbTe NPs

BiSb NPs were synthesized using phenylether as the solvent (while other conditions are kept constant) and used as the seeds to synthesize BiSbTe NPs. Half of the BiSb NPs in one batch of synthesis were redispersed in 10 mL of diphenylether and 3×10^{-3} moles of OAM, and stirred under Ar gas (Dispersion I). 0.843×10^{-4} mole of $TeCl_4$ and 4.5×10^{-3} moles of OAM were added into 15 ml of diphenylether and stirred under Ar gas until $TeCl_3$ completely dissolved to form Te stock solution. Te stock solution was added into the Dispersion I. The reaction solution was heated up to 195 ^{o}C and hold for 2 hours then cooled to room temperature. The resulting NPs were repeatedly washed with ethanol several times and collected for characterizations.

3.2.4. Instrumentation and analysis conditions

An array of instrumental techniques including X-ray diffraction (XRD), transmission electron microscopy (TEM), energy dispersive spectroscopy (EDS), inductively coupled plasma optical emission spectroscopy (ICP-OES) were used to characterize the size, shape, composition, structure and other properties of the materials.

XRD patterns were collected in reflection geometry using a Rigaku SmartLab X-ray diffractometer at room temperature with Cu Kα radiation (wavelength of 1.542 Å).

TEM analysis was performed on Hitachi H-7100 and H-7650 transmission electron microscopes operated at 100 kV. TEM samples were prepared by dropping the NP dispersions onto a carbon coated copper grid and natural drying in air overnight.

Samples for ICP-OES were prepared by dissolving dried NP samples in aqua regia then diluted for certain degree. The data were collected using a Shimazu Sequential Plasma Spectrometer ICPS-7000.

3.3. Results and Discussion

3.3.1. Binary solid solution BiSb NPs with controllable composition and morphology

The resulting BiSb NPs were characterized using TEM, TEM-EDS and XRD. Fig. 3.1 show the TEM images of BiSb NPs synthesized using different molar feeding ratios.

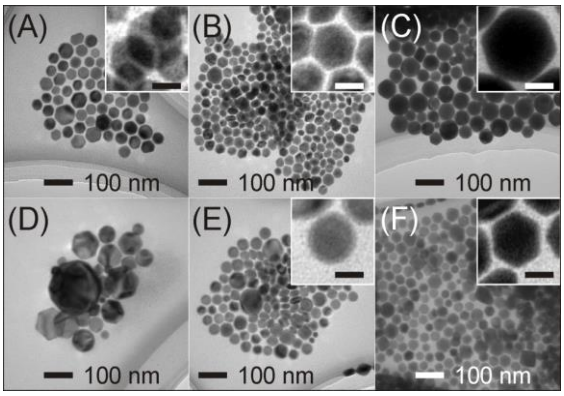

Figure 3.1. TEM images of BiSb NPs synthesized using approach I (upper row A-C) and II (lower row D-F) with Bi:Sb molar feeding ratio of 1:2, 1:1 and 2:1 (from left to right). The scale bars of the insets are 25 nm.

Almost all NPs are found to display hexagonal shape and with increasing $BiCl_3$ in the feeding ratios, NPs in synthesis approach I exhibit average diameters of 42.8 ± 8.1, 35.3 ± 6.6 and 56.9 ± 8.7 nm respectively and NPs in synthesis approach II have mean diameters of 63.1 ± 32.9, 38.4 ± 9.3, 38.7 ± 7.3 nm respectively. Additionally, the small thickness of NPs is clearly evidenced by the magnified TEM image captured for some overlapped NPs (inset of Fig. 3.1A), which clearly shows the different contrast between the overlapping areas compared to the surrounding (similar for some areas in Fig. 3.1B-F). Based on the contrast of the TEM images, it seems that NPs have a disk-like morphology with the thickness smaller than the diameter.

It is noted that the morphologies of resulting NPs in both syntheses are intermediate between those of single Bi and Sb NPs (Fig. 3.2). This is one of the contributions to the fact that BiSb solid solution NPs are formed in the syntheses which will be discussed later.

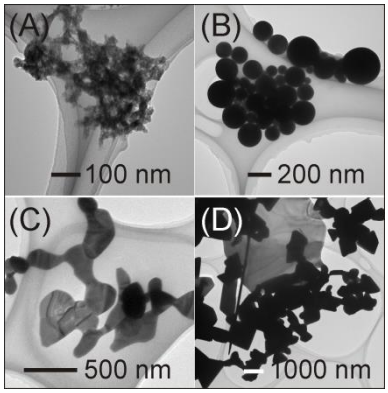

Figure 3.2. TEM images of single elemental Bi NPs (A, B) and Sb NPs (C, D) synthesized using synthesis approach I (left) and II (right) respectively.

The size and the uniformity in terms of the size and shape of the resulting BiSb NPs change according to the $BiCl_3$ to $SbCl_3$ molar feeding ratios (see Fig. 3.3 for the size distribution). The most uniformity in size and shape is obtained in both synthesis approaches using equal elemental molar feeding ratio with NPs size of 35.3 ± 6.6 nm and 38.4 ± 9.3 nm for synthesis approach I and II respectively. When the feeding ratios of two precursors are far from equal, the NP size becomes less uniform, which indicated that the comparative nucleation and growth of Bi and Sb can occur in the synthesis. It can be clearly observed that the resulting NPs in synthesis approach II became de-focused in size since the precursor molar feeding ratio of Bi:Sb equal to 1:2. The reduction rates of the precursors are also taken in to account for the

formation and growth of NPs. Compared to synthesis approach I, stronger reducing agent (HDD) and higher temperature (250 ^{o}C) used in synthesis approach II can allow precursors to be reduced simultaneously after the injection, but the nucleation and growth rate differences can become more significant than that in the first synthesis approach. As a result, it can contribute to the fact that NPs rich in Sb (elemental analysis will be shown later) may have larger size than the one rich in Bi as observed in synthesis approach II (Fig. 3.4).

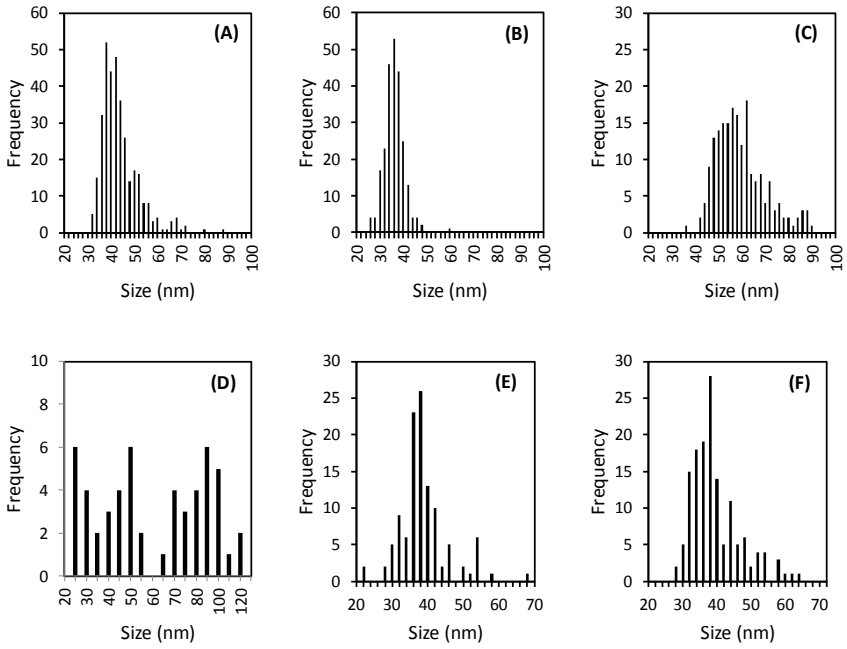

Figure 3.3. Size distributions of BiSb NPs synthesized using approach I (upper row A-C) and II (lower row D-F) with Bi to Sb molar feeding ratio of 1:2, 1:1 and 2:1 (from left to right).

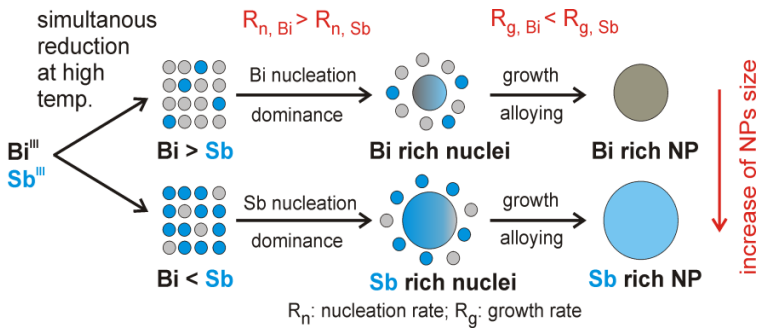

Figure 3.4. Illustration for the correlation between size and feeding ratios (then composition) of resulting BiSb NPs due to the differences in the nucleation and growth rate of Bi and Sb under the reaction conditions used in the injection method (synthesis approach II).

The XRD patterns were collected for resulting BiSb NPs (Fig. 3.5-3.6). XRD peak broadening was used to estimate the mean crystalline size of NPs (Table 3.1) based on Scherrer formula.[20] It is noteworthy that the mean crystalline size is similar or slightly smaller than the NP diameters measured from TEM images, which is in good agreement with the small size and disk like morphology of NPs, and suggests that binary solid solution NPs have good crystallinity.

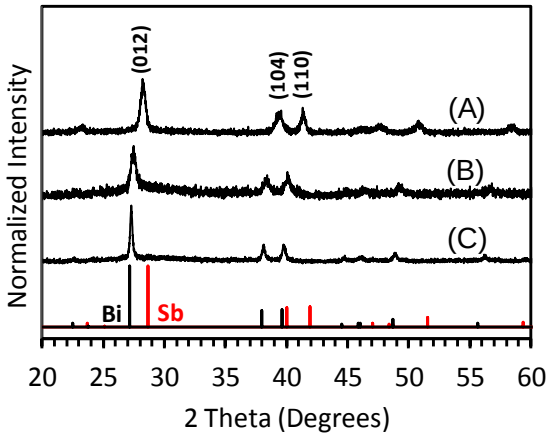

Figure 3.5. XRD patterns of BiSb NPs synthesized using approach I with $BiCl_3$:$SbCl_3$ molar feeding ratio of (A) 1:2, (B) 1:1 and (C) 2:1. The reference patterns of rhombohedral structural Bi (JSPS card no. 044-1246) and rhombohedral structural Sb (JSPS card no. 01-085-1322) were labeled by black and red colors.

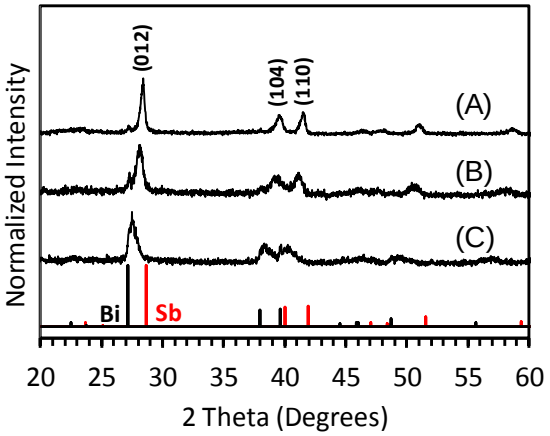

Figure 3.6. XRD patterns of BiSb NPs synthesized using approach II with $BiCl_3$:$SbCl_3$ molar feeding ratio of (A) 1:2, (B) 1:1 and (C) 2:1. The reference patterns of rhombohedral structural Bi (JSPS card no. 044-1246) and rhombohedral structural Sb (JSPS card no. 01-085-1322) were labeled by black and red colors.

Table 3.1 Summary of main results in composition, XRD peak position of (012) crystal plane and sizes of NPs for each synthesis approach

Approach	Molar feeding ratio $BiCl_3$:$SbCl_3$ (% Bi)	Composition [atomic %]	2 Theta [deg]	D_{TEM} [nm]	D_{XRD} [nm]
I	1:2 (33.3)	$Bi_{27.9}Sb_{72.1}$	28.20	42.8±8.1	26.7
	1:1 (50.0)	$Bi_{53.3}Sb_{46.7}$	27.42	35.3±6.6	27.4
	2:1 (66.7)	$Bi_{86.9}Sb_{13.1}$	27.24	56.9±8.7	54.7
II	1:2 (33.3)	$Bi_{25.0}Sb_{75.0}$	28.32	63.1±32.9	39.0
	1:1 (50.0)	$Bi_{50.1}Sb_{49.9}$	28.08	38.4±9.3	26.0
	2:1 (66.7)	$Bi_{74.4}Sb_{25.6}$	27.49	38.7±7.3	21.4

Compositions were measured by TEM-EDS for several single NPs. D_{TEM} and D_{XRD} represent the mean crystallize size and NP size calculated from TEM images and XRD patterns, respectively.

It can be seen in XRD patterns of Fig. 3.5 and Fig. 3.6 for NPs synthesized using the synthesis approach I and II respectively that all peaks are symmetric with peak positions in between the reference positions of pure Bi and pure Sb peaks. Except for the minor Bi peak in Fig. 3.6A, there is no sign of single phase Bi or Sb for all other cases. In addition, the TEM-EDS analysis confirmed that all single NPs contain Bi and Sb with average atomic composition nearly the feeding ratios of the elemental precursors (Table 3.1). Besides, the NPs are relatively uniform in size and shape (Fig. 3.1 and Fig. 3.3) with the morphology intermediate of the Bi and Sb single elemental NPs (Fig. 3.2). All the results indicate the formation of the binary solid solution BiSb NPs. Moreover, the peak position systematically shifted in a direction from the reference position of Sb towards the reference position of Bi in accordance with increasing the Bi composition of the resulting NPs, which suggests that the changes in lattice spacing due to the formation of Bi-Sb solid solution are strongly correlated with varying the NPs' compositions. This tendency is displayed in the XRD patterns of the resulting NPs synthesized using both approaches (Table 3.1). It is well known that Bi and Sb with rhombohedral structure can form the solid solution at any composition.[21,22] Therefore, the lattice spacings of (012) crystal planes (corresponding to the primary peak in XRD pattern) of the resulting NPs were plotted versus their composition in Fig. 3.7, where the lattice parameters were calculated from Bragg's law and the compositions were measured using TEM-EDS. Overall, the lattice spacing of the (012) crystal planes is in a linear relation to the measured composition by TEM-EDS, indicating that these materials obey Vegards law and are the binary solid solutions of Bi and Sb. While some points deviate slightly from the linear trend expected between lattice spacing and composition, this may arise as a result of slightly non-homogeneous alloy formation in these cases (i.e. the particles synthesized in approach I with a feeding ratio of Bi:Sb of 1:1).

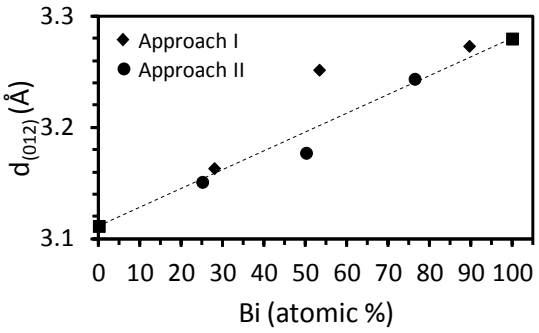

Figure 3.7. Relationship between the lattice spacing of (012) crystal plane of the synthesized BiSb NPs with the molar feeding ratios of $BiCl_3$ to $SbCl_3$ equal to 1:2, 1:1 and 2:1 and the corresponding composition of NPs measured by EDS. The data points for lattice spacing corresponding to pure Bi and pure Sb are labeled by squares (■) and a straight dash line connecting these 2 points is used for guidance.

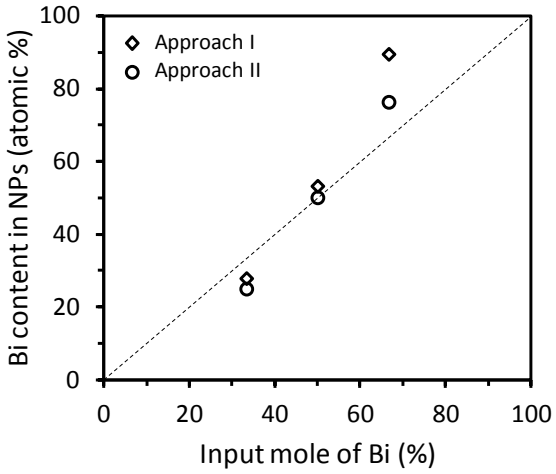

Figure 3.8. Relationship between the Bi content in NPs and the input moles of Bi precursor (in percentage). A linear line is used to guide the readers.

The composition of resulting NPs in both synthesis approaches can be controlled via tuning the feeding ratios of the precursors. We found a good linear relationship when the Bi content in resulting NPs was plotted versus Bi in metal precursors (in molar percentage) as shown in Fig. 3.8. In both synthesis approaches, the equal molar ratio of the precursors results in nearly equal molar ratio of metal composition in the resulting NPs, but higher or less Bi feeding ratios seem to cause higher or less Bi in the resulting NPs. This tendency is clear for NPs synthesized using approach I while the NPs synthesized using injection method seem to

have better equal relation between Bi content of the resulting NPs and that of the input precursors for a wide range of composition. It is reasonable because the nucleation and growth in the solution highly depends on the saturation concentration of the elemental atoms (Bi, Sb in this case). The nucleation and growth of Bi and Sb seem to occur simultaneously; therefore the elements with less concentration will reach the saturation conditions faster, which results in less content of the element in the resulting NPs than in the feeding ratios. Additionally, the reduction/decomposition rate of Sb and Bi may be different in the first synthesis, but it is likely that the injection methods, especially at high temperature, may be better in simultaneously producing both elemental atoms for growth of resulting NPs.

In summary, the binary solid solution BiSb NPs were successfully formed with controllable size and composition, and can be used for the next step to synthesize BiSbTe NPs.

3.3.2. Seed mediated growth of the ternary solid solution BiSbTe NPs

In this part, a case study of BiSbTe NPs using BiSb NPs as the seeds will be discussed. In this section, di-octylether solvent was exchanged to di-phenylether which is more suitable for scaling up the synthesis in future. The BiSb seed NPs were synthesized using phenylether which has composition of $Bi_{76}Sb_{24}$ measured by ICP-OES. The following will show the primary results of the synthesis of BiSbTe NPs at 195 ^{o}C. The reaction temperature was chosen based on the previous study (chapter2) in which it is known that at 200 ^{o}C BiSbTe ternary solid solution NPs can be obtained. The presence of BiSb NPs as the seeds can help to prevent the homogenous nucleation and growth of Te, which is easy to be reduced and grow up, causing the phase segregation (chapter 2), because BiSb NPs can offer high surface area for the reduction of Te and alloying. Furthermore, gradually heating is also expected to give a good condition for the gradual reduction of Te, prevent the high concentration of Te atom for the homogenous nucleation.

Fig. 3.9 shows the TEM images collected for resulting BiSbTe NPs synthesized using the $Bi_{76}Sb_{24}$ NPs as the seeds. It can be seen in the TEM images that the size of resulting BiSbTe of 80-100 nm which is bigger than the diameter of the $Bi_{76}Sb_{24}$ NPs (42 ± 10 nm). Additionally, the BiSbTe NPs display the similar morphology to the BiSb seeds. The results indicate the possibility that Te was incorporated into the seed NPs.

ICP-OES and XRD were utilized to analyze the composition and structure of BiSbTe NPs. The ICP-OES result shows the composition of $Bi_{37}Sb_{12}Te_{51}$. The molar ratio of Bi and Sb in the resulting BiSbTe NPs is similar to that of the BiSb seeds, furthermore indicating that the composition of the seed is maintained in the BiSbTe NPs. Because Bi_2Te_3 and BiSbTe have

similar crystal structure, the existing of Sb indicated by ICP-OES analysis and the absence of Sb or Sb oxides phase in XRD pattern are important for assignment of $(Bi_{1-x}Sb_x)_2Te_3$ or Bi_2Te_3 phases, where x ranges from 0 to 1. BiSbTe was found with Te as the very minor phase as shown in the XRD pattern (Fig. 3.10, see Appendix III for detail of the peak assignment). All these results together indicate that the ternary BiSbTe NPs can be obtained using the BiSb NPs as the seed, in which the morphology and composition of the BiSbTe NPs is similar to the seed NPs. The formation of Te phase can be suppressed with further control of the Te precursor concentration and the reaction temperature.

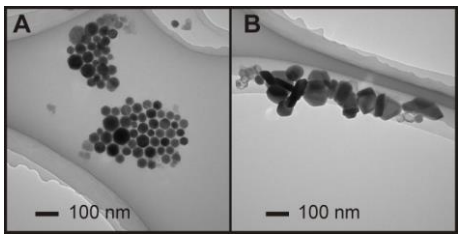

Figure 3.9. TEM images of BiSb seed NPs redispersed in diphenylether (A) and BiSbTe NPs synthesized at 195 ^oC (B), using OAM as the reducing agent and capping ligand with the seed's composition of $Bi_{74}Sb_{26}$.

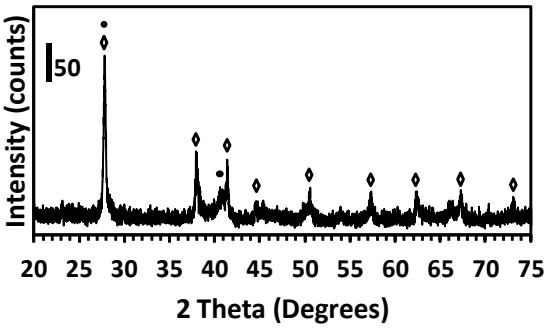

Figure 3.10. XRD patterns of BiSbTe NPs synthesized at 195 ^oC, using OAM as the reducing agent and capping ligand. The BiSb seed NPs were synthesized with $BiCl_3$:$SbCl_3$ feeding ratio of 1:1. The identities of the peaks were labeled by open diamond (◊) for BiSbTe (JSPS card no. 01-072-1835) and black circle (●) for Te hexagonal structure (JSPS card no. 036-1452).

3.4. Conclusion

In conclusion, the chemical synthesis approach was illustrated to be straightforward in preparation of BiSb seed NPs and BiSbTe NPs with controllable composition and morphology.

The seed mediated growth technique developed in our study exhibits a strong potential in tailoring the NPs composition and morphology towards designed structures. Further investigation of synthesis conditions can help fully control the ternary solid solution BiSbTe NPs in term of their composition, uniformity, homogeneity and phases.

Acknowledgement

N. T. Mai would like to thank Satoru Kodaira and Md. Shahiduzzaman for their cooperation in conducting the experiment during this project.

References

[1] H. J. Goldsmid, *In Thermoelectric Handbook Macro to Nano*, ed. by D. M. Rowe, 10-1, CRC Press, Boca Raton, FL **2006**.

[2] A. V. Dmitriev, I. P. Zvyagin, *Physics-Uspekhi* **2010**, *53*, 789.

[3] G. A. Slack, *In CRC Handbook of Thermoelectrics*, ed. by D. M. Rowe, p. 147, CRC Press, Boca Raton, FL **1995**.

[4] L. D. Hicks, M. S. Dresselhaus, *Phys. Rev. B* **1993**, *47*, 12727.

[5] R. Venkatasubramanian, *In Semiconductors and Semimetals*, ed. R. K. Willardson, E. R. Weber, Vol 71, Academic Press, San Diego, CA **2001**.

[6] R. Venkatasubramanian, E. Siivola, T. Colpitts, B. O`Quinn, *Nature* **2001**, *413*, 597.

[7] A. Scheele, N. Oeschler, I. Veremchuk, K.-G. Reinsberg, A.-M. Kreuziger, A. Kornowski, J. Broekaert, C. Klinke, H. Weller, *ACS Nano* **2010**, *4*, 4283.

[8] G. S. Nolas, J. L. Cohn, G. A. Slack, *Phys. Rev. B* **1998**, *58*, 164.

[9] G. A. Slack, V. G. Tsoukala, *J. Appl. Phys.* **1994**, *76*, 1665.

[10] G. S. Nolas, D. T. Morelli, T. M. Tritt, *Ann. Rev. Mater. Sci.* **1999**, *29*, 89.

[11] A. F. Ioffe, S. V. Airapetyants, A. V. Ioffe, N. V. Kolomoets, L. S. Stil'bans, *Dokl. Akad. Nauk., SSSR* **1956**, *106*, 981.

[12] M. S. Abrahams, R. Braunstein, F. D. Rosi, *J. Phys. Chem. Solids* **1959**, *10*, 204.

[13] T. C. Harman, D. L. Spears, M. P. Walsh, *J. Electron. Mater.* **1999**, *28*, L1.

[14] M. S. Dresselhaus, G. Chen, M. Y. Tang, R. G. Yang, H. Lee, D. Z. Wang, Z. F. Ren, J.-P. Fleurial, P. Gogna, *Adv. Mater.* **2007**, *19*, 1043.

[15] G. J. Snyder, E. S. Toberer, *Nat. Mater.* **2008**, *7*, 105.

[16] M. G. Kanatzidis, *Chem. Mater.* **2010**, *22*, 648.

[17] Y. Zhao, C. Burda, *ACS Appl. Mater. Interfaces* **2009**, *1*, 1259.

[18] M. V. Kovalenko, B. Spokoyny, J.-S. Lee, M. Scheele, A. Weber, S. Perera, D. Landry, D. V. Talapin, *J. Am. Chem. Soc.* **2010**, *132*, 6686.

[19] N. T. Mai, D. Mott, N. T. B. Thuy, I. Osaka, K. Higashimine, M. Koyano, S. Maenosono, *RSC Adv.* **2011**, *1*, 1089.

[20] Scherrer, Gttinger Nachrichten Gesell. **1918**, *2*, 98.

[21] A. M. Ibrahim, D. A. Thompson, *Mater. Chem. Phys.* **1985**, *12*, 29.

[22] W. F. Ehret and M. B. Abramson, *J. Am. Chem. Soc.* **1934**, *56*, 385.

Chapter 4

One-pot Chemical Synthesis of Zinc Antimonide Nanoparticles as Building Blocks for Nanostructured Thermoelectric Materials

This chapter reports a one-pot chemical synthesis of zinc antimonide (Zn-Sb) nanoparticles (NPs) *via* a sequential reduction of metal precursors and subsequent compositional redistribution. The NP's characteristics were carefully investigated using wide range of analytical methods to elucidate the complex structure of the resulting NPs. Chemically-synthesized Zn-Sb NPs are expected to be promising building blocks for nanostructured thermoelectric materials.

4.1. Introduction

Thermoelectric (TE) materials have currently attracted much attention due to the immediate applicability to energy harvesting.[1,2] However, an improvement of TE efficiency is required for practical realization of these devices. One of the most promising approaches toward the enhancement of TE efficiency is a phonon-glass electron-crystal (PGEC) approach.[3-5] Zn-Sb systems (especially β-Zn_4Sb_3 phase) exhibit excellent TE properties because of their remarkably low thermal conductivity (κ) due to the disordered local (PGEC) structure.[6-12] In addition, Zn-Sb consists of relatively abundant elements, and thus, it has been regarded as a promising candidate for TE energy harvesting. Zn-Sb systems have invited various investigations ranging from fabrication to structure-property relation.[12] With respect to the fabrication of Zn-Sb alloy, physical methods have been mostly used such as ball-milling,[13] mechanical alloying,[14] zone melting,[15] spark plasma sintering,[16] and hot pressing.[17] To tailor the TE properties of Zn-Sb, the doping of a third element into the Zn-Sb bulk crystal has prevailed to enhance the TE efficiency.[18-20]

Nanostructuring of TE materials enables the reduction of κ while retaining the electrical conductivity, and thus, leads to an enhancement in TE efficiency. It has been demonstrated that nanostructured TE materials fabricated using TE NPs as building blocks can exhibit significant reduction in κ and better control over the resulting characteristics.[21,22] Recently, a few chemical approaches toward Zn-Sb nanostructures have been proposed. For example, Zn@Sb core-shell particles were synthesized first, and then, nanostructured Zn-Sb compound was formed by annealing Zn@Sb core-shell particles at 300 ^{o}C for 6 hours.[23] However, NPs are sensitive to heat because of crystal growth during longer heating periods, and thus, undesirable grain growth cannot be avoided during the reaction. In another approach, based on the solid state reaction of activated powders of Zn and Sb pioneered by Schlecht *et al.*,[24] Tremel and coworkers developed a new synthetic method to obtain Zn-Sb NPs *via* a peritectoid reaction between differentially-synthesized Zn and Sb NPs in an organic solvent at about 300 ^{o}C.[25,26] In this case, it is also somewhat difficult to control the grain size, which is crucially important for TE properties, because coalescence of the NPs takes place during the peritectoid reaction. In either case, it isn't possible to synthesize well-defined Zn-Sb NPs in terms of morphology and uniformity. Unfortunately, however, the direct chemical synthesis of Zn-Sb NPs has not been achieved yet. In this study, Zn-Sb NPs were chemically synthesized *via* a sequential reduction of metal precursors and subsequent alloying. The synthesis starts with the formation of Sb cores followed by the growth of Zn shell onto the cores. This chemical approach with the well control

of the core in term of size and shape and the deposition of the shell is expected to give better control on the resulting NPs.

4.2. Experimental Section

4.2.1. Chemicals

$ZnCl_2$ (purity 98%), $SbCl_3$ (purity 99%), dioctyl ether (DOE, purity 99%), oleylamine (OAM, purity 70%) and lithium triethylborohydride ($LiBHEt_3$, 1M solution in THF) were purchased from Sigma Aldrich and used without further purification. Other common solvents were purchased from Kanto Chemical and used as received.

4.2.2. Synthesis of Zn-Sb NPs

The synthesis was carried out in a three-neck flask under an Ar atmosphere. 0.1 mmol of $SbCl_3$ and 0.6 mmol of OAM were put in 3 ml of DOE and heated up to 60 °C under stirring (stock solution 1). Separately, 0.1 mmol of $ZnCl_2$ and 0.4 mmol of OAM were put in 10 mL of DOE and heated up to 200 °C (stock solution 2). 0.3 mL of $LiBHEt_3$ and 12 ml of DOE were put into the flask and heated up to 250 °C under Ar (matrix solution). Then, 3 mL of stock solution 1 was rapidly injected into the matrix solution. The color of the reaction solution turned to black immediately after the injection. After 30 min of the reaction at 250 °C, the temperature of the reaction solution was quickly reduced to 200 °C. Subsequently, 10 mL of stock solution 2 preheated at 200 °C was injected into the reaction solution followed by the injection of 0.2 mL of $LiBHEt_3$. The reaction was continued for 1 hour at 200 °C. After the reaction, the temperature of the reaction solution was quickly cooled to room temperature, and then a mixture of ethanol and hexane (1:1 volume ratio) was added to the reaction solution followed by centrifugation at 5000 rpm. This purification process was repeated several times to obtain the final product.

4.2.3. Synthesis of Sb NPs

0.1 mmol of $SbCl_3$ and 0.6 mmol of OAM were put in 3 ml of DOE and heated up to 60 °C under stirring (stock solution 1). 0.3 mL of $LiBHEt_3$ and 12 ml of DOE were put into the flask and heated up to 250 °C under Ar (matrix solution). Then, 3 mL of stock solution 1 was rapidly injected into the matrix solution. The color of the reaction solution turned to black immediately after the injection. After 30 min of the reaction at 250 °C, the temperature of the

reaction solution was quickly reduced to room temperature. The resulting Sb NPs were purified and collected for further analysis.

4.2.4. Synthesis of Zn NPs

0.2 mmol of $ZnCl_2$ and 0.8 mmol of OAM were put in 20 mL of DOE and heated up to 200 °C. Then, 0.4 mL of $LiBHEt_3$ was injected into the solution. The reaction was continued for 1 hour at 200 °C. The resulting Zn NPs were purified and collected for further analysis.

4.2.5. Instrumentation and analysis conditions

X-ray diffraction and X-ray photoelectron spectroscopy

X-ray diffraction (XRD) patterns of NPs were collected in reflection geometry using a Rigaku SmartLab X-ray diffractometer at room temperature with Cu Kα radiation.

For X-ray photoelectron spectroscopy (XPS), the dried NPs were put on carbon tape and measurements were performed on a Shimadzu Kratos AXIS-ULTRA DLD high performance XPS system. Photoelectron was excited by monochromated Al Kα radiation. Detection was done with a delay-line detector (DLD) and a concentric hemispherical analyzer (CHA). The X-ray tube was operated at 150 W. The pass energy of the CHA was 20 eV for narrow-scan spectra. The analyzed area on the specimen surface was 300×700 μm^2 and was located in the center of the irradiated region. The instrument was operated at a vacuum level of 1×10^{-8} Torr.

TEM measurement

As-synthesized NPs were redispersed in ethanol with the addition of OAM. 10 μL of the NP dispersion was dropped onto a carbon-coated TEM grid and completely dried in ambient conditions. TEM and high-resolution TEM imaging were performed on Hitachi H-7650 and H-9000NAR transmission electron microscopes operated at 100 kV and 300 kV, respectively. High-angle annular dark-field scanning TEM (HAADF-STEM) imaging and energy dispersive X-ray spectroscopy (EDS) elemental mapping were carried out using a JEOL JEM-ARM200F instrument operated at 200 kV with a spherical aberration corrector.

Seebeck coefficient measurement

A sample for the Seebeck coefficient measurement was prepared by the following procedures.

Purification of Zn-Sb NPs: as-synthesized Zn-Sb NPs were washed with hexane (3 times) and ethanol (2 times), and then, allowed to precipitate spontaneously. Finally, the precipitates were redispersed in hexane and centrifuged to obtain final product.

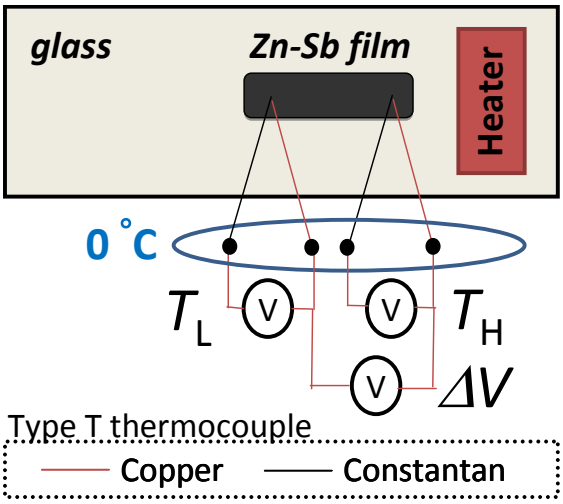

Figure 4.1. Schematic illustration of the configuration for Seebeck measurement

Thin film fabrication: Purified Zn-Sb NPs were put onto a mica substrate followed by drying under N_2 gas flow (50 mL/min) for 2 h. Then, another mica substrate was put on the NPs sandwiching the NPs between two glass slides. By applying the pressure of 20 MPa, a strip-shaped thin film of NPs was fabricated on the mica substrate.

Electrodes were attached on either end of the NP film to monitor temperature and voltage (Fig. 4.1). A manganin heater was placed near the one end of the NP film to generate a thermal gradient between two electrodes (ΔT). By measuring the Seebeck voltage as a function of ΔT, the Seebeck coefficient was obtained.

4.3. Results and Discussion

4.3.1. Morphology, composition, structure and surface properties of Zn-Sb NPs

Zn-Sb NPs were chemically synthesized *via* a sequential reduction of metal precursors and subsequent alloying. Before the growth of the Zn shell, Sb NPs with rhombohedral structure as the core were formed (Fig. 4.2). In a separate experiment, the synthesis of Zn NPs was performed in the absence of Sb cores. As a result, Zn NPs of mean size of 80.2±11.5 nm were obtained (Fig.4.3).

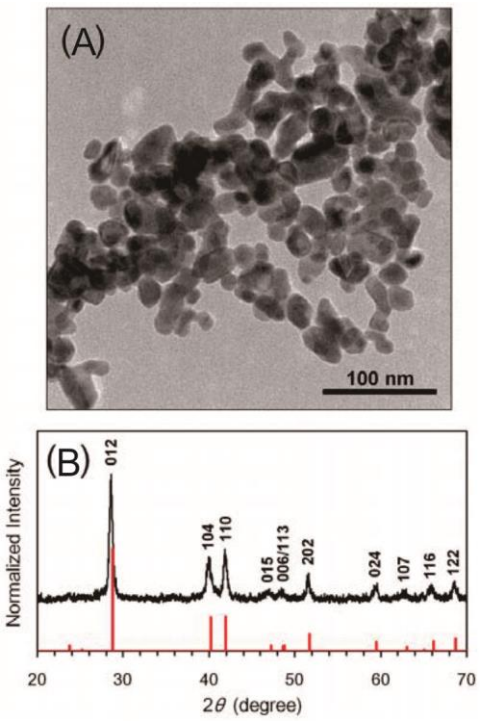

Figure 4.2. TEM image (A) and XRD pattern (B) of Sb NPs. All XRD peaks were identical with those of rhombohedral Sb (JCPDS card no. 01-085-1324).

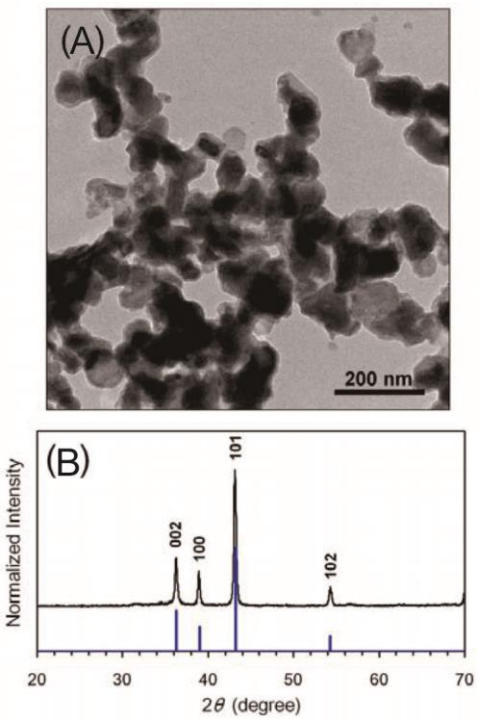

Figure 4.3. TEM image (A) and XRD pattern (B) of Zn NPs. All XRD peaks were identical with those of rhombohedral Sb (JCPDS card no. 01-085-1324).

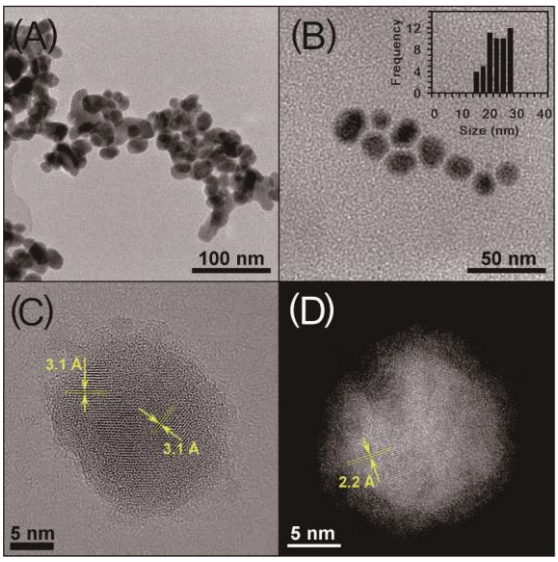

Figure 4.4. TEM images of Zn-Sb NPs (A, B) (the inset in (B) shows the size distribution of NPs), high-resolution TEM (C) and HAADF-STEM image (D) of a single Zn-Sb NP.

Fig. 4.4A-C shows TEM images indicating that the resulting as-synthesized NPs are nearly spherical in shape and have a mean size of 21.1±3.4 nm. The mean size and size distribution of NPs were estimated from randomly-selected NPs observed in the TEM images (Fig. A4.1, Appendix IV). TEM-EDS analysis on single NPs as well as an ensemble of NPs confirmed that each NP contains both Zn and Sb with an average atomic ratio of Zn:Sb = 47:53. Fig. 4.4D shows the high-angle annular dark-field scanning transmission electron microscopy (HAADF-STEM image). As can be seen, the Z contrast decreases from center to edge suggesting that Zn is rich at the periphery while Sb is rich in the core. The lattice fringes with different d-spacings can be clearly resolved in Fig. 4.4C and D. However, it is difficult to determine which phase these crystal planes belong to because several different phases have lattice planes with similar d-spacing.

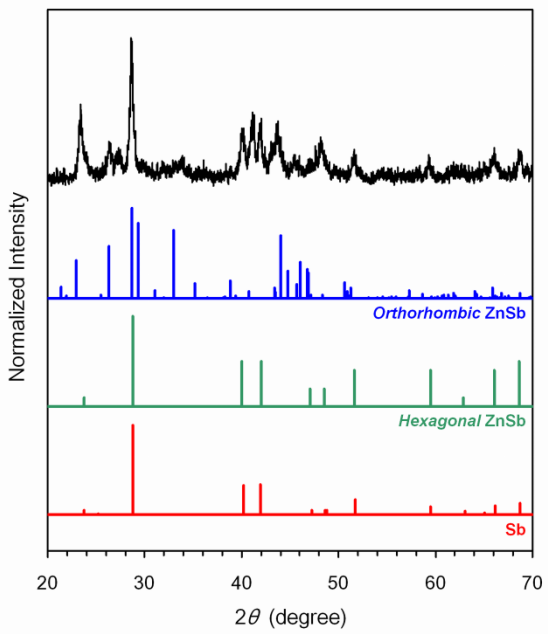

Figure 4.5. XRD pattern of Zn-Sb NPs (black curve). Red, green, and blue colors represent Sb (JCPDS No. 01-085-1324), hexagonal ZnSb (JCPDS No. 00-018-0140), and orthorhombic ZnSb (JCPDS No. 01-073-7857), respectively.

Fig. 4.5 shows the XRD pattern of the Zn-Sb NPs indicating that the NPs consist of several different phases including hexagonal ZnSb (and/or rhombohedral Sb), and orthorhombic ZnSb. No oxide related peak and no metallic Zn peak is observed in the XRD

pattern, while an unidentified peak at around $2\theta = 41^{o}$ is observed. Importantly, the XRD pattern does not correspond to any other phase including Zn_3Sb_2,[27,28] Zn_4Sb_3,[25,29] and Zn_8Sb_7.[25] It is worth noting that some peaks are abnormally broadened and asymmetric suggesting the overlapping reflections. It is also important to note that the XRD peak positions of hexagonal ZnSb are almost identical with those of rhombohedral Sb, and thus, we cannot rule out the existence of a pure Sb phase. Whatever the case, it is difficult to precisely determine the phases and their fraction in principle because of significant peak broadening and overlapping.

The surface properties of Zn-Sb NPs were analyzed using XPS. The high resolution XPS core-level spectra of the Zn-Sb NPs were shown in Fig. 4.6 while that of Zn NPs and Sb NPs were shown in Fig. 4.7.

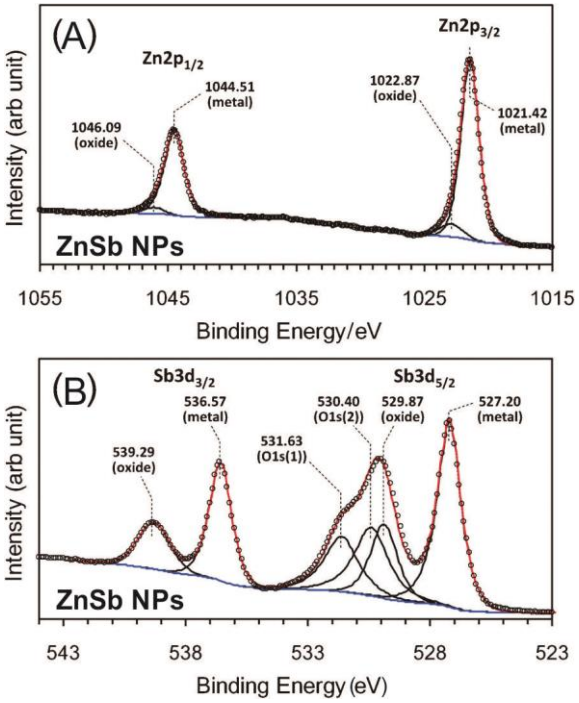

Figure 4.6. XPS spectra of Zn-Sb NPs, (A) Zn 2p and (B) Sb 3d areas.

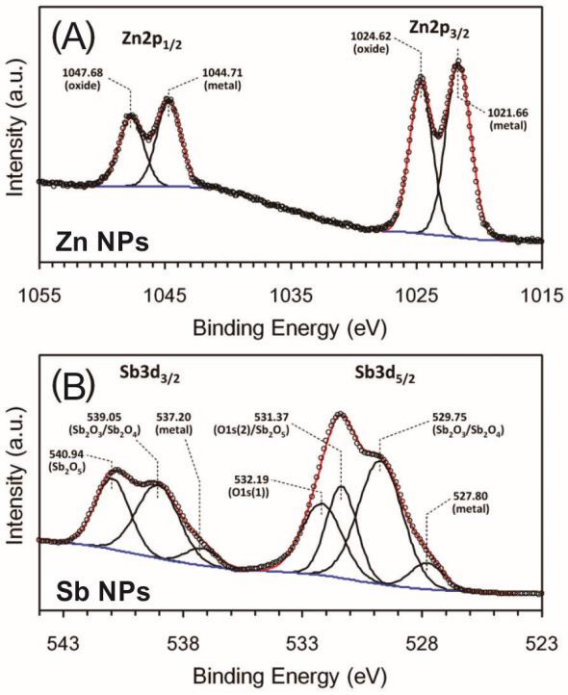

Figure 4.7. XPS spectra of (A) Zn 2p area of Zn NPs and (B) Sb 3d area of Sb NPs.

For Zn-Sb NPs, Zn and Sb NPs, the asymmetrically broadened 2p peaks were deconvoluted by using Gaussian-Lorentzian mixed functions corresponding to Zn and ZnO (for detail see Appendix IV, Table A4.1 and 3). Similarly, the Sb $3d_{3/2}$ and Sb $3d_{5/2}$ peaks were deconvoluted for Sb, Sb_xO_y, and O 1s (see Appendix IV, Table A4.2 and 3). For both elements, the majority is found in Zn-Sb NPs to be metallic. ZnO and Sb_xO_y detected in XPS are

indicative of a surface oxide layer which is undetectable in XRD. It has been reported that Zn 2p and Sb 3d XPS peaks in Zn-Sb alloy are almost identical to those of metallic Zn and Sb.[30] Therefore, it is reasonable to consider that Zn and Sb atoms are incorporated in the NPs in the form of alloy because no metallic Zn phase was observed in the XRD pattern. It is important to note that a significant fraction of oxide was detected in the XPS spectra in the cases of Zn and Sb NPs synthesized under the same conditions unlike Zn-Sb NPs. Although the real reason why Zn-Sb NPs becomes resistant to oxidation is not clear, the enhancement of oxidation stability in Zn-Sb NPs (even if the surface is Zn rich) may be due to the alloying. It is well-known that Pb-Sb eutectic alloys, which have been the most common grid alloy system in automobile-type batteries, show an enhanced corrosion resistance even though the content of Sb is low (typically ranging from 4 to 12 wt%).[31] Piecing together all analytical results, it can be concluded that the resulting Zn-Sb NPs have an Sb-rich core and Zn-rich surface with a composition gradient along the radial direction as a result of being composed of multiple ZnSb phases.

To confirm the composition distribution in the Zn-Sb NPs, EDS mapping was carried out for a single Zn-Sb NP (Fig. 4.8). Both Zn and Sb are found to be distributed over the entire area of a single NP. The cross-sectional line profile (Fig. 4.8E) confirmed that Sb is rich in the center and Zn content increases at the periphery (vice versa for Sb). Similar results were obtained for other single NPs indicating that this structural feature is typical and uniform. It has been reported that Zn-Sb solid solutions with various compositions are formed above 360 ^{o}C.[32] In addition, the fast diffusion of Zn into Zn-Sb alloy is known to take place even at low temperature, ca. 195 ^{o}C.[33] Based on these facts, Zn atoms are considered to rapidly diffuse into the core to form Zn-Sb alloy NPs at low temperature (200 ^{o}C) because of the relatively small size of the Sb cores.

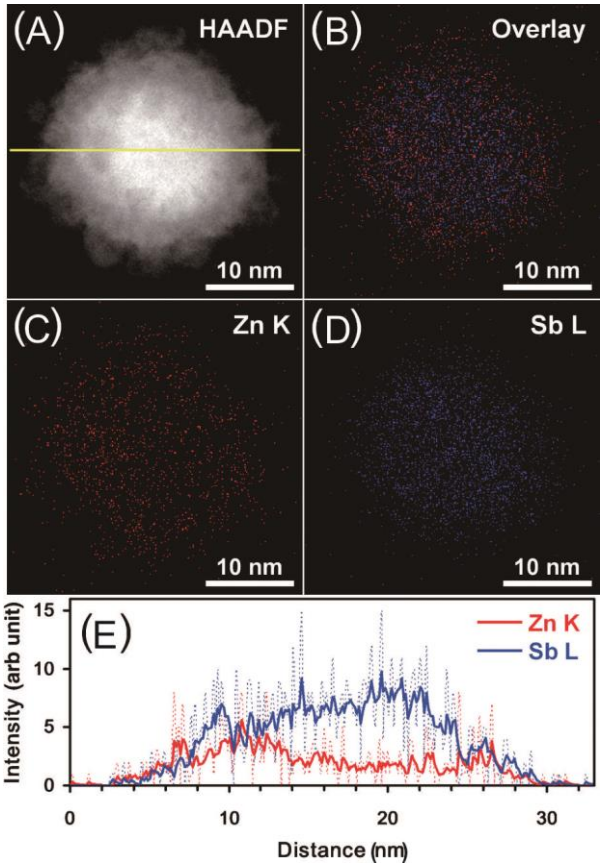

Figure 4.8. (A) HAADF-STEM and (B-D) EDS elemental mapping images of a Zn-Sb NP: overlay (B) of Zn K edge (C) and Sb L edge (D), (E) the EDS line profile at the center of the NP as indicated by a yellow line in (A). Dashed and solid lines represent raw and low-pass-filtered profiles, respectively.

4.3.2. Seebeck coefficient of the powder of Zn-Sb NPs

The Seebeck coefficient (S) of a compressed specimen of Zn-Sb NPs on a glass plate was measured (Fig. 4.1). The S value was approximately +25 μV/K with p-type at around room temperature, which was lower than for the Zn-Sb bulk crystals (~70 μV/K at 300 K) including ZnSb, Zn_4Sb_3 and Zn_8Sb_7.[34] Lowering of the S value for the Zn-Sb NPs results from the compositional inhomogeneity, probably due to the partial oxidation at the surface and/or the incomplete optimization of the interparticle properties such as the removal of the surface capping molecules, good electrical contacts between NPs in the compressed specimen.

4.4. Conclusion

In conclusion, this one-pot synthesis method has been proven to be able to synthesize compositionally gradient Zn-Sb NPs. The Zn-Sb NPs are relatively uniform, dispersible in nonpolar solvent, and resistive to oxidation. The present synthetic technique offers a new approach toward nanostructured Zn-Sb TE materials. If necessary, the composition gradient in a single NP can be uniformized during sintering at higher temperatures to fabricate nanostructured Zn-Sb TE materials, which will be the target of the next chapter. In addition, by changing the molar feeding ratio of Zn to Sb, it will be able to tune the crystal phase of nanostructured Zn-Sb TE materials, e.g. Zn_3Sb_2, Zn_4Sb_3, Zn_8Sb_7. However, a full characterization of the TE properties of these Zn-Sb NPs is still challenging in terms of scaling up the reaction to obtain enough amount of NPs, the existence of surface organic ligands, the optimization of the sample processing, the interparticle properties, the composition, among other factors. Part of this work is to be performed and discussed in the next chapter.

Acknowledgement

N. T. Mai would like to thank Drs. M. Koyano and K. Suekuni from JAIST for helping with the Seebeck coefficient measurement.

References and Notes

[1] *Thermoelectrics Handbook: Macro to Nano*, ed. by D. M. Rowe, CRC Press, Boca Raton, FL, **2006**.
[2] G. J. Snyder, E. S. Toberer, *Nat. Mater.* **2008**, *7*, 105.
[3] C. J. Vineis, A. Shakouri, A. Majumdar, M. G. Kanatzidis, *Adv. Mater.* **2010**, *22*, 3970.
[4] T. C. Harman, W. P. Walsh, B. E. Laforge, G. W. Turner, *J. Electron. Mater.* **2005**, *34*, 19.
[5] M. G. Kanatzidis, *Chem. Mater.* **2010**, *22*, 648.
[6] G. J. Snyder, M. Christensen, E. Nishibori, T. Caillat, B. B. Iversen, *Nat. Mater.* **2004**, *3*, 458.
[7] L. Bjerg, G. K. H. Madsen, B. B. Iversen, *Chem. Mater.* **2011**, *23*, 3907.
[8] F. Cargnoni, E. Nishibori, P. Rabiller, L. Bertini, G. J. Snyder, M. Christensen, C. Gatti, B. B. Iversen, *Chem. Eur. J.* **2004**, *10*, 3861.
[9] S. Bhattacharya, R. P. Hermann, V. Keppens, T. M. Tritt, G. J. Snyder, *Phys. Rev. B* **2006**, *74*, 134108.
[10] H. J. Kim, E. S. Božin, S. M. Haile, G. J. Snyder, S. J. L. Billinge, *Phys. Rev. B* **2007**, *75*, 134103.
[11] W. Chen, J. Li, *Appl. Phys. Lett.* **2011**, *98*, 241901.

[12] A. S. Mikhaylushkin, J. Nylen, U. Häussermann, *Chem. Eur. J.* **2005**, *11*, 4912.
[13] P. H. M. Böttger, K. Valset, S. Deledda, T. G. Finstad, *J. Electron. Mater.* **2010**, *29*, 1583.
[14] V. Izard, M. C. Record, J. C. Tedenac, *J. Alloys Compd.* **2002**, *345*, 257.
[15] B. L. Pedersen, B. B. Iversen, *Appl. Phys. Lett.* **2008**, *92*, 161907.
[16] T. Souma, G. Nakamoto, M. Kurisu, *J. Alloys Compd.* **2002**, *340*, 275.
[17] J. H. Ahn, M. W. Oh, B. S. Kim, S. D. Park, B. K. Min, H. W. Lee, Y. J. Shim, *Mater. Res. Bull.* **2011**, *46*, 1490.
[18] H.-J. Gau, J.-L. Yu, C.-C. Wu, Y.-K. Kuo, C.-H. Ho, *J. Alloys Compd.* **2009**, *480*, 73.
[19] X. Y. Qin, M. Liu, L. Pan, H. X. Xin, J. H. Sun, *J. Appl. Phys.* **2011**, *109*, 033714.
[20] J. L. Cui, L. D. Mao, D. Y. Chen, X. Qian, X. L. Liu, W. Yang, *Curr. Appl. Phys.* **2009**, *9*, 713.
[21] A. Scheele, N. Oeschler, K. Meier, A. Kornowski, C. Klinke, H. Weller, *Adv. Funct. Mater.* **2009**, *19*, 3476.
[22] A. Scheele, N. Oeschler, I. Veremchuk, K.-G. Reinsberg, A.-M. Kreuziger, A. Kornowski, J. Broekaert, C. Klinke, H. Weller, *ACS Nano* **2010**, *4*, 4283.
[23] A. Denoix, A. Solaiappan, R. M. Ayral, F. Rouessac, J. C. Tedenac, *J. Solid State Chem.* **2010**, *183*, 1090.
[24] S. Schlecht, C. Erk, M. Yosef, *Inorg. Chem.* **2006**, *45*, 1693.
[25] C. S. Birkel, E. Mugnaioli, T. Gorelik, U. Kolb, M. Panthöfer, W. Tremel, *J. Am. Chem. Soc.* **2010**, *132*, 9881.
[26] G. Kieslich, C. S. Birkel, A. Stewart, U. Kolb, W. Tremel, *Inorg. Chem.* **2011**, *50*, 6938.
[27] JCPDS No. 00-056-0235
[28] M. Boström, S. Lidin, *J. Alloyd Compd.* **2004**, *376*, 49.
[29] JCPDS No. 00-023-1017 (orthorhombic); JCPDS No. 01-089-1969 (rhombohedral)
[30] S.-M. Zhou, N. Li, Y.-Q. Wang, S.-Y. Lou, X.-L. Chen, H.-L. Yuan, L.-S. Liu, P. Wang, *Nanoscale Microscale Thermophys. Eng.* **2011**, *15*, 95.
[31] J. Perkins, *Mater. Sci. Eng.* **1977**, *28*, 167.
[32] V. Izard, M. C. Record, J. C. Tedenac, S. G. Fries, *Calphad* **2001**, *25*, 567.
[33] E. Chalfin, H. X. Lu, R. Dieckmann, *Solid State Ionics* **2007**, *178*, 447.
[34] G. S. Pomrehn, E. S. Toberer, G. J. Snyder, A. van de Walle, *J. Am. Chem. Soc.* **2011**, *133*, 11255.

Chapter 5

Scaled-up Chemical Synthesis of Zn-Sb Nanoparticles and Thermoelectric Properties of Zn-Sb Nanostructured Materials

The large scale syntheses of Zn-Sb nanoparticles (NP)s result in gram amount of NPs for making the pellet and study the thermoelectric properties of the nanostructured bulk materials. The large scale chemical synthesis was investigated with varying the feeding ratio of precursor to obtain the resulting NPs with size of 20.5 - 25.4 nm and compositions of $Zn_{42}Sb_{58}$ to $Zn_{45}Sb_{55}$ similar to that of $Zn_{47}Sb_{53}$ NPs obtained from small scale synthesis. The organic capping molecules on surface of NPs were removed during heat treatment at 366 ^{o}C for 6 h. The pellet made from NPs can be archived *via* hot-pressing at 400 - 500 ^{o}C and 100 MPa for 5 hours with area of 10x10 mm^2 and 1.4 - 2.3 mm in thickness. The thermoelectric properties of the nanostructured sample including thermal conductivity, electrical conductivity and Seebeck coefficient were measured. This study focuses on not only the large synthesis of NPs but also the thermoelectric properties of the three dimensional materials with NPs as the building blocks.

5.1. Introduction

Thermoelectric (TE) materials are interesting for wide range of applications such as cooling devices, electricity generations, especially, waste heat to electricity converter.[1-3] The efficiency of TE materials is determined via *ZT* value, $ZT = \alpha^2\sigma T/\kappa$, where σ is the electrical conductivity, κ is the thermal conductivity and α is the Seebeck coefficient. It is well known that the low efficiency of TE materials is still a big challenge for these applications which required a *ZT* higher than 3.[1] From the fundamental point of view, the difficulty in improving *ZT* value arises from the reverse relation between 3 parameters contributing to *ZT*. Many studies on the field of TE materials are, therefore, devoted to overcome this challenge, or, on another words, decoupling the independence of electrical and thermal conductivity to make a "phonon glass electron transmission" materials.[4-6] Based on the fact that the thermal conductivity are built up from two parts, one from electron carrying heat which always proportional to electrical conductivity as given by Wiedermann-Franz's law and the other one from phonon carrying heat which can be manipulated to minimize κ while not significantly affect on σ. With this in mind, nanostructured thermoelectric materials which offer a large area of grain boundary for phonon scattering and the size dependent properties for separately manipulating electrical and thermal conductivity have been expected to be a potential candidate of TE materials with enhanced *ZT* value.[7-8]

For medium temperature ranges from 200-400 ^{o}C, ZnSb bulk materials exhibit one of the highest *ZT* value.[9-12] With introducing nanostructure to ZnSb materials, the more decrease in κ is expected to further improve the TE performance. The ZnSb nanoparticles (NP)s with controllable properties and characteristics, however, is still challenging for researcher all over the world and only few studies succeeded in the chemical approaches to synthesize this compound even though they could not fully manipulate the NPs characteristics.[13-16] In previous chapter, a multiple step chemical reaction is demonstrated to successfully synthesize Zn-Sb NPs.[17] The resulting NPs exhibit interesting characteristics with size of about 23 nm, narrow size distribution, and composition nearly $Zn_{50}Sb_{50}$ as well as the complex structure where Sb and Zn distribute in a single NP with a composition gradient of Zn and Sb along the radial direction of NPs with Zn rich at the shell and Sb rich in the core.[17] The multiphases of ZnSb may exist in the NPs and further annealing are expected to obtain homogenous phase.

Improvement of the TE properties can be achieved by using ZnSb NPs as the bulding blocks of TE materials. Towards the final target, the large scale reaction, create nanostructured

materials and optimize the composition are all required even though it is hugely challenging for NPs obtained by solution synthesis. Base on the synthesis approach developed in the previous chapter, this study focus on scaling up the chemical synthesis, adjust the composition and homogeneity with further thermal annealing during pelletizing NP powder (by means of hot pressing) and finally investigation of the TE properties of nanostructured pellet.

5.2. Experimental Section

5.2.1. Chemicals

$ZnCl_2$ (purity 98%), $SbCl_3$ (purity 99%), phenyl ether (PhE, purity 99%), oleylamine (OAM, purity 70%) and lithium triethylborohydride ($LiBHEt_3$, 1M solution in tetrahydrofuran, THF) were purchased from Sigma Aldrich and used without further purification. Other common solvents were purchased from Kanto Chemical and used as received.

5.2.2. Large scale synthesis of Zn-Sb NPs

The synthesis was carried out in a 4-neck flask under an Ar atmosphere. 8 mmol of $SbCl_3$ and 48 mmol of OAM were put in 100 ml of PhE and heated up to 60 °C under stirring (stock solution I). Separately, 8 mmol of $ZnCl_2$ and 32 mmol of OAM were put in 100 mL of PhE and heated up to 200 °C (stock solution II). 24 mL of $LiBHEt_3$ and 800 ml of PhE were put into the flask and heated up to 250 °C under Ar (matrix solution). Then, 100 mL of stock solution I was rapidly injected into the matrix solution. The color of the reaction solution turned to black immediately after the injection. After 30 min of the reaction at 250 °C, the temperature of the reaction solution was quickly reduced to 200 °C. Subsequently, 100 mL of stock solution II preheated at 200 °C was injected into the reaction solution followed by the injection of 16 mL of $LiBHEt_3$. The reaction was continued for 1 hour at 200 °C to obtain the Zn-Sb NPs dispersion (Fig. 5.1). After that the reaction solution was quickly cooled to room temperature, and then ethanol was added to the reaction solution for the natural precipitation of NPs. This purification process was repeated 5 times to obtain the final product. In case of the sampling to take out small amount of NPs, centrifugations were utilized to separate NPs from the matrix solution.

Figure 5.1. Photograph of the reactor after 1 hour of reaction with the black dispersion of the resulting NPs in di-phenylether. The reaction solution volume is of about 1070 mL.

5.2.3. Making the nanostructured pellet

Thermal treatment

After purification, the resulting NPs were put into the quartz boat in the tube furnace to be underwent the thermal treatment under N_2 gas with flow rate of 50 mL/min for 6 hours at 366 ^oC to remove oleylamine left on the surface of NPs.

Then, the pellet was prepared either by means of cool pressing and sintering or hot pressing techniques. For the cool pressing, refer to the results of the subtheme research.

Hot pressing

After the thermal treatment, NPs was introduced into the pressing holder of the hot pressing machine. The sample chamber was vacuumed to the vacuum level of $2x10^{-4}$ Torr to remove the air. After that, the Ar gas was flowed into the chamber with flowing rate of 1 $Lmin^{-1}$. The sample was pressed at 100 MPa at elevated temperature ranging from 400 ^oC to 500 ^oC for 5 hours under Ar gas (heating rate of 6.5 $^oCmin^{-1}$). The pressure was fine adjusted to keep constant during the time of hot-pressing. After 5 hours of the hot-pressing, the sample was naturally cooled down to room temperature, then, the pressure was released.

The pellet after the hot-pressing was underwent the surface polishing and was cut in specific configuration for further analysis and measurement of thermoelectric properties.

5.2.4. Instrumentation and analysis conditions

X-ray diffraction and X-ray photoelectron spectroscopy

X-ray diffraction (XRD) patterns of NPs were collected in reflection geometry using a Rigaku SmartLab X-ray diffractometer at room temperature with Cu Kα radiation (X-ray wavelength of 1.5418 Å).

For X-ray photoelectron spectroscopy (XPS), the dried NPs were put on carbon tape and measurements were performed on a Shimadzu Kratos AXIS-ULTRA DLD high performance XPS system. Photoelectron was excited by monochromated Al Kα radiation. Detection was done with a delay-line detector (DLD) and a concentric hemispherical analyzer (CHA). The pass energy of the CHA was 20 eV for narrow-scan spectra. The analyzed area on the specimen surface was 300×700 μm^2 and was located in the center of the irradiated region.

Transmission Electron Microscope (TEM)

As-synthesized NPs and NPs after annealing were re-dispersed in ethanol with the addition of OAM. 10 μL of the NP dispersion was dropped onto a carbon-coated TEM grid and completely dried under ambient conditions. TEM for NPs was performed on a Hitachi H-7650 and H-9000. High-angle annular dark-field scanning TEM (HAADF-STEM) imaging and energy dispersive X-ray spectroscopy (EDS) elemental mapping were carried out for nanostructured pellets using a JEOL JEM-ARM200F instrument operated at 200 kV.

Inductively couple plasma optical emission spectroscopy (ICP-OES)

Samples for ICP-OES were prepared by dissolving NPs in aqua regia then were diluted using Mili Q water. The data were collected using a Shimazu Sequential Plasma Spectrometer ICPS-7000.

DT/TGA measurement

TG/DTG measurement of the dried NP powder was conducted using a Seiko TG/DTA6200 with heating rate 10 °Cmin^{-1} under N_2 gas with flow rate of 200 $mLmin^{-1}$.

Thermoelectric property measurement

The thermal conductivity, κ, was measured by laser flash method on a TC-7000 (ULVAC-RIKO Inc.). The electrical conductivity, σ, and Seebeck coefficient, α, of the resulting pellet were measured on a ZEM-1 (ULVAC-RIKO Inc.).

5.3. Results and Discussion

5.3.1. Large scale chemical synthesis of Zn-Sb NPs

The purpose of this part is to scale up the synthesis developed in chapter 4 to obtain the larger amount of Zn-Sb NPs with similar structure and morphology enough for making the pellet and study the TE properties. The large scale syntheses were first conducted with the feeding ratio of Zn:Sb = 50:50 as the same as the synthesis presented in chapter 4. However, the resulting NPs show a composition of $Zn_{39}Sb_{61}$ (measured by XPS) and $Zn_{30}Sb_{70}$ (measured by ICP-OES) (Table 5.1) which is far from the composition of $Zn_{47}Sb_{53}$ obtained for NPs in small scale synthesis (chapter 4).[17] Therefore, it is necessary to increase the feeding ratio of $ZnCl_2$ in the synthesis. In the following part, the syntheses were conducted with the molar feeding ratio of Zn:Sb equal to 50:50, 66:34, 58:42 and 58:42 followed by the addition of Zn NPs respectively. The resulting NPs from those syntheses were labelled by Sample I, II, III, IV respectively and collected for the characterizations.

Morphology of NPs

The as-synthesized NPs (before annealing) were investigated for the the morphology, composition, crsytal structure and oxidation state. Fig. 5.2 shows the TEM images of Sb NPs (Fig. 5.2A) sampled before injection of Zn stock solution, Zn-Sb NPs with molar feeding ratio of Zn:Sb equal to 50:50 (Sample I, Fig. 5.2B), 67:33 (Sample II, Fig. 5.2C), 58:42 (Sample III, Fig. 5.2D-F) and 58:42 followed by the addition of Zn NPs (Sample, IV, Fig. 5.2G-I) respectively. The addition of Zn NPs is to adjust the average composition of the pellet prepared by hot pressing and it is found effectively suppress antiony oxide formation. The Sb NPs are aggregated in the TEM image, and the segregated Sb NPs have roughly round shape. The mean crystalline size calculated from the XRD peak based on the Scherrer formula for Sb NPs is of 21.3 nm. The aggregation of NPs observed in the TEM image is due to the fact that the NPs were separated from the matrix solution by means of the centrifugation prior to the preparation of the TEM sample. Zn-Sb NPs prepared using different elemental feeding ratio of $ZnCl_2$ and $SbCl_3$ were shown in Fig. 5.2B-I. The average size of resulting NPs were listed in Table 5.1 for the syntheses using different feeding ratio which ranges from 21 ± 4 to 31 ± 5 nm. However,

in comparison to the small scale synthesis (chapter 4),[17] the morphology of Zn-Sb NPs in large scale synthesis shows less uniform in size and shape. The most similar morphology of Zn-Sb NPs were obtained in cases of Sample III and IV synthesized using feeding ratio Zn:Sb = 58:42 with and without addition of Zn NPs respectively.

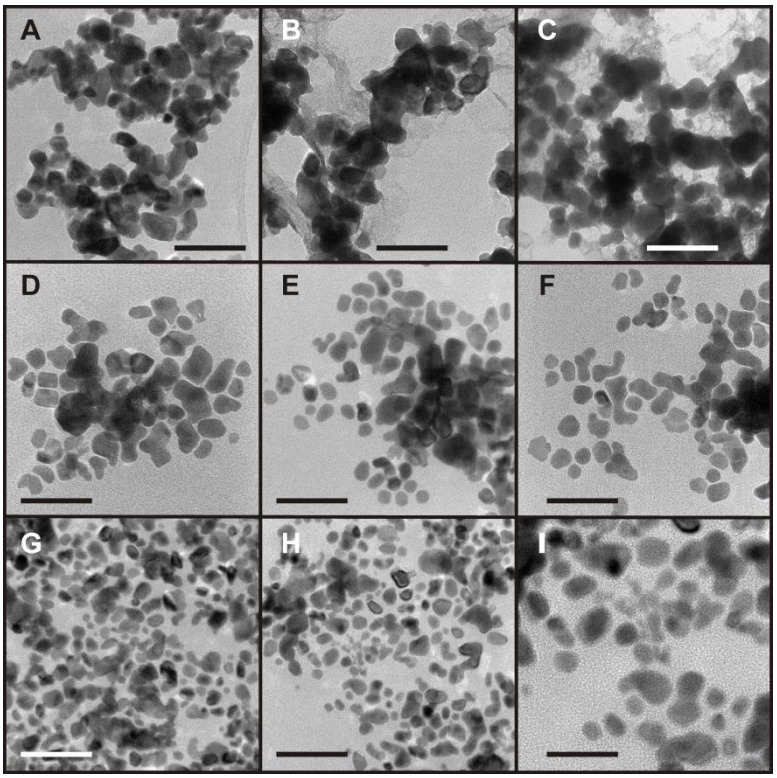

Figure 5.2. TEM images of (A) Sb seed NPs and (B-I) Zn-Sb NPs synthesized using different molar feeding ratios of Zn to Sb precursors: (B) 50:50 (Sample I), (C) 67:33 (Sample II), (D-F) 58:42 (Sample III), (G-I) 58:42 followed by the addition of Zn NPs (Sample IV). The scale bar in fig 5.2I is 50 nm and all other scale bars are 100 nm. It is noted that the Sb seed shown in Fig. 5.2 is sampled from the synthesis using feeding ratio of Zn:Sb equal to 50:50.

It is interesting that, among all the cases, the NPs displaying the core-shell like structure (constrast between the center and periphery of the NPs) (Fig. 5.2I) as it was observed in small scale synthesis (chapter 4) are only founded for Sample IV when the feeding ratio of Zn:Sb equal to 58:42 was used followed by addtion of the Zn NPs.[17] Moreover, from the XRD peaks of Sb NPs and Zn-Sb NPs (Fig. 5.3, Table 5.1), the mean crystalline sizes of the Zn-Sb NPs in

all cases (20.1 to 23.6 nm) are close to that of the Sb NPs (21.3 nm) and also in good agreement with the size calculated from the TEM images.

Table 5.1 Summary of the composition, phases and sizes for the as-synthesized Zn-Sb NPs using different molar feeding ratios of the metal precursors

ID	Feeding ratio $ZnCl_2$:$SbCl_3$	XPS	ICP-OES	Phases	D_{TEM} [nm]	D_{XRD} [nm]
	$SbCl_3$ only	NA	NA	Sb	25 ± 6	21.3
Sample I	50:50	$Zn_{39}Sb_{61}$	$Zn_{30}Sb_{70}$	Sb/ZnSb	30 ± 2	23.6
Sample II	67:33	$Zn_{83}Sb_{17}$	$Zn_{90}Sb_{10}$	ZnSb, Zn, Sb_2O_3, ZnO	31 ± 5	22.4
Sample III	58:42	$Zn_{58}Sb_{42}$	$Zn_{42}Sb_{58}$	ZnSb, Zn Sb_2O_3	25 ± 4	23.6
Sample IV	58:42, addition of Zn NPs	$Zn_{64}Sb_{36}$	$Zn_{45}Sb_{55}$	ZnSb, Zn	21 ± 4	20.1

DTEM and DXRD represent for the size measured by TEM and crystallite size calculated from Scherrer's formula

Composition of NPs

The composition of the resulting NPs was measured using XPS, and ICP-OES. In all cases, both Zn and Sb were found; however, the composition indicated by each analytical method is different from each other. The composition measured by XPS is higher than that measure by ICP-OES. This tendency was observed in samples synthesized with feeding ratios of Zn:Sb equal to 50:50, 67:33, and 58:42. It can be explained because of the fact that the NPs may possess the inhomogeneous composition from the surface to the center and XPS only gives the composition of the surface region while ICP-OES measures the average composition of the sample after the NPs were completely dissolved in acid solution. Detail of the composition of each sample was shown in Table 5.1. The average composition of Zn and Sb (measured by ICP-OES) in the resulting NPs can be tuned by varying the input feeding ratio. NPs with average composition of $Zn_{30}Sb_{70}$, $Zn_{90}Sb_{10}$, $Zn_{42}Sb_{58}$ can be obtained from the feeding ratios of Zn:Sb equal to 50:50, 66:34 and 58:42. Using the feeding ratio of Zn:Sb equal to 58:42 followed by the addition of Zn NPs results in a little increase of Zn content in the resulting NPs

in Sample IV ($Zn_{45}Sb_{55}$, measured by ICP-OES) (noted that the Zn NPs were synthesized with the calculated feeding ratio to obtain $Zn_{58}Sb_{42}$ composition). In term of average composition, the last two samples (Sample III and IV) synthesized using input molar ratio of Zn:Sb equal to 58:42 with and without addition of Zn NPs show the most similar composition to that of Zn-Sb NPs obtained in small scale synthesis ($Zn_{47}Sb_{53}$).

Crystal structure and phases: X-ray diffraction

The crystal structure of the resulting NPs was analyzed using X-ray diffraction. The results were plotted in Fig. 5.3. For Sample I (equal feeding ratio of Zn to Sb), monometallic Zn or ZnO and/or antimony oxides could not found in the XRD pattern (Fig. 5.3A). All the peaks can be well fit with ZnSb hexagonal structure (JCPDS card no. 00-018-0140) as shown in the reference pattern in Fig 5.3. Because of the similarity of crystal structure of Sb (rhombohedral structure) and ZnSb (hexagonal structure) as well as the NPs are rich in Sb (ICP-OES composition of $Zn_{30}Sb_{70}$), it is possible for the existence of Sb phase in the final product. It is also possible that the NPs contain hexagonal Sb and the Zn element exists in amorphous phase which can be detected in the composition analysis methods while does not contribute to the XRD pattern. However combination of the XRD analysis and the average composition of the sample, it suggests that whatever the case, the phase ZnSb can only present with small portion compared to Sb phase.

Using excess amount of $ZnCl_2$ with the feeding ratio of Zn:Sb = 66:34 for the synthesis, the XRD pattern of the resulting NPs (Sample II, Fig. 5.3B) clearly shows the crystalline peak of Zn (at 36.29, 38.66, 43.24), ZnO (at 31.45, 33.76, and 36.29), Sb_2O_3 (at 27.18, 45.26, 53.93 in 2θ) and the other peaks are identical with XRD pattern of Fig. 5.3A which can be assigned for either Sb rhombohedral or ZnSb hexagonal structure. It is important that the Zn peaks are strong in this case which is in agreement with the composition analysis results (ICP-OES composition of $Zn_{90}Sb_{10}$). These results indicate that the high feeding ratio of Zn:Sb equal to 66:34 is fail in produce $Zn_{47}Sb_{53}$ NPs(obtained in chapter 4). This result may arise from the limitation diffusion of Zn into Sb, hence, the outside Zn shell or segregated Zn (due to the homogenous nucleation and growth become more dominant) are oxidized without alloying with Sb.

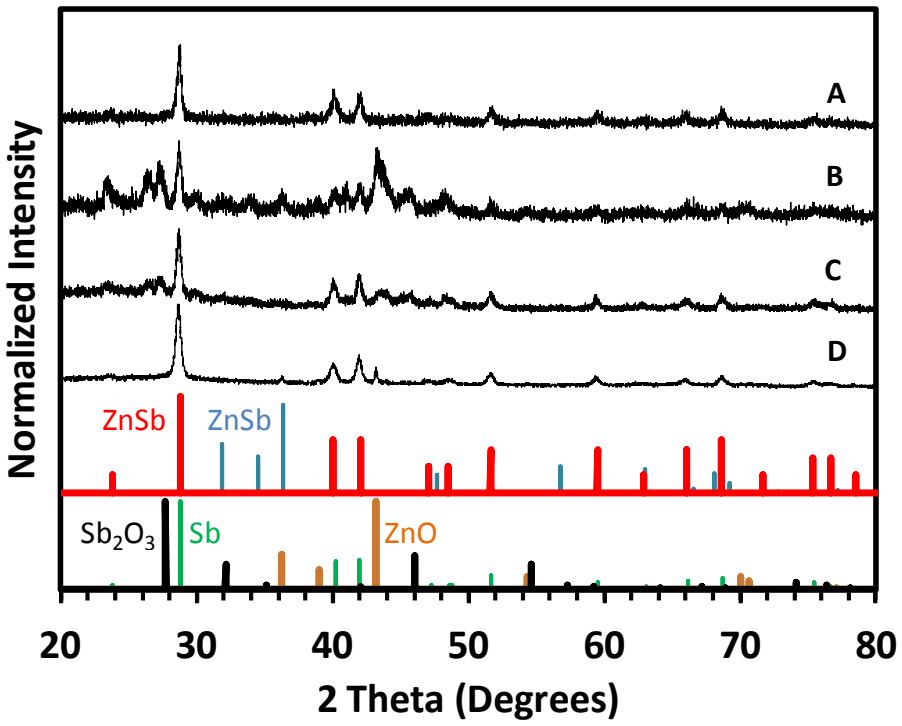

Figure 5.3. XRD pattern of the as-synthesized Zn-Sb NPs using different molar feeding ratios of Zn to Sb precursors equal to 50:50 (A), 67: 33 (B), 58:42 (C), and Zn to Sb precursors equal to 58:42 followed by the addition of Zn NPs (D). The references of ZnSb (hexagonal, JSPS card No.00-018-0140, Sb (rhombohedral, JSPS card No. 01-085-1324), Zn (hexagonal, JCPDS No.03-065-5973), ZnO (hexagonal, JSPS card No. 01-075-0576), Sb_2O_3 (cubic structure, JCPDS No. 01-075-1565) were labeled by red, green, orange, blue and black colors.

Based on those two cases, it is worthy that the input molar ratio of $ZnCl_2$ to $SbCl_3$ should not be far from 1 to avoid the oxidation of Zn as well as the dominant formation of Zn. Using the feeding ratio of Zn:Sb equal to 58:42 results in NPs (Sample III) with average composition of $Zn_{42}Sb_{58}$ (measured by ICP-OES) which is closer to the equal composition of Zn and Sb. The XRD pattern of this sample is shown in Fig. 5.3C. Zn and Sb_2O_3 were found to be very minor phases in which the peak appear at 43.24 may come from Zn and peaks at 27.18 and 45.26 in 2θ come from Sb_2O_3. The all other main peaks can be assigned for either ZnSb hexagonal or Sb rhombohedral structure.

Because the NPs will undergo the hot pressing at high temperature (400-500 ^oC) and pressure (100 MPs) to form the pellet, Zn NPs were added to resulting Zn-Sb NPs dispersion to increase the average content of Zn in the final product. For that purpose, the synthesis using

feeding ratio of Zn:Sb equal to 58:42 were conducted, then Zn NPs were separately synthesized and added into the reaction solution of Zn-Sb NPs for mixing with Zn-Sb NPs in the solution. It is interesting that the final product have the average composition of $Zn_{45}Sb_{55}$ (Table 5.1) and the morphology similar to the Zn-Sb NPs in the small scale synthesis (Fig. 5.2I). The XRD pattern of the final product (Fig. 5.3D) shows that there are no zinc oxide and antimony oxides' peaks. The minor peaks at 36.29, 38.66, and 43.24 in 2θ are identical with hexagonal structure Zn while all the other main peaks were assigned for either ZnSb or Sb phases.

Surface properties: X-ray photoelectron spectroscopy

Further analyze the chemical state and surface properties of Zn-Sb NPs, XPS were carried out on Sample III and IV with composition of $Zn_{42}Sb_{58}$ and $Zn_{45}Sb_{55}$ and the results were plotted in Fig. 5.4.

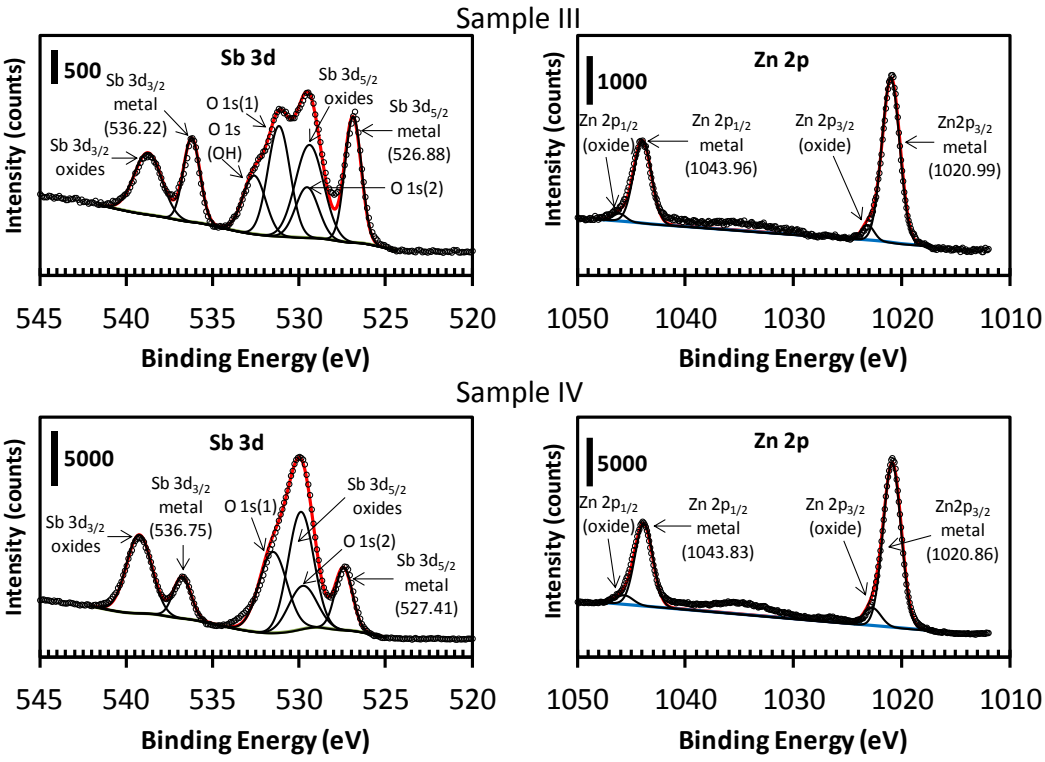

Figure 5.4. XPS spectra of resulting NPs from Sample III with composition of $Zn_{42}Sb_{58}$ (upper row) and Sample IV with composition of $Zn_{45}Sb_{55}$ NPs (lower row): the narrow scan areas of Sb 3d and Zn 2p. For more explanation of the O peaks, refer to the Appendix IV.

The XPS spectrum of Sb 3d area shows both Sb metal and oxides. It is also notable that the XPS narrow scanning spectrum of Sb3d area is overlapped with O 1s area, the deconvolution is necessary to identify Sb 3d peaks and O 1s peak. The oxide peaks found in XPS spectra may originate from the surface oxidation when the sample exposed to the air (XPS technique is surface sensitive). The XPS spectrum of Zn area exhibits mostly Zn metal compared to ZnO. It is noticed that Zn it shelf is reactive metal and easy to be oxidized. Therefore, the enhancement of oxidation of Zn may indicate the alloy formation between Zn and Sb, which can stabilize both Zn and Sb. The similar results were reported for $Zn_{47}Sb_{53}$ NPs[17] synthesized under similar conditions and method in a small scale synthesis. Therefore, combine all results, it is thought that in the large scale synthesis, Zn-Sb NPs which rich in Sb can be formed, and the composition gradient along NPs radius still exists. The two last samples with composition, morphology and structure similar to the reported $Zn_{47}Sb_{53}$ NPs[17] in the small scale synthesis (chapter 4) were used to create the pellets *via* hot-pressing and study their thermoelectric properties.

5.3.2. Zn-Sb NPs after thermal treatment

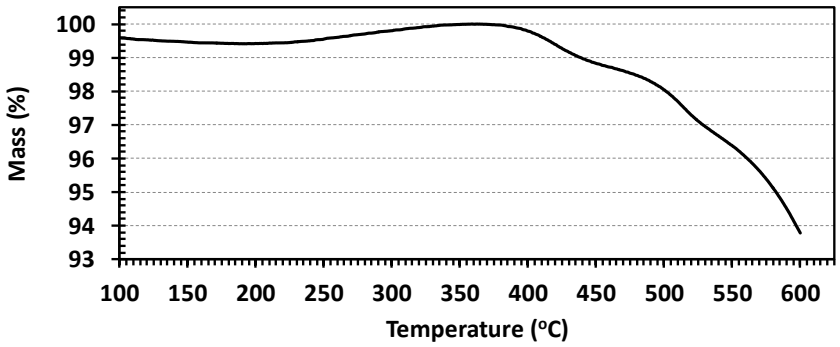

Figure 5.5. TGA curve for the Zn-Sb NPs after 6 hours annealing at 366 °C.

The surface of NPs is stabilized with OAM (even after purification) which are organic capping molecules with long alkyl chain. The existence of OAM with very low electrical conductivity can affect (decrease) not only the density of the sample but also the electrical contact between NPs. Therefore, to characterize the intrinsic TE properties of the pellet, all organic capping molecules should be removed before the measurement. For this purpose, a thermal treatment was carried out at 366 °C (close to the boiling point of OAM, 364 °C) for 6

hours under the flowing of reducing gas (10 % H_2 in Ar). The TG/DTA analysis shows that after 6 hours of annealing at 366 ^oC, the decrease of mass is less than 1 % (under error) until 420 ^oC (melting point of Zn) which confirms that OAM can be mostly removed (Fig. 5.5).

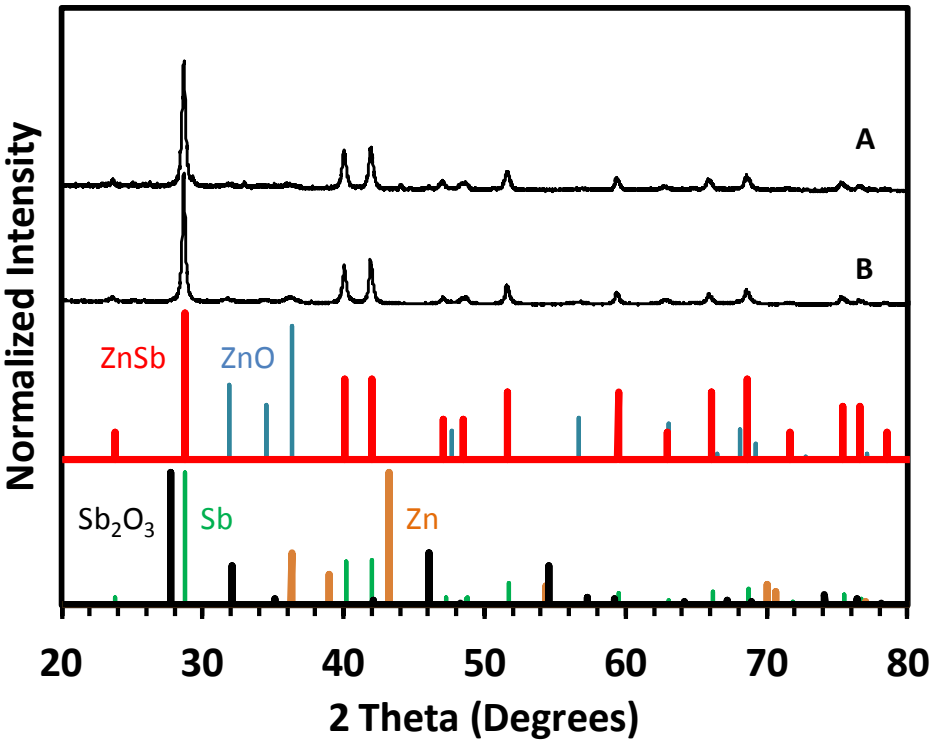

Figure 5.6. XRD pattern of Zn-Sb NPs after thermal annealing for Sample III (A) and IV (B). The references of ZnSb (hexagonal, JSPS card No.00-018-0140, Sb (rhombohedral, JSPS card No. 01-085-1324), Zn (hexagonal, JCPDS No.03-065-5973), ZnO (hexagonal, JSPS card No. 01-075-0576), Sb_2O_3 (cubic structure, JCPDS No. 01-075-1565) were labeled by red, green, orange, blue and black colors.

The XRD patterns of the sample after annealing were collected in Fig. 5.6 to check the crystal structure and phases. In both cases the crystalline sizes of 31.8 nm and 43.2 nm for Sample III and IV (with elemental composition of $Zn_{42}Sb_{58}$ and $Zn_{45}Sb_{55}$ respectively) were increases compared to the as-synthesized NPs. There is no sign for metallic Zn phase appear in both XRD patterns, however, there are some peaks of ZnO at the position 31.45, 33.76, and 36.29 in 2θ in case of $Zn_{45}Sb_{55}$ sample. Sb_2O_3 peaks were not found in Sample III compared to the as-synthesized NPs which can be explained due to the fact that Zn and H_2 gas can act as the reducing agent to reduce Sb_2O_3 to Sb at elevated temperature. However, the reducing gas

is not significant protect Zn, so the ZnO once it is formed could not be reduced back to Zn. The flowing of reducing gas before the heat treatment may not completely remove the gas and water molecules adsorbed on the surface of NPs, which can be one of the reasons for the oxygen sources. It is noted that metallic Zn was found in the XPS spectrum of both samples (Appendix V, Fig. A5.1) even though Zn peaks do not appear in XRD pattern. This phenomenon may due to the further diffusion of Zn into Sb and the formation of Zn-Sb phase.

5.3.3. Zn-Sb pellet after hot pressing

The composition and structure and bulk properties of pellets were summarized in Table 5.2.

Table 5.2 Summary of the composition of Zn-Sb NPs and pellet and the bulk properties of the pellets

Sample	Composition measured by XPS (up) and ICP-OES (down)			Pellet		
	NPs before annealing	NPs after annealing	Pellet	Phases	D_{XRD} [nm]	Density (%)
Sample III	$Zn_{58}Sb_{42}$ $Zn_{42}Sb_{58}$	$Zn_{65}Sb_{35}$ N/A	$Zn_{30}Sb_{70}$ $Zn_{40}Sb_{60}$	ZnSb, ZnO	28	85.3
Sample IV	$Zn_{64}Sb_{36}$ $Zn_{45}Sb_{55}$	$Zn_{64}Sb_{36}$ $Zn_{42}Sb_{58}$	$Zn_{34}Sb_{66}$ $Zn_{41}Sb_{59}$	ZnSb, ZnO	56	71.4

Sample III. The pellet after pressing (the inset of Fig. 5.7) has area of 10x10 mm^2, height of 2.36 mm and density of 5.4 gcm^{-3} which is 85.3% compared to the theoretical value (6.33 gcm^{-3}) of $Zn_{50}Sb_{50}$ bulk materials (it is noted that the resulting NPs are rich in Sb ($Zn_{42}Sb_{58}$), and the molecular weight of Sb is higher than Zn which can contribute to the lower density of the prepared pellet in comparison to bulk $Zn_{50}Sb_{50}$).

The pellet show almost identical crystal structure with the NPs after thermal treatment (Fig. 5.7A) except for some minor peaks of ZnO at 31.45, 33.76, and 36.29 in 2θ (marked by blue arrows). The average surface composition calculated from the XPS spectra of this sample is $Zn_{30}Sb_{70}$ (Appendix V, Fig. A5.2). However, the XPS composition shows less Zn than the ICP composition because of the inhomogeneity of the microstructure and composition

distribution in the pellet which might be the same as observed for the pellet made from Sample IV in the mapping images (Fig. 5.8).

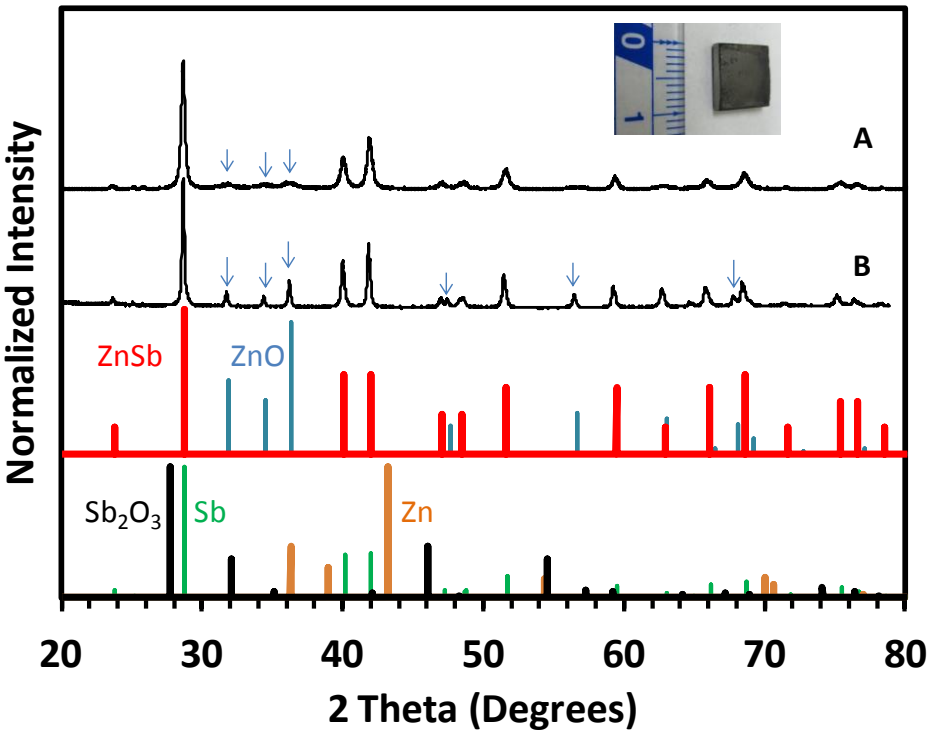

Figure 5.7. XRD pattern of Zn-Sb pellets after hot pressing of Sample III (A) and IV (B). The references of ZnSb (hexagonal, JSPS card No.00-018-0140, Sb (rhombohedral, JSPS card No. 01-085-1324), Zn (hexagonal, JCPDS No.03-065-5973), ZnO (hexagonal, JSPS card No. 01-075-0576), Sb_2O_3 (cubic structure, JCPDS No. 01-075-1565) were labeled by red, green, orange, blue and black colors. The inset shows the picture of the pellet prepared from Sample III with the ruler scale unit of 1 cm.

Sample IV. The pellet after pressing and polishing (not show) has area of 10x10 mm^2, height of 1.43 mm and density of 4.52 gcm^{-3} which is 71.4 % compared to the theoretical value (6.33 gcm^{-3}) of $Zn_{50}Sb_{50}$ bulk materials (again it is noticed that the resulting pellet is rich in Sb ($Zn_{41}Sb_{59}$), with the molecular weight of Sb higher than that of Zn, and contains ZnO with bulk density of 5.6 gcm^{-3}).

This pellet also displays the same crystal structure with that of the NPs after heat treatment, but the ZnO peaks appear more clearly in the XRD pattern (marked by blue arrows in Fig. 5.7B).

The average surface composition calculated from the XPS spectra of this sample is $Zn_{34}Sb_{66}$ which is similar to that of the pellet prepared from Sample III (Appendix V, Fig. A5.2).

In both cases, the mean crystalline size of the sample is of 56 nm for pellet prepared from Sample III and 28 nm for pellet prepared from Sample IV, which may suggest that the nanostructure may be maintained at certain extent and these samples have large area of grain boundary. The existence of the nanostructures in the pellet can be comfirmed by TEM image for pellet prepared using sample IV (Fig. 5.8) where grain size less than 100 nm were found.

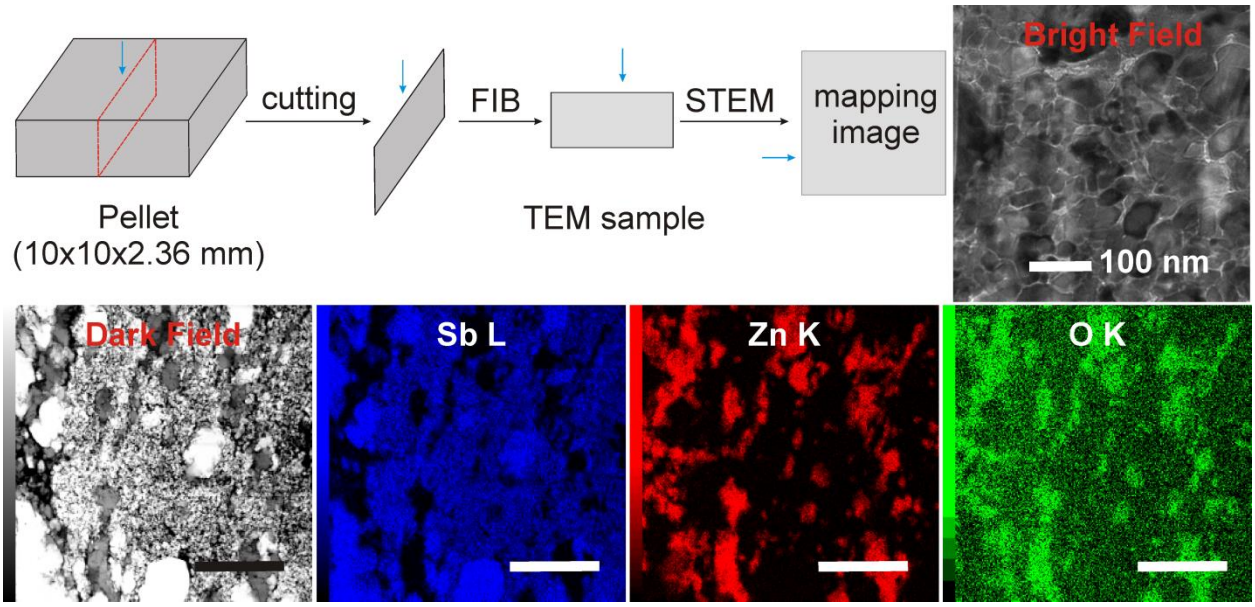

Figure 5.8. Upper row: TEM sample preparation from the pellet in which FIB stands for focus ion beam, the technique used to prepare thin film sample for TEM observation; the blue arrows indicate the position from the surface of the pellet; and the TEM image shows small grain size in the pellet. Lower row: dark field (HAADF) image and elemental mapping images for Sb L, Zn K, O K. All scale bars in HAADF and mapping images are 100 micrometer.

The structure and composition distribution for pellet prepared from sample IV with composition of $Zn_{41}Sb_{59}$ were analyzed using HAADF-STEM and EDS mapping. The results

shown in Fig. 5.8 indicate that both Zn and Sb exist in the sample, but segregated from each other to in different areas, with dark color for Sb and lighter for Zn in the dark field image. The elemental mapping images further indicate that oxygen exists in the same area with Zn rather than Sb which is consistent with the existence of ZnO and Sb. The EDS results for Zn area and Sb area (Appendix V, Fig. A5.3) are also consistent with the results indicated in elemental mapping images. But, it is noted that, Zd and Sb are not completely segregated and ZnSb phases can exist in the pellet, where both Zn and Sb were found (Fig. 5.8 and Appendix V, Fig. A5.4). The TEM image (Fig. 5.8) also indicates that the pellet contains space between nanoparticles which contributed to the low density of the sample.

In summary, the pellet display Sb/ZnSb and ZnO segregated phases especially near the surface. The pellet contains the large (in order of micron) and small (hundred nanometer) grain sizes with porosity exist in the sample. Even though the optimal Zn-Sb phases were not found as the pure phase in the pellet, the maintain of small grain size under the pressing condition is important for further using of NPs as the building block for the nanostructured TE materials. The following investigation of the TE properties of pellet is necessary to understand relation of the structure, composition and TE properties which will help further progress in this field.

5.3.4. Thermoelectric properties of the Zn-Sb nanostructured pellet

Sample III Pellet

After the hot pressing at 100 MPa and 400 ^{o}C for 5 hours, the pellet was used to measure the thermoelectric properties. The results were shown in Fig. 5.9. The temperature dependence of the pellet's resistivity was plotted in Fig. 5.9A. The result shows the decreasing of ρ with increasing of temperature ($d\rho/dT<0$) for the measurement temperature range from near room temperature to 250 ^{o}C. This temperature dependence tendency is good indication of the semiconductor like behavior of the pellet. The resistivity of 0.32-0.37 mΩ.m for Zn-Sb pellet which is 4 order larger than the value of Zn (metal, $6x10^{-5}$ mΩ.m) and 3 order higher than that of Sb (semimetal, $40x10^{-5}$ mΩ.m) furthermore suggests that the Zn-Sb pellet is a semiconductor. The large value of ρ is also consistent with the analytical result for the composition of the pellet ($Zn_{40}Sb_{60}$) which is not $Zn_{50}Sb_{50}$.[22] We also do not rule out the partial contribution of the low density of the sample (less than 85.3% of the theoretical value) and the antimony and zinc oxides to the high value of ρ.

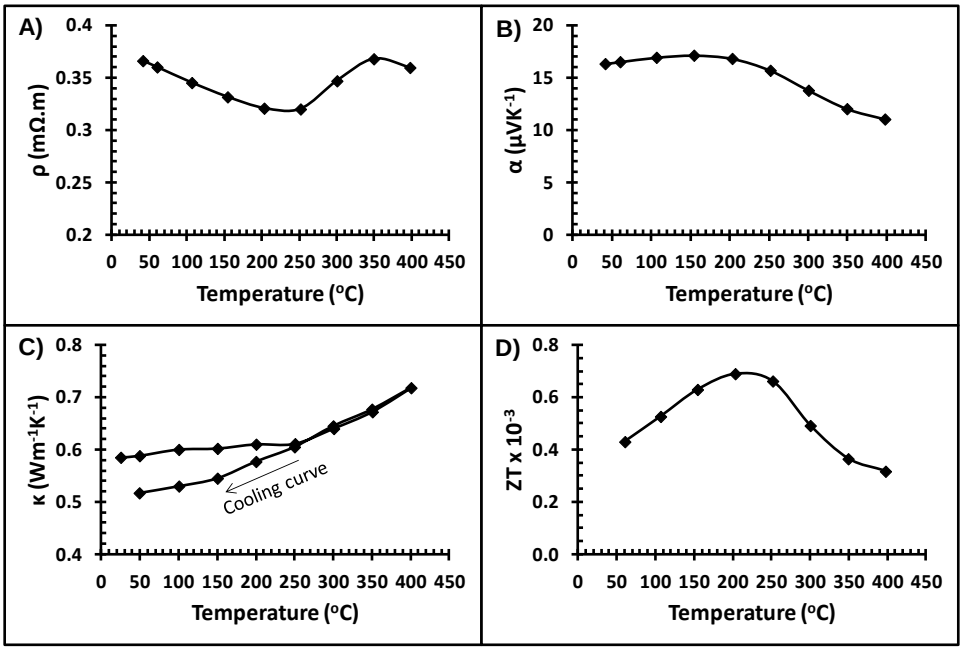

Figure 5.9. Temperature dependence of the thermoelectric properties of Zn-Sb nanostructured pellet prepared from Sample III: (A) electrical conductivity, (B) Seebeck coefficient, (C) thermal conductivity and (D) the dimensionless thermoelectric figure of merit.

Seebeck coefficient versus temperature (Fig. 5.9B) is nearly constant from near room temperature to 200 ^{o}C then decreases as the temperature increases. It can be explained due to the increase of carrier concentration due to the increases of temperature. The positive sign of Seebeck coefficient over the entire measured temperature range indicates of the p-type conduction with holes as the dominant carrier in the sample. The value of α is of about 17 μVK^{-1} from near room temperature to 200 ^{o}C which is larger than the Seebeck coefficient of Zn (2.5 μVK^{-1})[18] but in the same order with the Seebeck coefficient of Sb (~24 μVK^{-1}).[19]

Thermal conductivity as function of temperature was plotted in Fig. 5.9C. κ slightly increases along temperature range from near room temperature to 250 ^{o}C, then increases more significantly when the temperature rises up to 400 ^{o}C. Additionally, it is possibility that the small value of κ (~0.5-0.6 $WK^{-1}m^{-1}$ at near room temperature to 250 ^{o}C) can be contributed partly by the low density of the sample. The κ versus T curve indicates the phonon scattering by grain boundary. The huge amount of grain boundary can be offered by the nanostructure still maintained in the pellet.

Sample IV pellet

After the hot pressing at 100 MPa and 500 ^{o}C for 5 hours, the pellet was used to measure the thermoelectric properties on a ZEM and Laser flash. The results were shown in Fig. 5.10. The temperature dependence of the thermal conductivity, electrical resistivity and Seebeck coefficient of the pellet does not show any significant different in the cooling curve and heating curve, which indicates the stability of the sample and its homogenous thermal expansion.

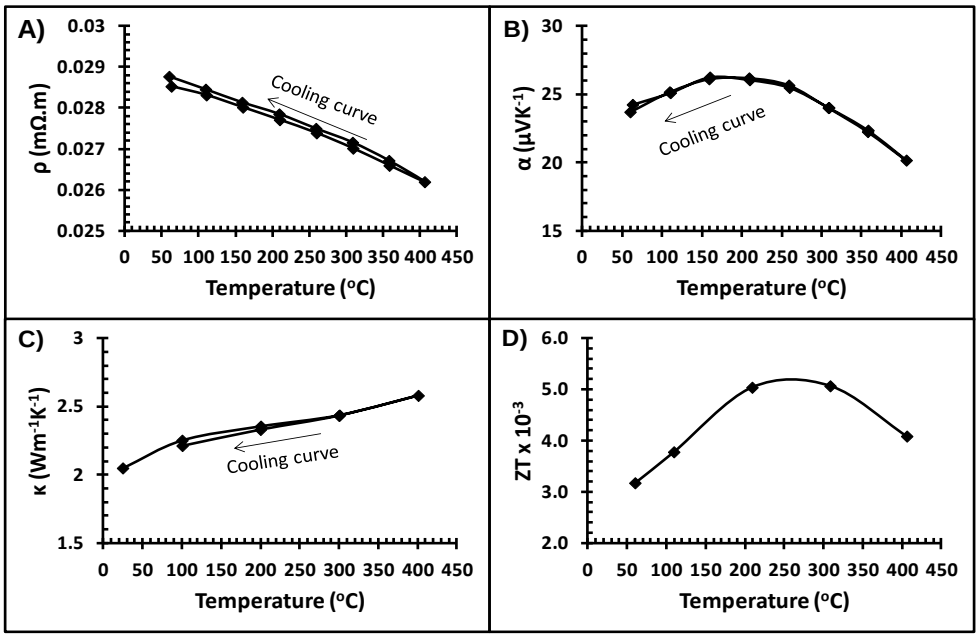

Figure 5.10. Temperature dependence of the thermoelectric properties of Zn-Sb nanostructured pellet prepared from Sample IV: (A) electrical conductivity, (B) Seebeck coefficient, (C) thermal conductivity and (D) the dimensionless thermoelectric figure of merit.

Fig. 5.10A is the temperature dependence of the pellet's resistivity in which the decrease of ρ along with the increasing of temperature ($d\rho/dT<0$) for the entire measurement temperature range exhibits the semiconductor like behavior of the pellet. The resistivity of 0.026-0.029 mΩ.m which is 3 order larger than the value of Zn (metal, $6x10^{-5}$ mΩ.m) and 2 order higher than that of Sb (semimetal, $40x10^{-5}$ mΩ.m) also suggests that the Zn-Sb pellet is a semiconductor. When compared to the case of $Zn_{42}Sb_{58}$ sample without addition of Zn NPs, the resistivity of this sample is much smaller even its density is lower than that of the former one. Additionally, in Sample IV pellet, the content of zinc oxides may be larger than that in Sample III pellet (the XRD peaks of ZnO in Sample IV pellet are clear with higher relative

intensity than that of Sample III pellet. Therefore, it is possible that the electrical contact between NPs in this case was improved due to the higher temperature (500 ^{o}C) during the hot pressing process. It is reasonable because the increase of the thermal conductivity of 3 times compared to that of Sample III pellet also observed for the entire measured temperature range.

The Seebeck coefficient (Fig. 5.10B) is positive in entire measurement temperature range which again indicates the p-type conduction with hole as the dominant carrier in the sample. Moreover α is found to decrease with increasing of the measurement temperature. Combination with the increase of thermal conductivity as well as the decrease of electrical conductivity along with increasing of measurement temperature, those tendencies of α, κ, and ρ can originate from the increase of carrier concentration of semiconductor due to the increasing of temperature. The value of Seebeck coefficient is higher than 20 μVK^{-1} and reaches the maximum value of 26 μVK^{-1} at 150 ^{o}C. Even the Seebeck coefficient is improved compared to that of the Sample III pellet, it is still similar to that of Sb (~24 μVK^{-1}).[19]

The overall zT is very small (~ 10^{-3}) but was improved one order compared to that of Sample III pellet mainly due to the improvement of the electrical conductivity in compensation with the increase of thermal conductivity. In both cases, the small zT is due to the low Seebeck coefficient and electrical conductivity. Both samples show that the maximum of zT falls in range of 200-250 ^{o}C which is different than the normal peak position at 400 ^{o}C for $Zn_{50}Sb_{50}$.[20]

Discussion on the TE properties and the micro-nanostructure of the pellet

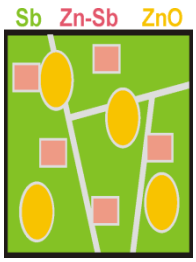

Figure 5.11. Schematic illustration of the micro-structure of the pellet

Based on the results of TE properties, it is clear that both of the pellets display the semiconducting characteristic. The Seebeck coefficient close to the value of Sb, and which is far from the value of ZnO (the sign of α is negative for ZnO) as well as ZnSb phases indicates the primary contribution of Sb in the pellet which is consistent with the result of composition

and structure analysis as illustrated in Fig. 5.11. The Zn-Sb and ZnO phase may distribute in the matrix of Sb, and the spaces between NPs/phases can exist in the sample.

Because the grain size of ZnO phase is smaller than 100 nm (of 55 nm in Sample IV pellet and even smaller than 20 nm in Sample III pellet), the thermal conductivity of ZnO with small grain size can be reduced to 3 $Wm^{-1}K^{-1}$ (for 20 nm grain size of ZnO in bulk sample)[32] compared to the bulk ZnO (~100 $Wm^{-1}K^{-1}$) (Table 5.3). The ZnSb and/or Sb phase also have grain size less than 100 nm. Moreover, the density of the pellets is lower than 90% of the theoretical value which can enhance the phonon scattering and reduce thermal conductivity. These reasons contribute to the fact that the thermal conductivity of both pellets is small. The electrical resistivity of these pellets is similar to ZnSb, even though the sample rich in Sb. There are several reasons for this result such as: the presence of ZnO phase with high electrical resistivity can inhibit the electrical conduction of Sb and/or ZnSb main phase in the pellet, the porosity of the pellet can also offer the electron scattering. The increase of electrical and thermal conductivity in the Sample IV pellet compared to Sample III pellet can be explained due to the increase in the grain size of the main ZnSb and/or Sb phases which is mainly because of the higher hot-pressing temperature used for Sample IV pellet.

Table 5.3 Thermoelectric properties of related materials. The data if not mentioned more were given at RT.

Materials	ρ **[**mΩ.m**]**	σ **[**μVK^{-1}**]**	κ **[**$WK^{-1}m^{-1}$**]**	zT	**d [**gcm^{-3}**]**	**Reference, note**
$Zn_{47}Sb_{53}$	0.11	196	2.3	4.56×10^{-3}	> 92% theoretical value	[21]
$Zn_{50}Sb_{50}$ bulk	0.2	300-500	1.41	0.6-0.8 (300 °C)	6.36	[20]
$Zn_{50}Sb_{50}$ single crystal	0.012	~200	3.7			[22], at 0 °C

Materials	ρ [mΩ.m]	σ [μVK^{-1}]	κ [WK^{-1}m^{-1}]	zT	d [gcm^{-3}]	Reference, note
$Zn_{50}Sb_{50}$ polycrystal		~200	1.3-2.6			[23,24]
Zn	6x10^{-5}	2.5	116		7.134	[18]
Sb	40x10^{-5}	24.4	20-50		6.697	[19]
ZnO	75x10^{7}-1.5x10^{6}					[25], n-type SC
ZnO bulk single crystal			100		5.607	[26],29
ZnO bulk polycrystal			30-40			[30,31]
ZnO, grain size<100 nm	10-500	-60~-100 (25-500 ^{o}C)	3	5x10^{-2} (300 ^{o}C)	90%	[32]
Sb_2O_3 thin film	5x10^{9} - 2.5x10^{4}					[27, 28]

5.4. Conclusion

In conclusion, the large scale syntheses were studied with different feeding ratios of metal molecular precursor, Zn:Sb, ranging from 50:50 to 66:34. The feeding ratio of Zn:Sb equal to 58:42 with and without the addition of Zn NPs results in the Zn-Sb NPs with composition of $Zn_{42}Sb_{58}$ and $Zn_{45}Sb_{55}$ respectively, which is the most similar to Zn-Sb NPs obtained in the small scale synthesis. The as-synthesized NPs after heat treatment were used to prepare the nanostructured pellets. The pellets show nanostructure and main phases similar to the as-synthesized sample, but, the oxidation of Zn (and partial oxidation of Sb) was found. It is important that the pellet shows the Seebeck coefficient is similar to Sb. The presence of ZnO is not good for the electrical conductivity and Seebeck coefficient of the sample. A part of the further work should be devoted to prevent the presence of ZnO. Further manipulation of the

as-synthesized NPs' composition and investigation of the post treatment and pelletizing conditions are necessary for the improvement of the TE properties.

Acknowledgement

Nguyen T. Mai would like to thank Assoc. Prof. Mikio Koyano and Dr. Koichiro Suekuni for useful discussion, Prof. Hideki Iwasaki and Dr. Go Nakamoto for their support, guidance and discussion in using hot-pressing machine, Prof. Tatsuya Shimoda for his permission of using TGA machine during my study. My thanks go to Dr. Yamamoto Atsushi in AIST for carry out the thermoelectric measurement on my sample.

References

[1] *Thermoelectrics Handbook: Macro to Nano*, ed. by D. M. Rowe, CRC Press, Boca Raton, FL, **2006**.

[2] G. J. Snyder, E. S. Toberer, *Nat. Mater.* **2008**, *7*, 105.

[3] S. B. Riffat, X. Ma, *Appl. Thermal Eng.* **2003**, *23*, 913.

[4] C. J. Vineis, A. Shakouri, A. Majumdar, M. G. Kanatzidis, *Adv. Mater*. **2010**, *22*, 3970.

[5] T. C. Harman, W. P. Walsh, B. E. Laforge, G. W. Turner, *J. Electron. Mater.* **2005**, *34*, 19.

[6] M. G. Kanatzidis, *Chem. Mater.* **2010**, *22*, 648.

[7] A. Scheele, N. Oeschler, K. Meier, A. Kornowski, C. Klinke, H. Weller, *Adv. Funct. Mater.* **2009**, *19*, 3476.

[8] A. Scheele, N. Oeschler, I. Veremchuk, K.-G. Reinsberg, A.-M. Kreuziger, A. Kornowski, J. Broekaert, C. Klinke, H. Weller, *ACS Nano* **2010**, *4*, 4283.

[9] G. J. Snyder, M. Christensen, E. Nishibori, T. Caillat, B. B. Iversen, *Nat. Mater.* **2004**, *3*, 458.

[10] L. Bjerg, G. K. H. Madsen, B. B. Iversen, *Chem. Mater.* **2011**, *23*, 3907.

[11] F. Cargnoni, E. Nishibori, P. Rabiller, L. Bertini, G. J. Snyder, M. Christensen, C. Gatti, B. B. Iversen, *Chem. Eur. J.* **2004**, *10*, 3861.

[12] S. Bhattacharya, R. P. Hermann, V. Keppens, T. M. Tritt, G. J. Snyder, *Phys. Rev. B* **2006**, *74*, 134108.

[13] A. Denoix, A. Solaiappan, R. M. Ayral, F. Rouessac, J. C. Tedenac, *J. Solid State Chem.* **2010**, *183*, 1090.

[14] S. Schlecht, C. Erk, M. Yosef, *Inorg. Chem.* **2006**, *45*, 1693.

[15] C. S. Birkel, E. Mugnaioli, T. Gorelik, U. Kolb, M. Panthöfer, W. Tremel, *J. Am. Chem. Soc.* **2010**, *132*, 9881.

[16] G. Kieslich, C. S. Birkel, A. Stewart, U. Kolb, W. Tremel, *Inorg. Chem.* **2011**, *50*, 6938.

[17] Nguyen T. Mai, D. Mott, K. Higashimine, S. Maenosono, *Chem. Lett.* **2012**, *41*, 1259.

[18] V. A. Rowe, P. A. Schroeder, *J. Phys. Chem. Sol.* **1970**, *31*, 1.

[19] G. A. Saunders, Ö. Öktu, *J. Phys. Chem. Solids* **1968**, *29*, 327.

[20] C. Okamura, T. Ueda, K. Hasezaki, *Mater. Trans.* **2010**, *51*, 860.

[21] L. T. Zhang, M. Tsutsui, K. Ito, M. Yamaguchi, *J. Alloys. Compd.* **2003**, *358*, 252.

[22] P. J. Shaver, J. Blair, *Phys. Rev.* **1966**, *141*, 469.

[23] R. R. Heikes, R. W. Ure, *Thermoelectricity: Science and Engineering*, Interscience Publishers, Inc., New York, **1961**, p. 406

[24] E. Justi, W. Rasch, G. Schneider, *Adv. Energy Convesion* **1964**, *4*, 27.

[25] T. K. Roy, D. Sanyal, D. Bhowmick, A. Chakrabarti, *Mater. Sci. Semiconductor Proc.* **2013**, *16*, 332.

[26] A. Y. Polyakov, N. B. Smirnov, A. V. Govorkov, E. A. Kozhukhova, S. J. Pearton, D. P. Norton, A. Osinsky, A. Dabiran, *J. Electronic Mater.* **2006**, *35*, 663.

[27] N. Tigău, National Conference on Applied Physics, 2006, Galati, Romania

[28] N. Tigău, *Rom. Jour. Phys.* **2008**, *53*, 203.

[29] Ü. Özgür, X. Gu, S. Chevtchenko, J. Spradlin, S.-J. Cho, H. Morkoç, F. H. Pollak, H. O. Everitt, B. Nemeth, J. E. Nause, *J. Electron. Mater.* **2006**, *35*, 550.

[30] T. Tsubota, M. Ohtaki, K. Eguchi, H. Arai, *J. Mater. Chem.* **1986**, *7*, 85.

[31] H. Kaga, Y. Kinemuchi, S. Tanaka, A. Makiya, Z. Kato, K. Uematsu, K. Watari, *Jpn. J. Appl. Phys.* **2006**, *45*, L1212.

[32] Y. Kinemuchi, M. Mikami, K. Kobayashi, K. Watari, Y. Hotta, *J. Electron. Mater.* **2010**, *39*, 2059.

Chapter 6

Conclusion and Prospects

My study was conducted to achieve the research objectives. The following summaries the achievement, contribution and prospects of the research:

1) My researches were designed to obtain TE NPs *via* suitable chemical approaches and to address the related fundamental issues on the chemical synthesis of NPs towards desired characteristics such as size, shape, composition, nanostructure and surface properties.

Regarding BiSbTe containing NP, I focus on a modified polyol synthesis to obtain various morphologies such as nanowires (NW)s, nanodiscs (ND)s or NDs grown on NWs. The phase segregation and complexity of the resulting BiSbTe NPs encourage us to investigate the formation mechanism of BiSbTe containing NPs systematically. The study on the formation mechanism of these NPs elucidated the important effect of capping molecules and the interaction between the metal precursor complexes. It is found that in the presence of oleyl amine as the capping agent, the formation of Te nanowires, BiSb alloy NPs and their solid solution formation can facilitate the formation of single NW composed of BiSbTe ternary alloy and Te segregated phases. On the other hand, the formation of Te and its catalytic activity in formation of Bi_2Te_3 and Sb_2Te_3 phases with the strong interaction between Te with Bi and Sb complex in the presence of decanethiol result in two phases in a single nanodisc, without any ternary phase of Bi, Sb and Te.

Based on the formation mechanism of Bi, Sb, Te containing NPs, a synthesis approach is further developed to obtain ternary alloy BiSbTe NPs with the manipulation of the NPs' composition and morphology. In this approach, BiSb NPs with tunable composition and relatively uniform morphology were successfully synthesized. These BiSb NPs were used as the seed for the growth of BiSbTe NPs. Ternary solid solution BiSbTe NPs can be formed with morphology similar to that of the seeds and the composition is expected to be tunable based on the seed composition and the feeding ratio between the seed and the Te precursor.

The chemical synthesis was studied for the Zn-Sb NPs which compose of relatively cheap and abundance elements and are challenging in term of creating Zn-Sb NPs *via* chemical

approach. The designed one-pot reaction with the first formation of Sb NPs as seeds followed by the reduction and growth of a Zn shell and subsequence alloying of Sb and Zn has succeeded to form Zn-Sb NPs with composition of $Zn_{47}Sb_{53}$. The resulting NPs are uniform in size and shape and reveal the complex nanostructure in which Zn and Sb show the radial distribution with Zn richer at the shell and Sb richer at the core, and the oxidation enhancement arises from the alloy formation between Zn and Sb was found in the resulting NPs.

2) Utilizing NPs as the building blocks to form the nanostructured TE materials was demonstrated in case of Zn-Sb NPs. The chemical synthesis of Zn-Sb NPs was scaled up to obtain gram amount of NPs. The scaled up reaction was studied with varying the feeding ratio of the metal precursors to obtain Zn-Sb NPs which have similar characteristics (morphology, composition and structure) with the Zn-Sb NPs obtained in the small scale synthesis. The NPs underwent the surface treatment and pressing to form the pellet. It is found that the resulting bulk pellet has the nanograin size and interesting TE properties.

3) The research on the synthesis, formation mechanism and manipulation of NPs' characteristics such as morphology, composition and structure can contribute to the fundamental understanding on the formation of NPs with tunable characteristics in chemical approach. Moreover, the chemical synthesis in this research is proved to be scalable to produce large amount of NPs which is important for using NPs to create the nanostructured bulk materials. All of the results in this study encourage the further study on the conditions of post treatment and creating nanostructured materials, the TE properties and the impact of NPs' characteristics on the TE properties.

Appendix I

for

General Introduction to Thermoelectric Materials and Research Objective

1.1. The current state of the art TE materials

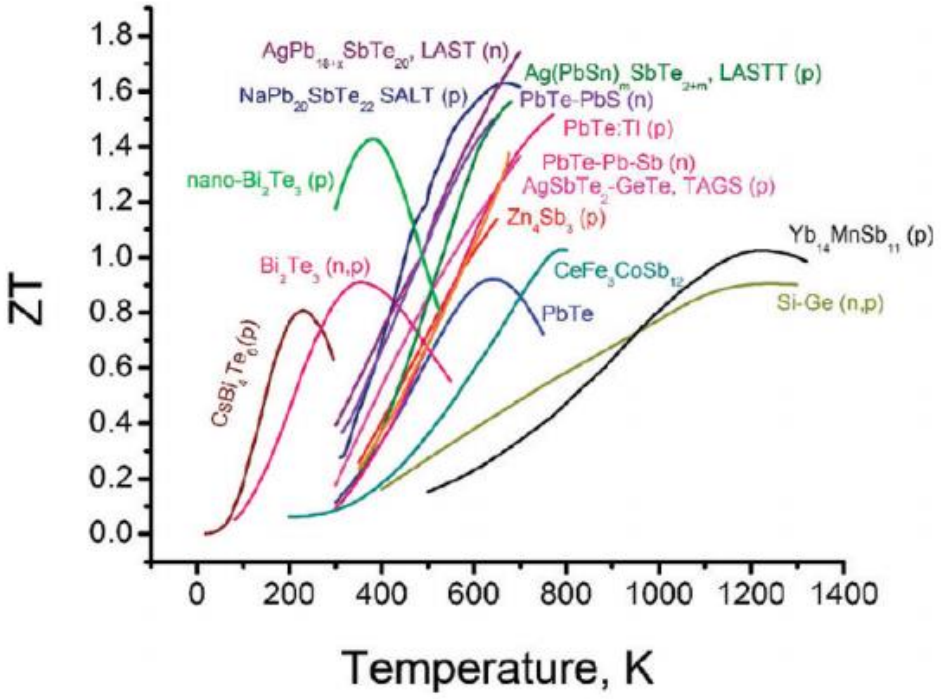

Figure A1.1. Current state-of-the-art in bulk TE materials. Adapted from M. G. Kanatzidis, *Chem. Mater.* **2010**, *22*, 648-659.

1.2. Characterization Methods

This section briefly describes the characterization methods used in the study to (i) investigate the nanoparticles's characteristics including: morphology, sizes, crystal structure and phases, composition, surface properties;[1-6] (ii) measure the thermoelectric properties of the nanostructured materials[7,8,9] such as methods to measure α, α, κ, and n; and (iii) measure others related properties.

1.2.1. Nanostructure analysis

Electron microscopy

Electron microscopy use the primary electron beam with characteristic wavelength less than 1 Å interacting with the NPs then collecting the transmitted, diffracted, scattered, secondary or backscattered electron,… giving information about sample characteristics. This method includes some of the straight forward techniques to determine the size and shape of the NPs as well as correlating with the NPs' composition and structure.

- A part of primary electron passes through the sample (transmitted electrons) and the attenuation of the transmitted electron beam depends on the thickness and the density of the sample giving the two dimensional projection of the sample. This is the principle of the normal Transmission Electron Microscope (TEM). Because the atoms with higher mass will scatter electron stronger than lower mass atoms, it will contribute apart to the contrast in the TEM images beside the thickness of the sample.
- The diffracted electron obtained when the primary electron beam hit the sample can be used to analyze the crystallographic of the sample. The Selected Area Electron Diffraction (SAED) can be collected for analyzing the crystal structure of the NPs. The High Resolution TEM (HR-TEM) is also operated based on the collection of diffracted electrons which interferes consecutively. HR-TEM can display the lattice fringes of the crystal structured NPs. From these data, the crystal planes and direction can be addressed. Under certain conditions, the information can be used to discuss about the growth direction of NPs.
- The high angle scattered electron can be collected using an annual dark field detector with spherical aberration corrector to give the dark-field images (High Angular Annual Dark Field image, HAAD image). This technique allows the atomic resolution and the contrast in the images with the intensity (the brightness of the image) is proportional to the atomic number of the atom (Z-contrast) present in the sample.
- Scanning Electron Microsope (SEM) involves rastering the electron beam over the surface of the sample and collecting either secondary electron or backscattered electrons as a function of the position of primary electrons. The part of the surface facing to the detector appears brighter than the part that points away from the detector resulting in the contrast of the image. The secondary electrons are often originated from the surface region while the backscattered electrons come from deeper region and have the information of the sample's composition. The intensity of the backscattered electron beam depends on the atomic number

of the element present in the sample and the area of higher atomic number atoms is brighter in the image.

- Furthermore, the characteristic X-rays emitted from the interaction of electron and atom in the sample are identical for the element, and the amount of the atoms is proportion to the emission's intensity. Hence, the characteristic X-ray emission can be used to determine the composition of the sample qualitative and quantitatively. This content relates to the Energy Dispersive X-ray Spectroscopy (EDS) which often correlated with TEM or SEM machines to measure NPs composition. The elemental mapping correlated with STEM or SEM can give the distribution of element in single NP in correlation with NP's morphology.

X-ray Diffraction

X-ray Diffraction (XRD) is one of the most important methods to characterize the crystal structure and phases of the NPs' powder or thin film *via* identify the lattice structural parameters. The X-ray diffraction occurs when X-ray elastically scattered by the atoms in the lattice which satisfies the Bragg equation:

$$n\lambda = 2d\sin\theta \qquad \text{(Eq. A1.1)}$$

where λ, d, θ and n is the X-ray wavelength, the distance between two lattice planes, the angle between incoming X-ray and the normal to the reflecting lattice planes and the order of the diffraction (integer number) respectively.

In the XRD pattern, the sharp peak can only observe for the sample with long-range order . The peak becomes broaden when the short-range order of the phase (the size of the ordered range is so-called crystalline size) exists in the sample due to either the small particles' size or the polycrystalline domains. Therefore, beside the information of the lattice parameters, XRD data also carry important information about the mean crystalline size of the NPs. The relation between the peak broadening and the mean crystalline size was described in Scherrer formula:

$$\langle L\rangle = K\lambda/(\beta\cos\theta) \qquad \text{(Eq. A1.2)}$$

where $\langle L\rangle$ is the crystalline size of the phase related to the broadening peak, K is the shape factor which is typical 0.9 for spherical particles but varies for other shape, and β is the peak width at half the maximum (FWHM) intensity of the peak at 2θ degree. Based on the line

broadening, one can calculate the average crystalline size of the sample, and in case of the NPs, this number can reveal the size of the NPs as well.

X-ray Photoelectron Spectroscopy (XPS)

XPS is among the most used techniques to analyze the surface properties of NPs including the elemental composition (quantitative and qualitative), the oxidation state of the element (the interaction of surface adsorbed molecules to the NPs). Taken into account the size of NPs, this method is informative in indicating the sample composition.

XPS is based on the photoelectronic effect in which an atom absorbs a photon of energy $h\nu$, then the electron in the core level with binding energy E_b emit (photoelectron) with kinetic energy E_k. The binding energy of the photoelectron can be calculated based on the energy conservation equation:

$$E_b = h\nu - E_k - \Phi \qquad \text{(Eq. A1.3)}$$

where Φ is the work function of the spectrometer.

The intensity *vs.* the kinetic energy of photoelectron was measured and then the kinetic energy was used to converse to the binding energy. The binding energy, E_b is identical for element that the photoelectron emitted from. Because an electron in the atom has the orbital and spin momentums which represents by the quantum number l and s respectively, each electron has the total momentum j = l + s. Except for l = 0 (s orbital), electron in each level has two sublevels j = l ± 1/2 with different energy resulting in two XPS peaks (spin-orbit doublet) with different binding energy from electron of one core level. The intensity ratio of the spin-orbit doublets is spin-orbit ratio which determined by multiply (2j+1) to the corresponding sublevels, for instance, the spin-orbit ratio of j = 3/2 and j = 1/2 (l = 1, s = ±1/2, p orbital) is 4:2 = 2:1. The binding energy difference called spin-orbit splitting is also characteristic of the elements. Therefore, the XPS peaks' positions (binding energy axis) and the spin-orbit splitting can indicate the elements present in the sample.

Moreover, because the energy of the core electrons slightly depends on the chemical state of the atom, the binding energy also contains the chemical information by mean of the shift of binding energy (so-called chemical shift). It is explained due to the fact that the core electrons of a neutral atom bind loser to the nuclei compared to the core electrons of a cation and stronger in comparison to that of an anion. Therefore, one can record the chemical shift in

the XPS spectrum. The chemical shifts often range from 0 to 3 eV and can be used to discuss the chemical state of the element. It is noted that when analyze the chemical shift for NPs sample which have large surface to volume ratio of atoms (surface atoms do not possess saturated bonding, usually), the chemical state and the size effect should be taken into account.

1.2.2. Elemental analysis

There are many methods to determine the composition of NPs, the mainly used method in case of this study to measure the average elemental composition is Inductively Couple Plasma- Optical Emission Spectroscopy or Mass Spectroscopy (ICP-OES/MS). ICP-MS is based on ionizing the sample with inductively couple plasma then using the mass spectroscopy as the detector to separate and quantify the ions. ICP-MS offers very sensitive, high accurate analysis with the concentration of ions in order of one per billion. In ICP-OES, atoms and ions were excited by plasma (ICP) to emit the characteristic radiations for the elements presenting in the sample. The emission will be separated based on their wavelength and counted for the intensity in the optical chamber. The intensity of the emission light (ICP-OES) or the isotopes (collected in MS) is proportional to the concentration of element in the sample. An array of known concentration solution of the concerned elements was measured to build the calibration curve which then was used to calculate the amount of the investigated element in the sample.

Beside the mentioned methods, TEM-EDS and SEM-EDS and XPS can also be used to measure the composition (relative) of the NPs' sample. In certain condition, the composition of single NP is required, the TEM-EDS becomes crucial important method. However, it is noticed that in case of using EDS or XPS to determine the composition of the sample, the size and the homogeneity of the sample should be considered because the penetration of electron beam and X-ray beam as well as the mean free path of the characteristic emitted electron/photoelectron are smaller than the thickness of the NPs which under the radiation beam.

1.2.3. Thermoelectric property measurements

In order to investigate the TE properties of the TE materials, α, σ, κ, carrier concentration, and density of the sample are normally required. The following will mention about the measurement of those properties and parameter. The review on these measurements can be found in references.

Electrical conductivity

Electrical conductivity is often calculated from the electrical resistivity of the sample *via* the equation $\alpha = 1/\rho$ where ρ is the electrical resistivity. For the bulk sample, the four probe method is typically used where current and voltage are injected through different sets of current leads and voltage leads to prevent the contribution of the leads or the contacts (contact resistance) to the voltage measurement. One can obtain the voltage and the current value which leads to the resistance of the sample. To obtain the resistivity, ρ, the dimension of the sample should be measured accurately and ρ will be drawn from the relation:

$$\rho = VA/Il \qquad \text{(Eq. A1.4)}$$

where *V, I, A* and *lo* are the voltage, current, cross area between two current leads and length between two voltage leads of the sample respectively. It is required that the current is uniform through the sample where the voltage was measured. Hence the configuration of the sample and the leads position should satisfy $l\text{-}lo \geq 2w$, where *l* and w are the length and the thickness of the sample respectively. The resistivity (conductivity) measurement is relatively straightforward and simple; however, it is still necessary to pay much attention because TE materials are often SCs which can easily have oxide layer on the surface causing some difficulties in creating good electrical contact. Other reason is the p-n junction contact between SCs and the leads and resulting nonohmic voltages which can contribute some errors to the resistivity measurement.

Seebeck coefficient

The Seebeck coefficient is calculated from the measured voltages arise due to the temperature gradient along the sample:

$$\alpha_o = \Delta V/\Delta T = (V_H - V_L)/(T_H - T_L) \qquad \text{(Eq. A1.5)}$$

where $\alpha_o = (\alpha' - \alpha)$ is the measure value of Seebeck coefficient including the part contribution from sample (α) and the leads (α'). The error in measuring Seebeck coefficient is independent of the sample dimensions, but much depends on the determination of the temperature gradient of the sample. Another error source of the Seebeck coefficient measurement comes from the placement of thermal couples in relation to the voltage leads. Ideally, the thermal couples should be placed at the position of voltage leads, or used as voltage leads and precisely measure the temperature. In both cases, good thermal and electrical contact is required.

Thermal conductivity

Thermal conductivity measurements are the most difficult to make with relatively high accuracy, 5%. The typical TE materials has low thermal conductivity, $\kappa \leq 2$ $Wm^{-1}K^{-1}$, which is challenging for an accurate measurement because the heat will flow through the other paths of higher thermal conductivity such as any gas flow around the sample. The thermal conductivity for a standard steady-state method is given by:

$$\lambda_T = Q_T l_o / A\Delta T \qquad \text{(Eq. A1.6)}$$

where Q_T is the heater power, ΔT is the resulting temperature difference, l_o is the length between thermocouple leads and A is the cross section area of the sample.

An accurate measurement of thermal conductivity should be done with minimizing the heat losses (or gain) through the convection, radiation between sample and environments or conduction through the thermocouples, leads attached to the sample. The best way is to conduct the measurement under moderate vacuum (10^{-4}-10^{-5} torr), using a long lead lengths of small diameter (to reduce the ΔT arises between sample and the shield). Using an array of standard samples for each temperature range to calibrate the measurement apparatus is essential for an accurate measurement of thermal conductivity in the standard steady-state method.

Physical Property Measurement System-Thermal Transport Option to measure λ_T (PPMS-TTO) based on the mentioned principle with providing the high vacuum environment for the designed TTO sample puck. Using PPMS-TTO can give measurement of the thermal conductivity with high accuracy, 5%, due to the ability of accurate measurement of small temperature differentials, controlling the heat flow, and correcting the heat losses.

For thin film sample, 3-ω method can be used to measure the thermal conductivity. This technique is originally developed to measure the thermal conductivity of glasses and amorphous solids, and later on, for the thin film samples. In this technique, a thin metal film was deposited on the sample (thin film). An AC current heating (frequency of ω) is applied to the film, providing an oscillating heat source (Joul heating) ($P = I^2R$) of frequency of 2ω. The Joul heating leads to the temperature fluctuation at frequency of 2ω. The resistance of the film is dependent on the temperature fluctuation also at 2ω. Therefore, the monitored voltage ($V = IR$) as the function of the frequency of the AC current, will have the 3ω component. The thermal conductivity will be determined by means of the linear slope of ΔT vs. $\ln(\omega)$. The 3-ω method

is advantageous compared to standard steady state technique in terms of radiation effects and contact effect.

The thermal conductivity can be measured using laser flash thermal diffusivity methods for both bulk and thin film. This method measure the thermal diffusivity of the sample which will be used to draw the thermal conductivity (equal to thermal diffusivity time specific heat and density). In this technique, one face of the sample was radiated by the short laser pulse and on the other opposite face of the sample, the temperature rises is measured. The thermal diffusivity was measured *via* the temperature rises *vs.* time profile. The thermal diffusivity measurement requires a sample surfaces highly emissive to maximize the thermal energy transmitted from one to opposite surface, hence maximize the collected signal by the detector. The laser flash method can be used to measure the diffusivity in temperature range from 77 to 2300 K.

It is important notice on the measurement data of thermal conductivity regarding the density of the sample. Because the high porosity sample will offer huge vacant space inside and the vacant space can play a role of scattering or reducing thermal conductivity. Therefore, the very low thermal conductivity can be obtained in a measurement, but it may not reflex the intrinsic low thermal conductivity of the sample due to lowering the lattice thermal conductivity, but instead due to the high porosity of the sample. This notice often important when discuss about the mechanism and meaning of thermal conductivity value measured for nanostructured materials which prepared from the NPs building block by pressing/sintering because these samples may not have the same density as the bulk counterpart. Density higher than 90 % the theoretical value can be considered as good for thermal conductivity measurement. In some cases, density higher than 80 % of the theoretical value can be used. In these cases, the correction is necessary to extract the thermal conductivity value which can be attributed to the lattice and electrical thermal conductivity.

Others. Other parameters are also important in studying the TE properties of TE materials including carrier concentration, carrier mobility, Hall voltage, Hall coefficient and density. The measurement of those parameters can be found in the literature.

References

[98] P. W. Hawkes, J. C. H. Spence, *Science of Microscopy*, Vol I, Springer Science+ Business Media, LLC, **2007**.

[99] R. Wiesendanger, *Scanning Probe Microsopy and Spectroscopy Methods and Applications*, Cambridfe University Press, **1994**.

[100] J. P. Glusker, M. Lewis, M. Rossi, *Crystal Structure Analysis for Chemists and Biologists*, VCH Publishers, Inc. **1994**.

[101] D. C. Harris, *Quantitative Chemical Analysis*, W. H. Freeman and Company, **2007**.

[102] S. Hüfner, *Photoelectron Spectroscopy Principle and Applications*, in *Springer Series in Solid-State Sciences*, Springer-Verlag Berlin Heidelberg, **1995**.

[103] W. Suëtaka, *Surface Infrared and Raman Spectroscopy Methods and Applications*, Plenum Press, NY, **1995**.

[104] R. Taylor, In *CRC Handbook of Thermoelectrics*, Ed. by D. M. Rowe, CRC Press, Boca Raton, FL, **1995**.

[105] D. W. Koon, C. J. Knickerbocker, *Rev. Sci. Instrum.* **1992**, *63*, 207.

[106] T. M. Tritt, *Recent Trends in Thermoelectric Materials Research*, in *Semiconductors and Semimetals*, Academic Press, CA, **2001**.

Appendix II

for

Study on Formation Mechanism and Ligand-directed Architectural Control of Nanoparticles Composed of Bi, Sb and Te: toward One-pot Synthesis of Ternary $(Bi,Sb)_2Te_3$ Nanobuilding Blocks

2.1. XRD Peak Assignments

2.1.1. Monometallic Systems

2.1.1.1. Bi monometallic systems

Table A2.1. XRD peak positions and corresponding crystal planes for Fig. 2.1A (Bi-OAM system).

2 Theta (Degree)	Intensity	Phase	(*h k l*)
22.42	Very weak	Bi (RHO)	(0 0 3)
24.16	Strong	BiOCl (TET)	(0 0 2)
25.88	Medium	BiOCl (TET)	(1 0 1)
27.15	Medium	Bi (RHO)	(0 1 2)
32.48	Strong	BiOCl (TET)	(1 1 0)
33.44	Strong	BiOCl (TET)	(1 0 2)
34.73	Very weak	BiOCl (TET)	(1 1 1)
36.56	Medium	BiOCl (TET)	(0 0 3)
38.01	Weak	Bi (RHO)	(1 0 4)
39.70	Weak	Bi (RHO)	(1 1 0)
40.89	Weak	BiOCl (TET)	(1 1 2)
44.53	Very weak	Bi (RHO)	(0 1 5)
45.93	Very weak	Bi (RHO)	(0 0 6)
46.60	Weak	BiOCl (TET)	(2 0 0)
48.36	Very weak	BiOCl (TET)	(2 0 1)
48.76	Very weak	Bi (RHO)	(2 0 2)
49.62	Weak	BiOCl (TET)	(1 1 3)
53.06	Very weak	BiOCl (TET)	(2 0 2)
54.04	Weak	BiOCl (TET)	(2 1 1)
55.14	Weak	BiOCl (TET)	(1 0 4)
58.56	Weak	BiOCl (TET)	(2 1 2)

RHO=Rhombohedral, TET=Tetragonal

Table A2.2. XRD peak positions and corresponding crystal planes for Fig. 2.1B (Bi-OAC/OAM system).

2 Theta (Degree)	Intensity	Phase	(*h k l*)
24.10	Strong	BiOCl (TET)	(0 0 2)
25.78	Weak	BiOCl (TET)	(1 0 1)
27.16	Weak	Bi (RHO)	(0 1 2)
32.50	Medium	BiOCl (TET)	(1 1 0)
33.40	Medium	BiOCl (TET)	(1 0 2)
34.76	Very weak	BiOCl (TET)	(1 1 1)
36.54	Strong	BiOCl (TET)	(0 0 3)
37.96	Weak	Bi (RHO)	(1 0 4)
39.54	Weak	Bi (RHO)	(1 1 0)
40.88	Weak	BiOCl (TET)	(1 1 2)
44.60	Very weak	Bi (RHO)	(0 1 5)
45.90	Very weak	Bi (RHO)	(0 0 6)
46.60	Weak	BiOCl (TET)	(2 0 0)
48.34	Very weak	BiOCl (TET)	(2 0 1)
49.56	Weak	BiOCl (TET)	(1 1 3)
53.16	Very weak	BiOCl (TET)	(2 0 2)
54.10	Weak	BiOCl (TET)	(2 1 1)
55.02	Weak	BiOCl (TET)	(1 0 4)
58.56	Weak	BiOCl (TET)	(2 1 2)

RHO=Rhombohedral, TET=Tetragonal

Table A2.3. XRD peak positions and corresponding crystal planes for Fig. 2.1C (Bi-DT system).

2 Theta (Degree)	Intensity	Phase	(*h k l*)
22.44	Very weak	Bi (RHO)	(0 0 3)
23.81	Very weak	Bi (RHO)	(1 0 1)
27.12	Strong	Bi (RHO)	(0 1 2)
37.92	Medium	Bi (RHO)	(1 0 4)
39.59	Medium	Bi (RHO)	(1 1 0)
44.53	Very weak	Bi (RHO)	(0 1 5)
45.95	Very weak	Bi (RHO)	(0 0 6)
46.89	Very weak	Bi (RHO)	(0 2 1)
48.66	Weak	Bi (RHO)	(2 0 2)
55.97	Very weak	Bi (RHO)	(0 2 4)
59.29	Very weak	Bi (RHO)	(1 0 7)

RHO=Rhombohedral

2.1.1.2. Sb monometallic systems

Table A2.4. XRD peak positions and corresponding crystal planes for Fig. 2.2A (Sb-OAM system).

2 Theta (Degree)	Intensity	Phase	(*h k l*)
23.66	Very weak	Sb (RHO)	(0 0 3)
28.65	Strong	Sb (RHO)	(0 1 2)
39.98	Weak	Sb (RHO)	(1 0 4)
41.88	Weak	Sb (RHO)	(1 1 0)
46.98	Very weak	Sb (RHO)	(0 1 5)
48.41	Very weak	Sb (RHO)	(0 0 6)
51.54	Very weak	Sb (RHO)	(2 0 2)
59.39	Very weak	Sb (RHO)	(0 2 4)

RHO=Rhombohedral

Table A2.5. XRD peak positions and corresponding crystal planes for Fig. 2.2B (Sb-OAC/OAM system).

2 Theta (Degree)	Intensity	Phase	(*h k l*)
23.64	Very weak	Sb (RHO)	(0 0 3)
28.62	Strong	Sb (RHO)	(0 1 2)
40.00	Medium	Sb (RHO)	(1 0 4)
41.91	Medium	Sb (RHO)	(1 1 0)
47.09	Very weak	Sb (RHO)	(0 1 5)
48.35	Very weak	Sb (RHO)	(0 0 6)
51.50	Weak	Sb (RHO)	(2 0 2)
59.33	Very weak	Sb (RHO)	(0 2 4)

RHO=Rhombohedral

2.1.1.3. Te monometallic systems

Table A2.6. XRD peak positions and corresponding crystal planes for Fig. 2.3A (Te-OAM system).

2 Theta (Degree)	Intensity	Phase	(*h k l*)
23.00	Weak	Te (HEX)	(1 0 0)
27.52	Strong	Te (HEX)	(1 0 1)
38.22	Medium	Te (HEX)	(1 0 2)
40.41	Medium	Te (HEX)	(1 1 0)
43.36	Very weak	Te (HEX)	(1 1 1)
45.97	Very weak	Te (HEX)	(0 0 3)
47.12	Very weak	Te (HEX)	(2 0 0)
49.62	Weak	Te (HEX)	(2 0 1)
51.22	Very weak	Te (HEX)	(1 1 2)
51.93	Very weak	Te (HEX)	(1 0 3)
56.83	Very weak	Te (HEX)	(2 0 2)

HEX=Hexagonal

Table A2.7. XRD peak positions and corresponding crystal planes for Fig. 2.3B (Te-OAC/OAM system).

2 Theta (Degree)	Intensity	Phase	(*h k l*)
23.00	Weak	Te (HEX)	(1 0 0)
27.52	Strong	Te (HEX)	(1 0 1)
38.24	Weak	Te (HEX)	(1 0 2)
40.42	Weak	Te (HEX)	(1 1 0)
43.36	Very weak	Te (HEX)	(1 1 1)
45.88	Very weak	Te (HEX)	(0 0 3)
47.12	Very weak	Te (HEX)	(2 0 0)
49.62	Very weak	Te (HEX)	(2 0 1)
51.24	Very weak	Te (HEX)	(1 1 2)
52.04	Very weak	Te (HEX)	(1 0 3)
56.84	Very weak	Te (HEX)	(2 0 2)

HEX=Hexagonal

Table A2.8. XRD peak positions and corresponding crystal planes for Fig. 2.3C (Te-DT system).

2 Theta (Degree)	Intensity	Phase	(*h k l*)
23.00	Weak	Te (HEX)	(1 0 0)
27.54	Strong	Te (HEX)	(1 0 1)
38.24	Medium	Te (HEX)	(1 0 2)
40.46	Weak	Te (HEX)	(1 1 0)
43.42	Very weak	Te (HEX)	(1 1 1)
46.04	Very weak	Te (HEX)	(0 0 3)
47.16	Very weak	Te (HEX)	(2 0 0)
49.68	Very weak	Te (HEX)	(2 0 1)
51.24	Very weak	Te (HEX)	(1 1 2)
52.06	Very weak	Te (HEX)	(1 0 3)
56.88	Very weak	Te (HEX)	(2 0 2)

HEX=Hexagonal

2.1.2. Bimetallic Systems

2.1.2.1. Bi-Sb bimetallic systems

Table A2.9. XRD peak positions and corresponding crystal planes for Fig. 2.4A (Bi/Sb-OAM system).

2 Theta (Degree)	Intensity	Phase	(*h k l*)
27.45	Strong	BiSb (RHO)	(0 1 2)
38.34	Weak	BiSb (RHO)	(1 0 4)
40.33	Medium	BiSb (RHO)	(1 1 0)
46.34	Very weak	BiSb (RHO)	(0 1 5)
49.44	Very weak	BiSb (RHO)	(2 0 2)
56.78	Very weak	BiSb (RHO)	(0 2 4)

RHO=Rhombohedral

Table A2.10. XRD peak positions and corresponding crystal planes for Fig. 2.4B (Bi/Sb-OAC/OAM system).

2 Theta (Degree)	Intensity	Phase	(*h k l*)
22.54	Very weak	BiSb (RHO)	(0 0 3)
27.28	Strong	BiSb (RHO)	(0 1 2)
38.14	Weak	BiSb (RHO)	(1 0 4)
39.78	Medium	BiSb (RHO)	(1 1 0)
44.78	Very weak	Bi (RHO)	(0 1 5)
46.12	Very weak	BiSb (RHO)	(0 1 5)
48.96	Very weak	BiSb (RHO)	(2 0 2)
56.28	Very weak	BiSb (RHO)	(0 2 4)

RHO=Rhombohedral

Table A2.11. XRD peak positions and corresponding crystal planes for Fig. 2.4C (Bi/Sb-DT system).

2 Theta (Degree)	Intensity	Phase	(*h k l*)
22.32	Weak	Bi (RHO)	(0 0 3)
23.60	Very weak	Bi (RHO)	(1 0 1)
27.14	Strong	Bi (RHO)	(0 1 2)
37.92	Medium	Bi (RHO)	(1 0 4)
39.60	Medium	Bi (RHO)	(1 1 0)
44.56	Very weak	Bi (RHO)	(0 1 5)
45.18	Very weak	Bi (RHO)	(0 0 6)
45.90	Very weak	Bi (RHO)	(1 1 3)
46.74	Very weak	Bi (RHO)	(0 2 1)
48.66	Very weak	Bi (RHO)	(2 0 2)
56.02	Very weak	Bi (RHO)	(0 2 4)
59.30	Very weak	Bi (RHO)	(1 0 7)

RHO=Rhombohedral

2.1.2.2. Bi-Te bimetallic systems

Table A2.12. XRD peak positions and corresponding crystal planes for Fig. 2.6A (Bi/Te-OAM system).

2 Theta (Degree)	Intensity	Phase	(*h k l*)
23.01	Weak	Te (HEX)	(1 0 0)
27.56	Strong	Te (HEX)	(1 0 1)
38.31	Very weak	Te (HEX)	(1 0 2)
40.34	Medium	Te (HEX)	(1 1 0)
43.36	Very weak	Te (HEX)	(1 1 1)
45.88	Very weak	Te (HEX)	(0 0 3)
47.02	Very weak	Te (HEX)	(2 0 0)
49.57	Weak	Te (HEX)	(2 0 1)
51.42	Very weak	Te (HEX)	(1 1 2)
56.91	Very weak	Te (HEX)	(2 0 2)

HEX=Hexagonal

Table A2.13. XRD peak positions and corresponding crystal planes for Fig. 2.6B (Bi/Te-OAC/OAM system).

2 Theta (Degree)	Intensity	Phase	(*h k l*)
23.02	Weak	Te (HEX)	(1 0 0)
27.54	Strong	Te (HEX)	(1 0 1)
38.28	Weak	Te (HEX)	(1 0 2)
40.40	Weak	Te (HEX)	(1 1 0)
43.38	Very weak	Te (HEX)	(1 1 1)
45.98	Very weak	Te (HEX)	(0 0 3)
47.16	Very weak	Te (HEX)	(2 0 0)
49.62	Weak	Te (HEX)	(2 0 1)
51.26	Very weak	Te (HEX)	(1 1 2)
52.08	Very weak	Te (HEX)	(1 0 3)
56.86	Very weak	Te (HEX)	(2 0 2)

HEX=Hexagonal

Table A2.14. XRD peak positions and corresponding crystal planes for Fig. 2.6C (Bi/Te-DT system).

2 Theta (Degree)	Intensity	Phase	(*h k l*)
23.60	Very weak	Bi_2Te_3 (RHO)	(1 0 1)
27.62	Strong	Bi_2Te_3 (RHO)	(0 1 5)
37.96	Weak	Bi_2Te_3 (RHO)	(1 0 10)
40.38	Very weak	Bi_2Te_3 (RHO)	(0 1 11)
41.16	Weak	Bi_2Te_3 (RHO)	(1 1 0)
44.68	Very weak	Bi_2Te_3 (RHO)	(0 0 15)
45.00	Very weak	Bi_2Te_3 (RHO)	(1 1 6)
50.32	Very weak	Bi_2Te_3 (RHO)	(2 0 5)
54.02	Very weak	Bi_2Te_3 (RHO)	(0 0 18)
57.18	Very weak	Bi_2Te_3 (RHO)	(0 2 10)

RHO=Rhombohedral

2.1.2.3. Sb-Te bimetallic systems

Table A2.15. XRD peak positions and corresponding crystal planes for Fig. 2.7A (Sb/Te-OAM system).

2 Theta (Degree)	Intensity	Phase	(*h k l*)
22.94	Weak	Te (HEX)	(1 0 0)
27.43	Strong	Te (HEX)	(1 0 1)
38.15	Weak	Te (HEX)	(1 0 2)
40.37	Strong	Te (HEX)	(1 1 0)
43.18	Weak	Te (HEX)	(1 1 1)
45.87	Very weak	Te (HEX)	(0 0 3)
47.02	Very weak	Te (HEX)	(2 0 0)
49.49	Medium	Te (HEX)	(2 0 1)
51.22	Very weak	Te (HEX)	(1 1 2)
51.93	Very weak	Te (HEX)	(1 0 3)
56.72	Weak	Te (HEX)	(2 0 2)

HEX=Hexagonal

Table A2.16. XRD peak positions and corresponding crystal planes for Fig. 2.7B (Sb/Te-OAC/OAM system).

2 Theta (Degree)	Intensity	Phase	(*h k l*)
23.00	Weak	Te (HEX)	(1 0 0)
27.54	Strong	Te (HEX)	(1 0 1)
38.26	Weak	Te (HEX)	(1 0 2)
40.42	Medium	Te (HEX)	(1 1 0)
43.34	Very weak	Te (HEX)	(1 1 1)
45.88	Very weak	Te (HEX)	(0 0 3)
47.06	Very weak	Te (HEX)	(2 0 0)
49.62	Weak	Te (HEX)	(2 0 1)
51.24	Very weak	Te (HEX)	(1 1 2)
52.04	Very weak	Te (HEX)	(1 0 3)
56.86	Very weak	Te (HEX)	(2 0 2)

HEX=Hexagonal

Table A2.17. XRD peak positions and corresponding crystal planes for Fig. 2.7C (Sb/Te-DT system).

2 Theta (Degree)	Intensity	Phase	(*h k l*)
23.00	Very weak	Te (HEX)	(1 0 0)
26.32	Very weak	Sb_2Te_3 (RHO)	(0 0 9)
26.80	Very weak	Sb_2Te_3 (RHO)	(1 0 4)
27.54	Weak	Te (HEX)	(1 0 1)
28.20	Strong	Sb_2Te_3 (RHO)	(0 1 5)
31.70	Very weak	Sb_2Te_3 (RHO)	(1 0 7)
33.80	Very weak	Sb_2Te_3 (RHO)	(0 1 8)
38.26	Medium	Sb_2Te_3 (RHO), Te (HEX)	(1 0 10), (1 0 2)
40.42	Very weak	Te (HEX)	(1 1 0)
40.70	Very weak	Sb_2Te_3 (RHO)	(0 1 11)
42.30	Weak	Sb_2Te_3 (RHO)	(1 1 0)
43.32	Very weak	Te (HEX)	(1 1 1)
44.58	Very weak	Sb_2Te_3 (RHO)	(0 0 15)
45.94	Very weak	Sb_2Te_3 (RHO), Te (HEX)	(1 0 13), (0 0 3)
48.54	Very weak	Sb_2Te_3 (RHO)	(0 1 14)
49.60	Very weak	Te (HEX)	(2 0 1)
50.56	Very weak	Sb_2Te_3 (RHO)	(1 1 9)
51.64	Very weak	Sb_2Te_3 (RHO)	(2 0 5)
54.20	Very weak	Sb_2Te_3 (RHO)	(0 0 18)
56.86	Very weak	Sb_2Te_3 (RHO), Te (HEX)	(0 1 17), (2 0 2)
58.36	Very weak	Sb_2Te_3 (RHO)	(0 2 10)

HEX=Hexagonal, RHO=Rhombohedral

2.1.3. Trimetallic System

Table A2.18. XRD peak positions and corresponding crystal planes for Fig. 2.9 (Bi/Sb/Te-OAM system).

2 Theta (Degree)	Intensity	Phase	(*h k l*)
22.98	Very weak	Te (HEX)	(1 0 0)
23.56	Very weak	BiSbTe (RHO)	(1 0 1)
27.59	Strong	Te (HEX), BiSbTe (RHO)	(1 0 1), (0 1 5)
33.27	Very weak	BiSbTe (RHO)	(0 1 8)
37.73	Medium	BiSbTe (RHO)	(1 0 10)
38.21	Weak	Te (HEX)	(1 0 2)
40.38	Weak	Te (HEX)	(1 1 0)
41.11	Medium	BiSbTe (RHO)	(1 1 0)
43.28	Very weak	Te (HEX)	(1 1 1)
44.46	Very weak	BiSbTe (RHO)	(0 0 15)
44.95	Very weak	BiSbTe (RHO)	(1 1 6)
45.44	Very weak	BiSbTe (RHO)	(1 0 13)
45.86	Very weak	Te (HEX)	(0 0 3)
49.55	Very weak	Te (HEX)	(2 0 1)
50.27	Weak	BiSbTe (RHO)	(2 0 5)
51.16	Very weak	Te (HEX)	(1 1 2)
51.92	Very weak	Te (HEX)	(1 0 3)
53.74	Very weak	BiSbTe (RHO)	(1 0 16)
56.84	Very weak	Te (HEX)	(2 0 2)
57.05	Weak	BiSbTe (RHO)	(0 2 10)
58.95	Very weak	BiSbTe (RHO)	(2 0 11)
62.17	Weak	BiSbTe (RHO)	(1 1 15)

62.76	Very weak	BiSbTe (RHO)	(0 2 13)
63.66	Very weak	BiSbTe (RHO)	(0 0 21)
65.90	Weak	BiSbTe (RHO)	(0 1 20)
66.88	Weak	BiSbTe (RHO)	(1 2 5)
67.65	Very weak	Te (HEX)	(1 0 4)
70.09	Very weak	BiSbTe (RHO)	(0 2 16)
72.08	Very weak	Te (HEX)	(2 1 2)
72.68	Weak	BiSbTe (RHO)	(2 1 10)
74.91	Very weak	BiSbTe (RHO)	(1 2 11)
77.87	Very weak	Te (HEX)	(1 1 4)
79.03	Very weak	BiSbTe (RHO)	(1 1 21)

HEX=Hexagonal, RHO=Rhombohedral

2.2. Monometallic Synthesis of Sb and Te Nanowires using OAM or OAC/OAM

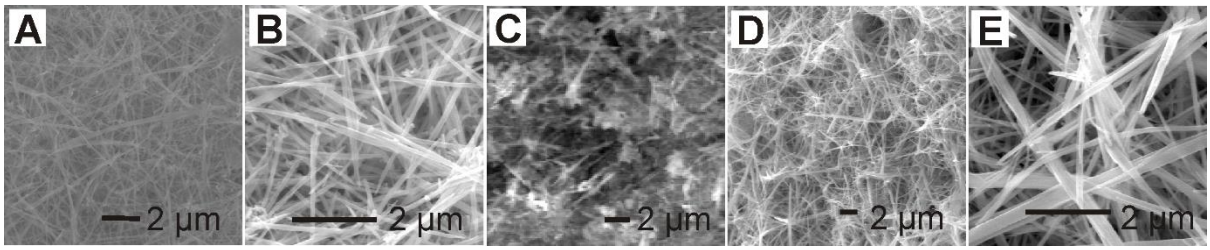

Figure A2.1. SEM images of Sb NWs synthesized using OAM (A, B), OAC/OAM (C) and Te NWs synthesized using OAM (D, E).

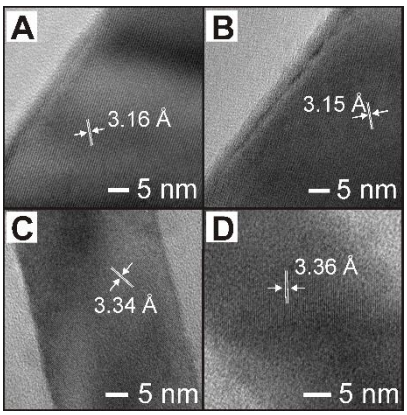

Figure A2.2. HR-TEM images of Sb NWs (A, B), and Te NWs (C, D) synthesized using OAM.

2.3. Photographs of Metal-Ligand Complexes

Each elemental precursor was dissolved in hexane solvent with a single capping ligand including OAM, OAC or DT under nitrogen atmosphere followed by stirring for 24 hours at room temperature. After that, a filter was used to separate the solid precursor from the liquid complex solution for analysis. The complexes of elemental precursors and each capping ligand have a different color as shown in Fig. A2.3.

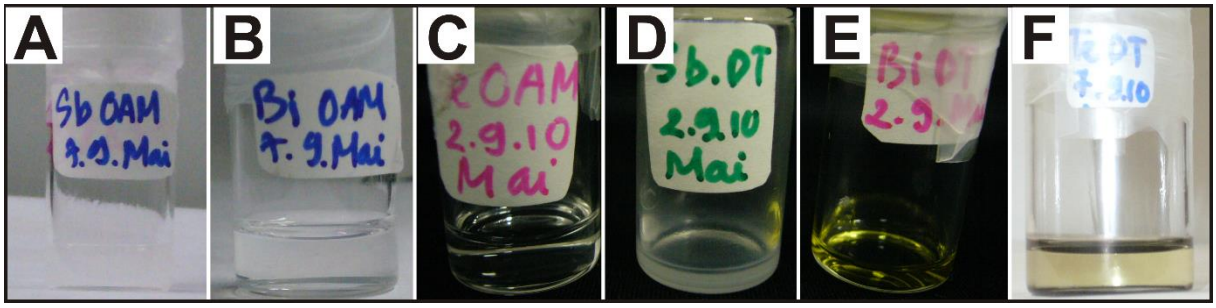

Figure A2.3. Photographs of single elemental complex solutions of Sb, Bi and Te with OAM and DT capping ligands. (A) Sb-OAM, (B) Bi-OAM, (C) Te-OAM, (D) Sb-DT, (E) Bi-DT and (F) Te-DT.

2.4. FTICR-MS Spectrum of Sb-DT Complex

To prove the existence of the metal-ligand complex, we conducted electrospray ionization Fourier transform ion cyclotron resonance mass spectroscopy (ESI-FTICR-MS) analysis for the Sb-DT complex. A Fourier transform ion cyclotron resonance mass spectrometer (FTICR-MS) equipped with a 9.4 T superconducting magnet (SolariX, Bruker Daltonics) was used for the analysis of the sample solutions. MS detection was performed in positive-ion ESI mode. Since Sb-DT complexes are thought to be relatively stable and Sb(III) shows specific isotope patterns (^{121}Sb:^{123}Sb; 57:43), they can easily be recognized in the mass spectrum.

Figure A2.4 shows an averaged mass spectrum measured for the sample prepared by dissolving $SbCl_3$ in DT at a concentration of 1×10^{-3} mM followed by dilution using 2-propanol. The spectrum shows various ions which are not observed for pure DT at an *m*/*z* range of 600-700. Two intense peaks are observed at *m*/*z* 611.32091 and 647.29856.

First, we analyzed the peak at *m*/*z* 611.32091 (Peak611) and its satellite peaks. The difference in *m*/*z* between the peak at *m*/*z* 613.32102 (Peak613) and Peak611 exactly

corresponds to the difference in accurate mass numbers of the stable isotopes of Sb. In addition, the intensity ratio between Peak611 and Peak613 is close to the isotope abundance ratio. The accurate mass obtained with the FTICR-MS supports the identification of Sb.

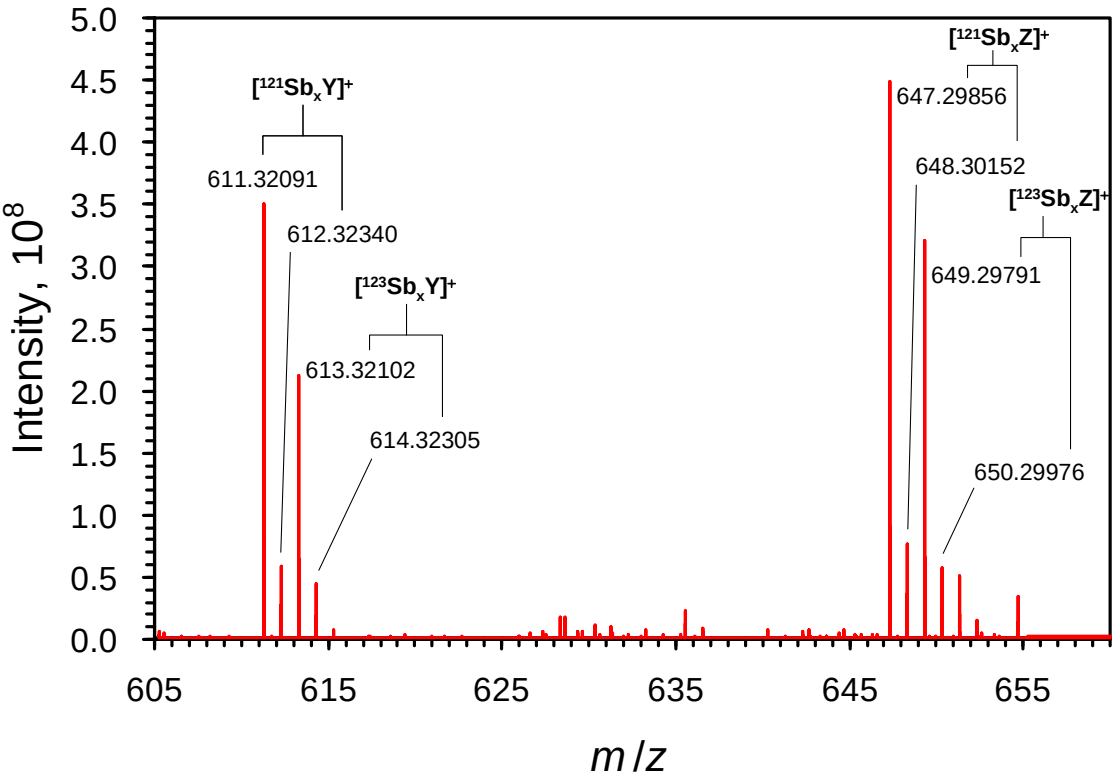

Figure A2.4. ESI-FTICR-MS spectrum of Sb-DT complexes.

On the other hand, the difference in *m*/*z* between the peak at *m*/*z* 612.32340 (or *m*/*z* 614.32305) and Peak611 (or Peak613) exactly corresponds to the difference in accurate mass numbers of the stable isotopes of C (^{12}C =12, ^{13}C=13.00335484). This result indicates that the ion has a molecular structure that contains carbon atoms. Consequently, we can conclude that Peak611 corresponds to a specific ion related to an Sb-DT complex, even though we couldn't identify its composition. Therefore, the Peak611 is designated as $[^{121}Sb_xY]^+$ hereafter where Y represents a DT-derived organic ligand.

Next, the peak at *m*/*z* 647.29856 (Peak647) and its satellite peaks are investigated. Again, the difference in *m*/*z* between Peak647 and the peak at *m*/*z* 649.29791 (Peak649) exactly corresponds to the difference in accurate mass numbers of the stable isotopes of Sb. Also, the

difference in *m*/*z* between the peak at *m*/*z* 648.30152 (or *m*/*z* 650.29976) and Peak647 (or Peak649) exactly corresponds to the difference in accurate mass numbers of the stable isotopes of C. Thus, we can conclude that Peak647 also corresponds to another ion related to an Sb-DT complex, which has a different ligand structure compared to $[^{121}Sb_xY]^+$. Thus, the Peak647 is designated as $[^{121}Sb_xZ]^+$ where Z represents a DT-derived organic ligand whose molecular structure differs from Y.

2.5. TGA Data of Sb-DT Complex

Thermogravimetric analysis (TGA) was performed using a Seiko TG/DTA6200 to investigate the thermal decomposition behavior of the Sb-DT complex. 39.618 milligrams of the Sb-DT complex was placed in an aluminum pan, and this was then placed in the TGA instrument. The temperature was raised to 600 °C at a heating rate of 10 °C/min under a N_2 atmosphere (flow rate 200 mL/min). Figure A.2.5 shows the resulting TG curve for the analysis of the Sb-DT complex.

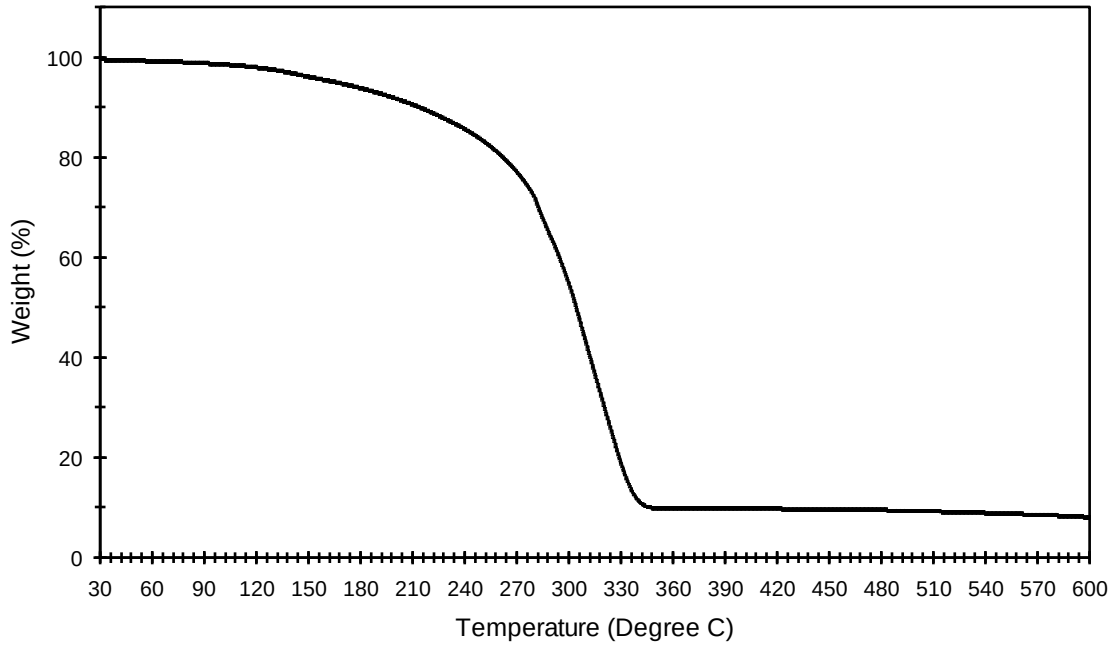

Figure A2.5. TG curve of Sb-DT complex.

2.6. Comparison of XRD Peak Position Collected for Resulting NPs Synthesized using $BiCl_3$ and $BiCl_3/SbCl_3$ with DT as Capping Ligands

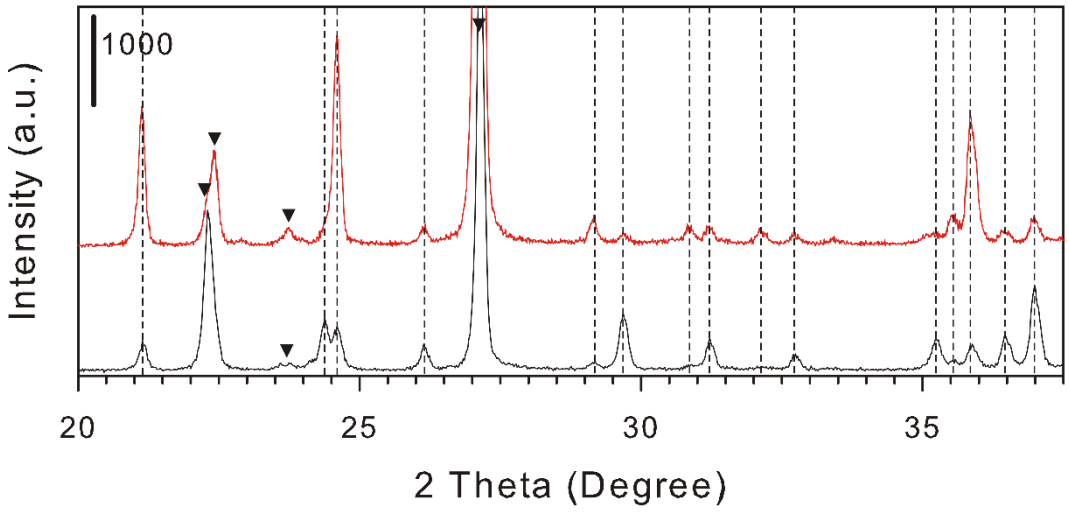

Figure A2.6. XRD patterns of NPs synthesized using DT and $BiCl_3$ (red curve) and $BiCl_3/SbCl_3$ (black curve) in range of 20 to 37.5 in two theta degree. The symbol (▼) was used to label for the peaks of Bi with rhombohedral structure. The unidentifiable peaks for these two NPs are found to have the same pattern. The dash lines were used to show the coincidence of the unidentifiable peak position of those two XRD patterns.

2.7. Bimetallic Synthesis of Bi-Te Halide Precursors and DT

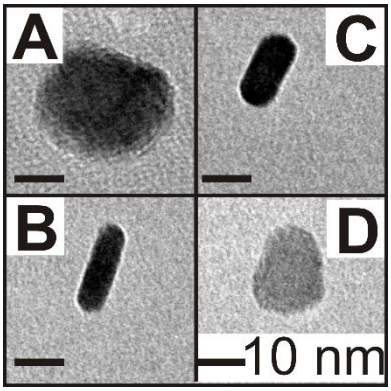

Figure A2.7. TEM images for NPs synthesized using Bi-Te halide precursors and DT as capping species. The images of individual NPs show the different contrast arising from the different alignment with electron beam in which (A and D) show the top down view and (B and C) show the side view of disc like NPs.

2.8. Results for Trimetallic Approach using Oleic Acid as Capping System

The resulting NPs obtained for trimetallic synthesis using oleic acid as capping species shows nanodiscs studded on NWs in the TEM images (Fig. A2.8). The XRD pattern collected for these materials shows the existence of several phases including Te, Bi_2Te_3 and Sb_2Te_3 (Fig. A2.9). The elemental analysis based on ICP-MS confirmed the composition of $Bi_{11}Sb_{23}Te_{66}$ which is consistent with the XRD results.

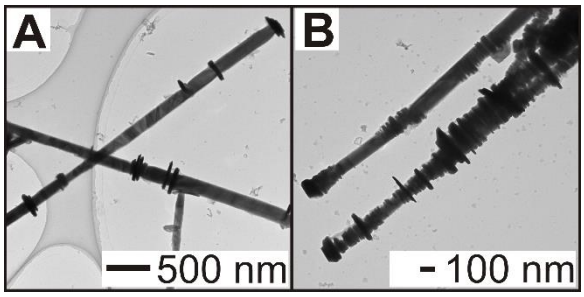

Figure A2.8. TEM images for NPs synthesized using three elemental precursors and OAC as capping species with 1:1 molar ratio between precursors and OAC.

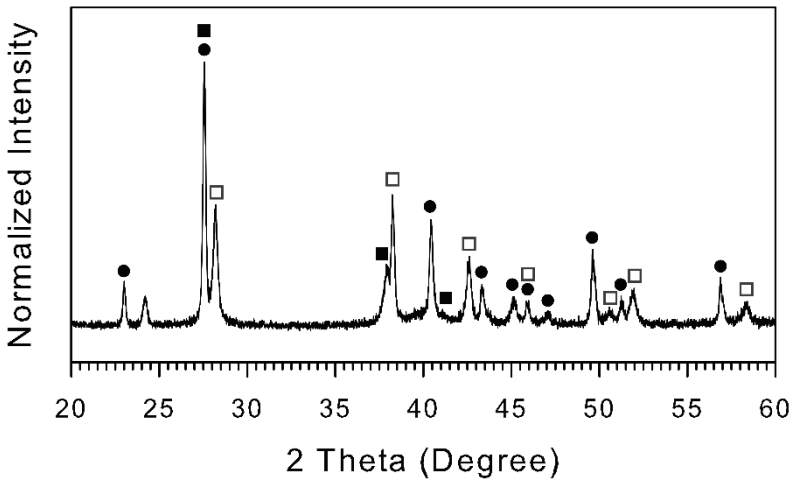

Figure A2.9. XRD pattern for resulting NPs synthesized using three elemental precursors and OAC as capping species with 1:1 molar ratio between precursors and OAC. The peak identities were label by

symbol circle (●) for hexagonal Te, filled square (■) for rhombohedral Bi_2Te_3 and open square (□) for rhombohedral Sb_2Te_3.

Table A2.19. XRD peak positions and corresponding crystal planes for Fig. A2.9 (BiSbTe-OAC system).

2 Theta (Degree)	Intensity	Phase	(*h k l*)
23.01	Very weak	Te (HEX)	(1 0 0)
27.57	Strong	Te (HEX), Bi_2Te_3 (RHO)	(101), (015)
28.20	Medium	Sb_2Te_3 (RHO)	(015)
37.89	Weak	Bi_2Te_3 (RHO)	(1010)
38.24	Medium	Sb_2Te_3 (RHO), Te(HEX)	(1010), (102)
40.43	Medium	Te (HEX)	(110)
41.03	Very weak	Bi_2Te_3 (RHO)	(110)
42.62	Weak	Sb_2Te_3 (RHO)	(110)
43.33	Weak	Te (HEX)	(111)
45.26	Very weak	Te (HEX)	(003)
45.86	Weak	Te(HEX), Sb_2Te_3 (RHO)	(003), (1013)
47.03	Very weak	Te (HEX)	(200)
49.63	Weak	Te (HEX)	(201)
50.56	Very weak	Sb_2Te_3 (RHO)	(119)
51.19	Very weak	Te (HEX)	(112)
51.97	Very weak	Sb_2Te_3 (RHO)	(205)
56.84	Weak	Sb_2Te_3 (RHO), Te (HEX)	(0117), (202)
58.35	Very weak	Sb_2Te_3 (RHO)	(0210)

HEX=Hexagonal, RHO=Rhombohedral

Appendix III

for

Chemical synthesis of BiSbTe Nanoparticles with Composition and Shape Manipulation

3.1. Vegard's Law

For an alloy, Vegard's law is an approximate empirical rule which holds that at constant temperature a linear relation exists between the crystal lattice parameter of an alloy (A-B) and the concentrations of the constituent elements (A and B). The mathematical expression of Vegard's law is given by:

$$D_{A\text{-}B} = xd_A + (100\text{-}x)d_B \qquad \text{(Eq. A3.1)}$$

where d_A, d_B and $d_{A\text{-}B}$ denote the lattice spacings of A, B and AB, respectively, and x is the molar percent of A in the alloy between A and B.

3.2. Crystalline size calculated from Scherrer Equation

Scherrer equation relating the crystalline size and the broadening of the XRD peak:

$$d = K\lambda/(\beta\cos\theta) \qquad \text{(Eq. A3.2)}$$

where d [nm] is the mean size of the crystalline domain (crystalline size) of the nanoparticles, K is the shape factor (dimensionless) which has the typical value of 0.9 (but depends on the shape of nanoparticles), λ [nm] is the X-ray wavelength, β [rad] is the peak width at half the maximum intensity (FWHM) and θ [rad] is the peak position (Bragg angle). K=0.9, and λ=0.15418 nm were used to calculate the mean crystalline size (d) of BiSb NPs.

3.3. XRD peak assignment for BiSbTe NPs

Table A3.1. XRD peak positions and corresponding crystal planes for Fig. 3.10.

2 Theta (Degree)	Intensity	Phase	(*h k l*)
27.59	Strong	Te (HEX), BiSbTe (RHO)	(1 0 1), (0 1 5)
37.73	Medium	BiSbTe (RHO)	(1 0 10)
40.38	Weak	Te (HEX)	(1 1 0)
41.11	Medium	BiSbTe (RHO)	(1 1 0)
44.95	Very weak	BiSbTe (RHO)	(1 1 6)
45.44	Very weak	BiSbTe (RHO)	(1 0 13)
50.27	Weak	BiSbTe (RHO)	(2 0 5)
53.74	Very weak	BiSbTe (RHO)	(1 0 16)
57.05	Weak	BiSbTe (RHO)	(0 2 10)
62.17	Weak	BiSbTe (RHO)	(1 1 15)
66.88	Very weak	BiSbTe (RHO)	(1 2 5)
67.65	Weak	Te (HEX)	(1 0 4)
70.09	Very weak	BiSbTe (RHO)	(0 2 16)
73.2	Weak	BiSbTe (RHO)	(2 1 10)

HEX=Hexagonal, RHO=Rhombohedral

Reference: L. Vegard. Die Konstitution der Mischkristalle and die Raumfüllung der Atome. Zeitschrift für Physik, 5:17, 1921.

Appendix IV

for

Novel One-pot Chemical Synthesis of Zinc Antimonide Nanoparticles as Building Blocks for Nanostructured Thermoelectric Materials

4.1. TEM images of Zn-Sb nanoparticles

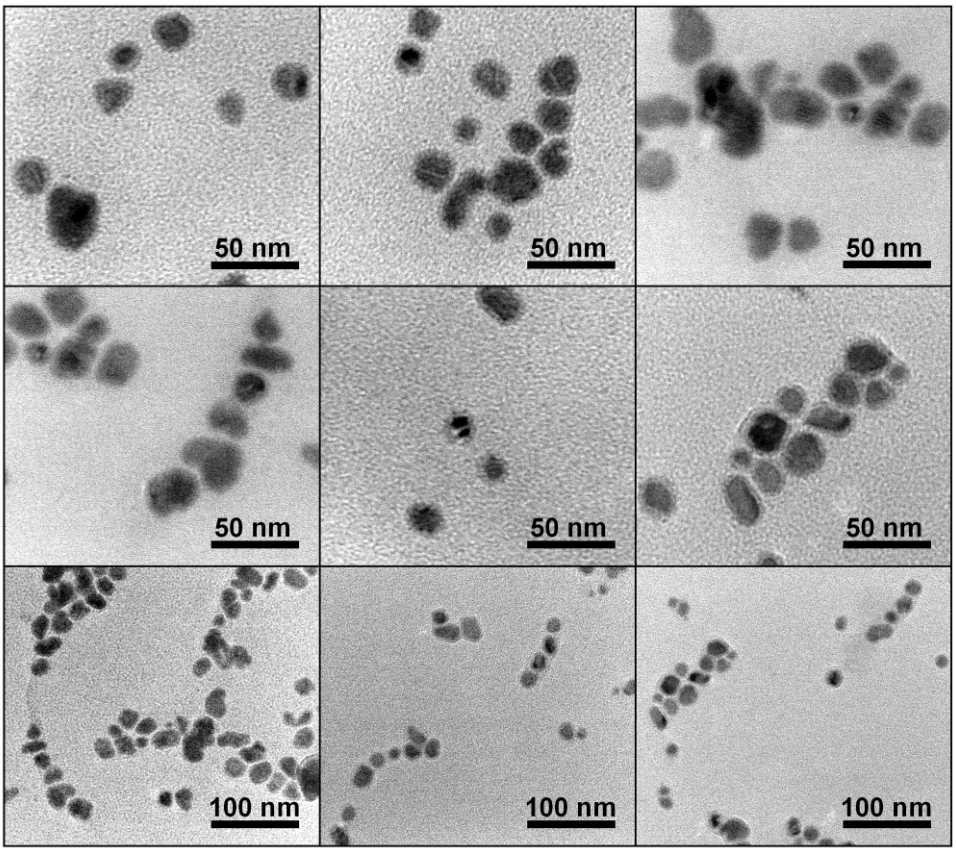

Figure A4.1. TEM images of Zn-Sb nanoparticless collected in different areas.

4.2. XPS peak parameters

Table A4.1. Peak parameters of Zn nanoparticles.

	$Zn2p_{3/2}$ (metal)	$Zn2p_{1/2}$ (metal)	$Zn2p_{3/2}$ (oxide)	$Zn2p_{1/2}$ (oxide)
Peak position	1021.66	1044.71	1024.62	1047.68
FWHM	1.17	1.16	1.07	1.16
M	0	0.26	0	0
α	0	0	0	0
Peak separation	23.06 eV		23.06 eV	
Spin-orbit intensity ratio	2.00		2.19	

Table A4.2. Peak parameters of Sb nanoparticles.

	$Sb3d_{5/2}$ (metal)	$Sb3d_{3/2}$ (metal)	$Sb3d_{5/2}$ (Sb_2O_3/Sb_2O_4)	$Sb3d_{3/2}$ (Sb_2O_3/Sb_2O_4)	$Sb3d_{5/2}$ (O1s(2)/Sb_2O_5)	$Sb3d_{3/2}$ (Sb_2O_5)	O1s(1)
Peak position	527.80	537.20	529.75	539.05	531.37	540.94	532.19
FWHM	0.80	0.80	1.09	1.04	0.74	0.85	1.04
M	0	0	0	0	0	0	0
α	0	0	0	0	0	0	0
Peak separation	9.40 eV		9.30 eV		–		–
Spin-orbit intensity ratio	1.53		1.68		–		–

Table A4.3. Peak parameters of Zn-Sb nanoparticles.

	$Zn2p_{3/2}$ (metal)	$Zn2p_{1/2}$ (metal)	$Sb3d_{5/2}$ (metal)	$Sb3d_{3/2}$ (metal)	$Sb3d_{5/2}$ (oxide)	$Sb3d_{3/2}$ (oxide)	O1s(1)	O1s(2)
Peak position	1021.42	1044.51	527.20	536.57	529.87	539.29	531.63	530.40
FWHM	0.88	0.92	0.59	0.57	0.67	0.80	0.82	0.84
M	0.55	0.69	0.84	0.68	0.65	0.33	0.84	0.84
α	0	0	0.03	0.02	0	0	0	0
Peak separation	23.09 eV		9.37 eV		9.42 eV		–	–
Spin-orbit intensity ratio	2.09		1.57		1.59		–	–

Note:

The shift of the binding energy scale due to charging was corrected by referencing the C1 peak in the C 1s signal to 284.8 eV[1] and the background was subtracted by Shirley's method.[2] The peaks were deconvoluted by/fitted to the asymmetric Gaussian-Lorentzian (G-L) mixed function:[3,4]

$$f(x) = \frac{I_0}{\{1 + M(x - x_0)^2 / \Gamma^2\} \exp\{(1 - M)\ \ln 2\ (x - x_0)^2 / \Gamma^2\}} \qquad \text{(Eq. A4.1)}$$

where I_0, x_0, x, Γ, and M are the peak height, the peak binding energy (BE), the BE, a parameter for the peak width, and the G-L mixing ratio, respectively. $M = 0$ gives a pure Gaussian curve,

while M = 1 gives a pure Lorentzian curve. To introduce the asymmetry into the G-L mixed function, the following variable transformation is incorporated in Equation (1):

$$(x-x_0) \rightarrow \frac{(x-x_0)}{\{1+\alpha(x-x_0)/\Gamma\}} \qquad \text{(Eq. A4.2)}$$

where α is an asymmetric factor (α = 0 gives a symmetric line shape).

It has been reported that the BE of Sb $3d_{3/2}$ in Sb_2O_3, Sb_2O_4 and Sb_2O_5 are 539.6, 539.8 and 540.2 eV, respectively.[5] In the case of Zn-Sb NPs, the lower energy Sb 3d component corresponds to Sb metal. The asymmetric higher energy $3d_{5/2}$ component was deconvoluted by using three G-L mixed functions corresponding to Sb oxide (peak at 529.87 eV), O 1s(1) (531.63 eV) and O 1s(2) (530.40 eV).[6]

References

1 J. F. Moulder, W. F. Stickle, P. E. Sobol, K. D. Bomben, *A Handbook of X-ray Photoelectron Spectroscopy*, ed. by J. Chastain, Physical Electronics Division, Perkin-Elmer Corporation, Eden Prairie, **1992**.

2 D. A. Shirley, *Phys. Rev. B* **1972**, *5*, 4709.

3 R. O. Ansell, T. Dickinson, A. F. Povey, P. M. A. Sherwood, *J. Electroanal. Chem.* **1979**, *98*, 79.

4 H. Darmstadt, D. Pantea, L. Sümmchen, U. Roland, S. Kaliaguine, C. Roy, *J. Anal. Appl. Pyrolysis* **2000**, *53*, 1.

5 R. Delobel, H. Baussart, J. Leroy, J. Grimblot, L. Gengembre, *J. Chem. Soc. Faraday Trans. 1* **1983**, *79*, 879.

6 T. Honma, R. Sato, Y. Benino, T. Komatsu, V. Dimitrov, *J. Non-Cryst. Solids* **2000**, *272*, 1.

Appendix V

for

Large Scale Chemical Synthesis of Zn-Sb Nanoparticles and Thermoelectric Properties of Zn-Sb Nanostructured Materials

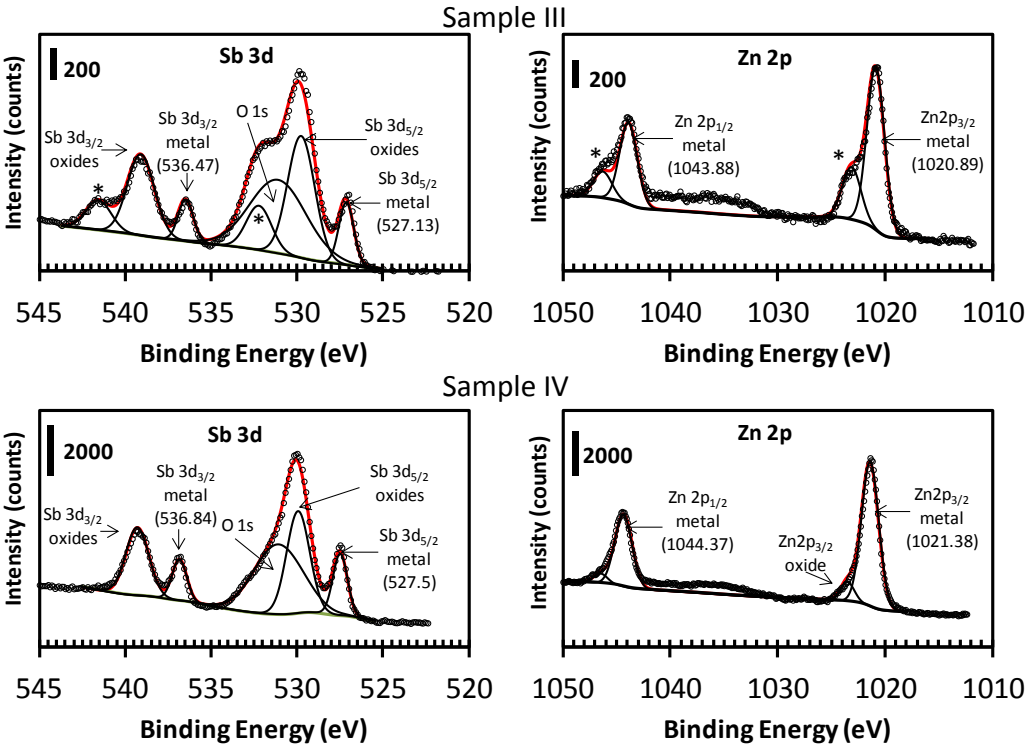

Figure A5.1. XPS spectra of the nanoparticles in Sample III (upper row) and IV (lower row) after annealing to remove oleylamine with the narrow scan areas of Sb 3d (left) and Zn 2p (right). The peaks marked by stars (*) appear at higher binding energy than usual for the corresponding oxide peaks of Sb and Zn (even though the spin-orbit splitting is identical of Sb 3d and Zn 2p) and are thought to be the shake-up satellite peaks. The peaks for O 1s may contain different types of O including surface absorbed oxygen, O in the oxides of Sb and Zn, which are broaden and were shown as 1 peaks for the simplification when analyze the composition of Zn and Sb by XPS.

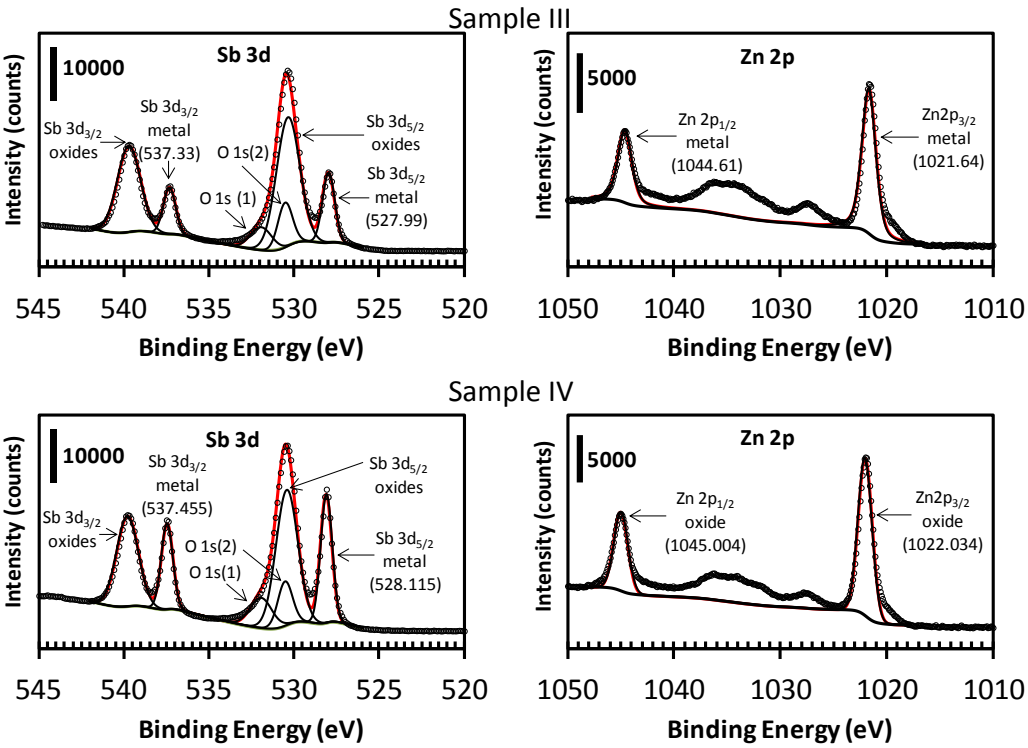

Figure A5.2. XPS spectra of $Zn_{42}Sb_{58}$ pellet prepared from Sample III (upper row) and $Zn_{45}Sb_{55}$ pellet prepared from Sample IV (lower row) for the narrow scan areas of Sb 3d (left) and Zn 2p (right). The ZnO are clear evidenced in pellet of Sample IV. (See Appendix IV for more detail explanation of O peaks)

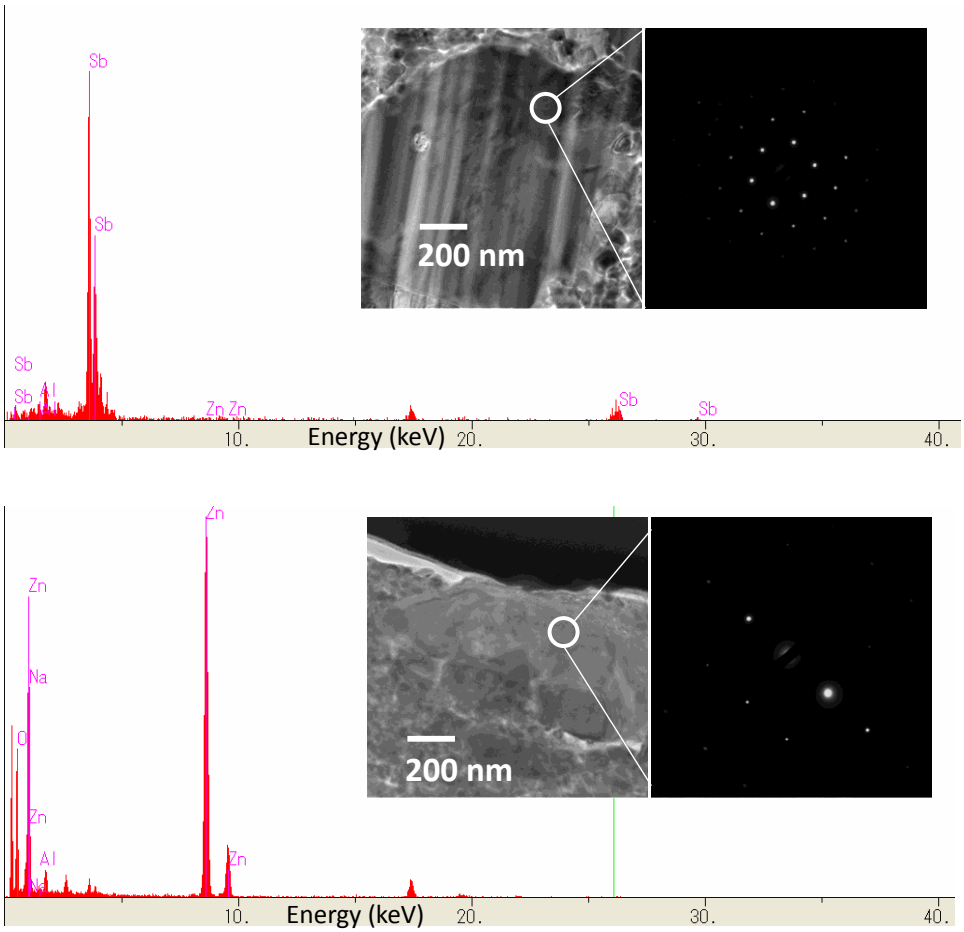

Figure A5.3. TEM-EDS spectrum of areas in the pellet prepared from Sample IV ($Zn_{45}Sb_{55}$) that contains seggregated Sb (up) or Zn (down). O peak appears with Zn area in the sample. The insets are the selected area electron diffraction patterns (SAED) measured on the areas marked by white circles in TEM images. SAED patterns of Sb and ZnO can be obtained.

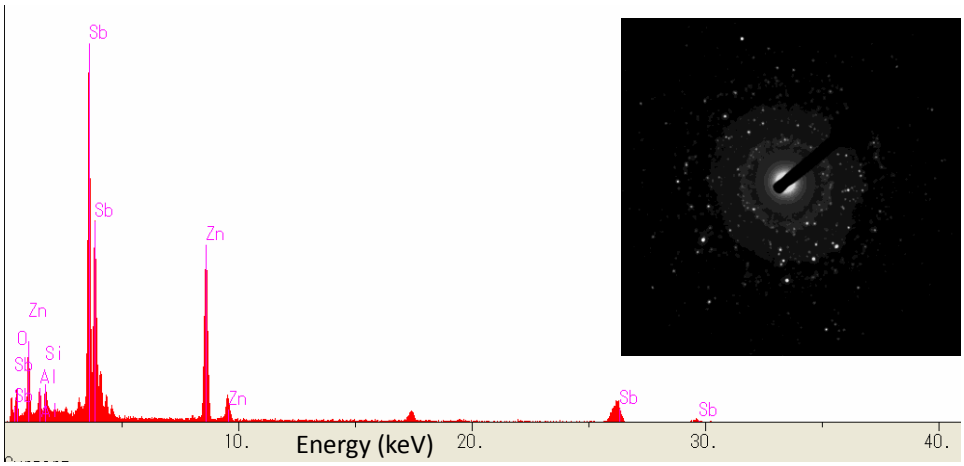

Figure A5.4. TEM-EDS spectrum of one area in the pellet prepared from Sample IV ($Zn_{45}Sb_{55}$). The inset is the SAED pattern of this sample, which indicates that sample is not single crystal in nature and the d-spacing of either ZnO, Sb, antimony oxides or ZnSb can be found.

List of Publication

Paper

1. N. T. Mai, T. T. Thuy, D. Mott, and S. Maenosono, "Chemical Synthesis of Blue-emitting Metallic Zinc Nano-hexagons", *CrystEngComm* **2013**, *15*, 6606.
2. N. T. Mai, D. Mott, K. Higashimine, and S. Maenosono, "One-pot Chemical Synthesis of Zinc Antimonide Nanoparticles as Building Blocks for Nanostructured Thermoelectric Materials", *Chem. Lett.* **2012**, *41*, 1529.
3. N. T. Mai, D. Mott, N. T. B. Thuy, I. Osaka, and S. Maenosono, "Study on Formation Mechanism and Ligand-directed Architectural Control of Nanoparticles Composed of Bi, Sb and Te: Toward One-pot Synthesis of Ternary $(Bi,Sb)_2Te_3$ Nanobuilding Blocks", *RSC Adv.* **2011**, *1*, 1089.
4. D. Mott, N. T. Mai, N. T. B. Thuy, T. Sakata, K. Higashimine, M. Koyano and S. Maenosono, "Elucidation of the Complex Structure of Nanoparticles Composed of Bismuth, Antimony and Tellurium using Scanning Transmission Electron Microscopy", *J. Phys. Chem. C* **2011**, *115*, 17334.
5. D. Mott, N. T. B. Thuy, N. T. Mai, Y. Maeda, Tran P. T. Linh, M. Koyano, and S. Maenosono: "Bismuth, Antimony and Tellurium Alloy Nanoparticles with Controllable Shape and Composition for Efficient Thermoelectric Devices", *Phys. Stat. Sol. A* **2011**, *208*, 52.

Book Chapter

"Anisotropic Nanoparticles for Efficient Thermoelectric Devices", N. T. Mai, D. Mott and S. Maenosono, In "Complex-Shaped Metal Nanoparticles: Bottom-Up Synthesis and Applications", Edited by Tapan K. Sau and Andrey L. Rogach, Chapter 16, Wiley-VCH, **2012**.

Proceeding

1. D. Mott, N. T. Mai, T. Sakata, M. Koyano, K. Higashimine, and S. Maenosono, "True Atomic Level Imaging of Shaped Nanoparticles Composed of Bismuth, Antimony and Tellurium using Scanning Transmission Electron Microscopy", The MRS Proceedings, Vol. 1349, mrss 11-1349-dd01-09, **2011**.

2. D. Mott, N. T. Mai, N. T. B. Thuy, T. Sakata, M. Koyano, and S. Maenosono, “Synthesis, Fabrication, and Characterization of Multidimensional Nanoparticle Based Thermoelectric Materials Composed of Bismuth, Antimony, and Tellurium”, The MRS Proceedings, Vol. 1329, mrss11-1329-i04-05, **2011**.
3. D. Mott, N. T. B. Thuy, N. T. Mai, Y. Maeda, T. P. T. Linh, G. Nakamoto, M. Koyano, and S. Maenosono, “Design and Synthesis of One and Two Dimensional Thermoelectric Nanomaterials Composed of Bismuth, Antimony, and Tellurium”, The MRS Proceedings, Vol. 1267, DD02-11, Published Online, **2010**.

Patent

1. “金属亜鉛ナノ粒子、及びその製造方法”, 前之園 信也, Derrick Mott, Nguyen Thanh Mai, 特願 2013-123183.
2. “亜鉛アンチモン系化合物ナノ粒子”, 前之園 信也, Nguyen Thanh Mai, Derrick Mott 特願 2012-105066.

Presentation in International Conferences

1. N. T. Mai, Md. Shahiduzzaman, S. Kodaira, K. Higashimine, D. Mott and S. Maenosono, "Chemical Synthesis, Characterization and Thermoelectric Properties of ZnSb Nanoparticles and their Nanostructured Materials", *The 32 International Conference on Thermoelectrics (ICT) 2013*, 30 Jun- 4 July **2013**, Kobe, Japan.
2. N. T. Mai, Md. Shahiduzzaman, S. Kodaira, D. Mott, and S. Maenosono, "BiSb Nanoparticles: Chemical Approach towards Controllable Composition", *The 32 International Conference on Thermoelectrics (ICT) 2013*, 30 Jun- 4 July **2013**, Kobe, Japan.
3. N. T. Mai, S. Kodaira, Md. Shahiduzzaman, K. Higashimine, D. Mott, and S. Maenosono, "Chemical Synthesis of BiSbTe Based Nanoparticles with Composition Manipulation", *E-MRS Spring 2013*, 27-31 May **2013**, Strasbourg, France.
4. N. T. Mai, S. Kodaira, Md. Shahiduzzaman, D. Mott, K. Higashimine, and S. Maenosono, "ZnSb Nanoparticles and Nanostructured Materials: Chemical Synthesis, Characterization and Thermoelectric Properties", *E-MRS Spring 2013*, 27-31 May **2013**, Strasbourg, France.
5. N. T. Mai, D. Mott, K. Higashimine, and S. Maenosono, "Chemically Synthesized ZnSb Alloy Nanoparticles towards Thermoelectric Applications", *The 2012 MRS Fall Meeting*, 25-30 November **2012**, Boston, USA.
6. N. T. Mai, D. Mott, K. Higashimine, and S. Maenosono, "One-pot Chemical Synthesis of ZnSb Alloy Nanoparticles towards Nanostructured Thermoelectric Materials", *The 2012 MRS Fall Meeting*, 25-30 November **2012**, Boston, USA.
7. N. T. Mai, D. M. Mott, K. Higashimine, and S. Maenosono, "Chemically Synthesized Zn-Sb Nanoparticles towards Thermoelectric Applications", *The 6th Internation Workshop on Advanced Materials Science and Nanotechnology (IWAMSN 2012)*, 30 October - 2 November **2012**, Halong City, Vietnam.
8. N. T. Mai, D. Mott, K. Higashimine, and S. Maenosono, "One-pot Chemical Synthesis of ZnSb Alloy Nanoparticles towards High Performance Thermoelectric Application", *IUMRS-ICEM 2012*, 23-28 September **2012**, Yokohama, Japan.
9. N. T. Mai, P. Kumar, Derrick. M. Mott, and Shinya Maenosono, "Synthesis and Growth Mechanism of Anisotropic BiSbTe Ternary Nanoparticles for Highly Efficient Thermoelectric Applications", *Asia Pacific Interdisciplinary Research Conference (AP-IRC)*, 16-18 November **2011**, Toyohashi, Ichi, Japan.

10. N. T. Mai, D. Mott and Shinya Maenosono, "Formation Mechanism of Anisotropic Nanoparticles Composed of Bismuth, Antimony and Tellurium", *UK Colloids 2011*, 4-6 July **2011**, De Vere Venue, London, UK.
11. D. Mott, N. T. Mai, N. T. B. Thuy, T. Sakata, M. Koyano, and S. Maenosono, "Manipulation of Shape and Composition of Nanoparticles Composed of Bi, Sb and Te in a Modified Polyol Synthesis Through Simple Ligand Control", *2011 Bilateral Energy Conference* (jointly organized by MRS and E-MRS), 10-12 May **2011**, Nice, France.
12. N. T. Mai, D. Mott, N. T. B. Thuy, M. Koyano, and S. Maenosono, "Study the Synthetic Technique and Formation Mechanism of BiSbTe Nanoparticles towards Highly Efficient Thermoelectric Application", *2011 Bilateral Energy Conference* (jointly organized by MRS and E-MRS), 10-12 May **2011**, Nice, France.
13. N. T. Mai, D. Mott, N. T. B. Thuy, M. Koyano, and S. Maenosono, "Synthesis and Growth Mechanism Study of BiSbTe Nanoparticles with Controllable Morphology and Composition", *2011 Bilateral Energy Conference* (jointly organized by MRS and E-MRS), 10-12 May **2011**, Nice, France.
14. D. Mott, N. T. Mai, N. T. B. Thuy, T. Sakata, M. Koyano, and S. Maenosono, "Synthesis, Fabrication, and Characterization of Multidimesional Nanoparticle Based Thermoelectric Materials Composed of Bismuth, Antimony, and Tellurium", *The 2011 MRS Spring Meeting*, 25-29 April **2011**, San Francisco, USA.
15. D. Mott, N. T. Mai, N. T. B. Thuy, T. Sakata, M. Koyano, K. Higashimine and S. Maenosono, "True Atomic Level Imaging of Shaped Nanoparticles Composed of Bismuth, Antimony and Tellurium Using Scanning Transmission Electron Microscopy", *The 2011 MRS Spring Meeting*, 25-29 April **2011**, San Francisco, USA.
16. N. T. Mai, D. Mott, N. T. B. Thuy, M. Koyano, and S. Maenosono, "Bismuth, Antimony and Tellurium Nanowire Applied to Thermoelectric Materials: Synthesis and Growth Mechanism", *PACIFICHEM 2010*, 15-20 December **2010**, Honolulu, Hawaii, USA.

Abstract of Subtheme Research

The large scale syntheses of Zn-Sb nanoparticles (NP)s result in gram amount of NPs for making the pellet to measure the thermoelectric properties of the nanostructured bulk materials. The NPs with size of 23 nm and composition of Zn-Sb NPs rich in Sb were synthesized via wet chemical approach. The organic capping molecules on surface of NPs were removed during heat treatment at 355 ^{o}C for 2 h. The pellet can be obtained by pressing at room temperature which has size of 10.1 mm in diameter and 3.7 mm in height. The sintering at elevated temperature under vacuum was conducted to improve the density of the NPs pellet. Finally, the thermoelectric properties of the NPs bulk sample were characterized using PPMS-TTO system and four-probe method was utilized to re-check the electrical resistivity of the sample. The thermal conductivity κ of the sample was found to be extremely low of 0.5 $Wm^{-1}K^{-1}$ at room temperature. The electrical resistivity ρ however, is also high (6 mΩm) and the Seebeck coefficient α of the sample is of about 15 μVK^{-1}. The results of measurement suggest that the low density and the nanostructure of the pellet contribute to the extremely low value of κ while the composition inhomogeneity and far from equal molar ratio affects on the value of ρ and α. The overall *ZT* is very small.